Photonic crystal structures for efficient localization or extraction of light

Thesis by

Jelena Vučković

In Partial Fulfillment of the Requirements

for the Degree of

Doctor of Philosophy

California Institute of Technology

Pasadena, California

2002

(Submitted September 17th, 2001)

Acknowledgements

An attempt to thank all the great people who have inspired me or helped me throughout my graduate studies, and to explain in details their role and importance in my life, would lead to an acknowledgement as long as this thesis. All of them contributed to making my Caltech experience so pleasant and enjoyable, that I sometimes think I would stay here forever.

My sincere gratitude to Professor Axel Scherer, for redirecting my interests from information theory to photonic crystals when I arrived here, for assigning me a couple of really cool projects, for giving me freedom to work on my own ideas, and for all the help and understanding.

I was very fortunate to collaborate with several great scientists during my years at Caltech, and they all had a profound influence on myself and my work. Many thanks to Professors Hideo Mabuchi, Amnon Yariv and Harry Atwater from Caltech, and Professor Yoshihisa Yamamoto from Stanford.

Huge thanks as well to all of my colleagues from the Nanofabrication Group, who have constantly inspired me with their talent and knowledge, and who were both my coworkers and friends: Marko Lončar, Tomoyuki Yoshie, David Barsic, Ali Husain, Sir Theodore Doll, Oskar Painter, Joyce Wong, Chuan Chen-Cheng, Hou-Pu Chou, Cary Gunn, Ives Lassilly, Terrell Neal, Jeremy Witzens and Mark Adams. Thanks in particular to Marko, my big collaborator and a very good friend.

I also wish to thank Joe Schmid, the wizard-machinist, for help during the work on projection system, as well as our administrative assistant Kate Finigan and our lab coordinators Reynold Johnson and Guy De Rose, for helping us organize both ourselves and our labs.

To my parents and my brother: thanks for all the love, support and patience, for letting me be independent very early in life and for believing in me so much.

Finally, I definitely cannot express how thankful I am to Vlada, for being with me at all the bad and good times. This thesis is for him.

Abstract

Three-dimensional (3D) photonic crystals offer the opportunity of light manipulation in all directions in space, but they are very difficult to fabricate. On the other hand, planar photonic crystals are much simpler to make, but they exhibit only a "quasi-3D" confinement, resulting from the combined action of 2D photonic crystal and internal reflection. The imperfect confinement in the third dimension produces some unwanted out-of-plane loss, which is usually a limiting factor in performance of these structures. This thesis proposes how to fully take advantage of the relatively simple fabrication of planar photonic crystals, by addressing a problem of loss-reduction.

One of the greatest challenges in photonics is a construction of optical microcavities with small mode volumes and large quality factors, for efficient localization of light. Beside standard applications of these structures (such as lasers or filters), they can potentially be used for cavity QED experiments, or as building blocks for quantum networks. This work also presents the design and fabrication of optical microcavities based on planar photonic crystals, with mode volumes of the order of one half of cubic wavelength of light (measured in material) and with Q factors predicted to be even larger than 10^4.

In addition to photonic crystals fabricated in semiconductors, we also address interesting properties of metallic photonic crystals and present our theoretical and experimental work on using them to improve the output of light emissive devices.

Feature sizes of structures presented here are below those achievable by photolithography. Therefore, a high resolution lithography is necessary for their fabrication. The presently used e-beam writing techniques suffer from limitations in speed and wafer throughput, and they represent a huge obstacle to commercialization of photonic crystals. Our preliminary work on electron beam projection lithography, the technique that could provide us with the speed of photolithography and the resolution of e-beam writing, is also discussed in this thesis.

Contents

List of Figures

List of Tables

Chapter 1 Optical microcavities in planar photonic crystals

1.1 Introduction

Photonic crystals (PCs) are structures with periodic variation of dielectric constant in one, two or three dimensions.[1–5] This periodicity is usually of the order of the wavelength of light in material that the PC is made of. While the one-dimensional structures operating at optical wavelengths have been known for more than 20 years,[1] the extension of photonic crystals to two and three dimensions was simultaneously proposed by Yablonovitch and John in 1987.[2,3] Although 3D PCs offer the opportunity of light manipulation in all three dimensions in space, they are very difficult to fabricate.[6] For this reason, many research groups have concentrated their efforts on planar photonic crystals (i.e., 2D photonic crystals of finite depth) in recent years.[7–19] By introducing point or line defects into such 2D PC arrays, a variety of passive and active optical devices can be constructed, and integrated on a single chip. The fabrication procedures of planar PCs are much simpler than those of their 3D counterparts, but their light confinement is only "quasi-3D," and resulting from the combined action of 2D photonic crystal and internal reflection. The imperfect confinement in the third dimension produces some unwanted out-of-plane loss (radiation loss), which is usually a limiting factor in performance of these structures.

One of the most important properties of photonic crystals is their ability to localize light into small mode volumes. Even the simplest single defect microcavities in planar photonic crystals with triangular lattice, produced by changing the radius or refractive index of a single PC hole or rod, can localize light into the volumes as small as one half of cubic wavelength in material. Unfortunately, these most obvious microcavity designs have maximum quality factors of the order of only a few thousand.[8,20–22] However, our group at Caltech has recently proposed the design and fabrication of optical microcavities based on free-standing membranes, with $Q > 10^4$ and mode volumes still of the order of one half

of cubic wavelength of light in material.[8,23,24] The topic of this chapter is the design and fabrication of these novel structures. Beside standard applications (such as optical filters, or laser resonators), the possibility of using them for achieving spontaneous emission control, threshold-less lasing, or as building blocks for quantum networks will also be addressed.

1.2 Dispersion diagrams of planar photonic crystals

Two principal directions of planar photonic crystal research are structures based on optically thin semiconductor membranes (free-standing membranes),[7–9,11,20] and structures fabricated in slab waveguides consisting of a semiconductor core sandwiched between cladding layers of lower refractive index.[12] Therefore, the difference lies in the design of the waveguide used for the vertical confinement. For the past few years, our group at Caltech has been studying free-standing membranes patterned with periodic arrays of holes,[7–9,20] as shown in Figure 1.1. Although cladding layers can be useful in reduction of the out-of-plane loss, we have recently discovered that in their presence, additional lateral-loss mechanisms are permitted to occur and that lateral PC confinement can be lost.[25] This problem will be discussed in greater detail later in this chapter. Thus, we concentrate on designing structures based on free-standing membranes.

The first step in the structure design is the choice of PC parameters. There are five pa-

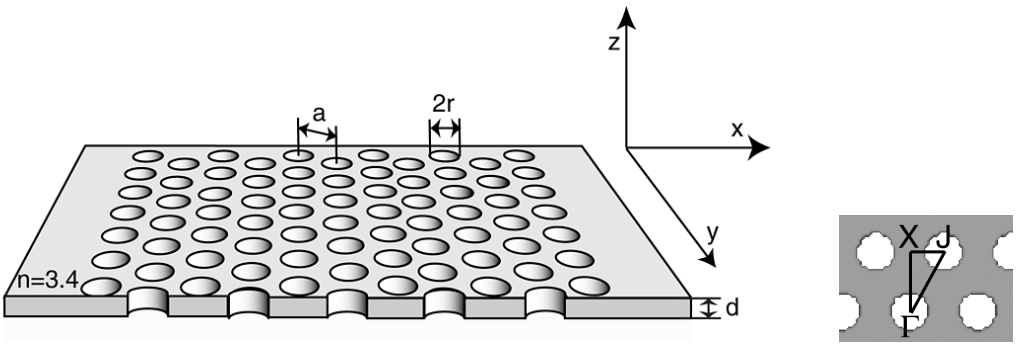

Figure 1.1: Optically thin membrane patterned with a triangular array of air holes.

rameters that we can control, as illustrated in Figure 1.1: the refractive index of material (n), the type of photonic crystal lattice (triangular, square...), the thickness of the slab

(d), the lattice periodicity (a), and the hole radius (r). The wavelength of light in air is denoted as λ. Since our structures are usually made out of Si or III-V semiconductors, we do not have much choice over the refractive index, which is in the range between 3.4 and 3.5. Furthermore, we concentrate mostly on triangular lattice crystals, which can provide us with a better lateral confinement than square lattice crystals.[26] However, properties of PC are still very sensitive to the remaining three parameters: d, r and a.

Most of the cavities presented in this chapter are based on the following two sets of param-

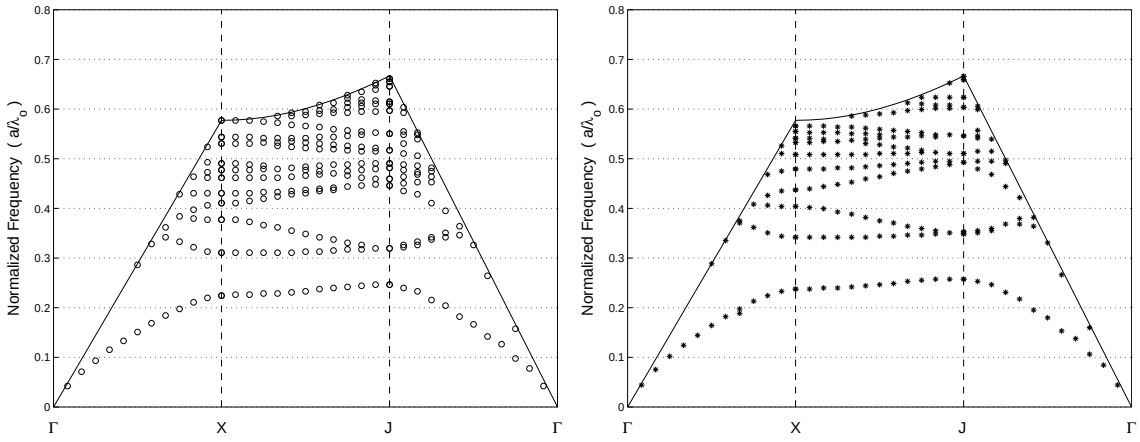

Figure 1.2: Band diagrams for TE-like modes of a thin slab surrounded by air on both sides and patterned with a triangular array of air holes. Parameters of photonic crystal are (a) n=3.4, d/a=0.75 and r/a=0.275; (b) n=3.4, d/a=0.65 and r/a=0.3.

eters: (1) n=3.4, d/a=0.75 and r/a=0.275; (2) n=3.4, d/a=0.65 and r/a=0.3. The band diagrams for TE-like modes in the planar PCs with these parameters are shown in Figure 1.2. On the horizontal axis, we plot the values of the wavevector in plane, and on the vertical axis we plot the normalized frequency of light in units of a/λ. All calculations presented in this chapter are done using the 3D finite-difference time-domain (FDTD) method. (For the explanation of the method, please refer to the Appendix I of this thesis). TE-like modes (also referred to as the even modes) have dominant E_x, E_y and B_z components in the middle of the slab. The solid lines in the plots represent the light line in air. Modes below this line can be guided in the slab and are called *guided modes*, whereas modes above

the light line (not plotted in the figures) are not confined in the slab and are called *leaky modes*. One can also observe the frequency region where guided modes do not exist, for any value of the wave-vector. This frequency region is called *the bandgap*. Guided modes are organized into modes above the bandgap (*air band, conduction band*), and modes below the bandgap (*dielectric band, valence band*). The names "conduction" and "valence" band are borrowed from solid-state physics, while the names "dielectric" and "air" band are based on where the electric field energy of a mode is mostly concentrated. For example, the dielectric band modes mostly concentrate their electric field energy in the high refractive index region (semiconductor), thereby reducing their frequencies, while the air band modes mostly concentrate their electric field energy in air region (holes), thereby increasing their frequencies.[4] It is important to note that the structures presented here do not have a bandgap for TM-like (odd) modes (having the dominant B_x, B_y and E_z components in the middle of the slab).

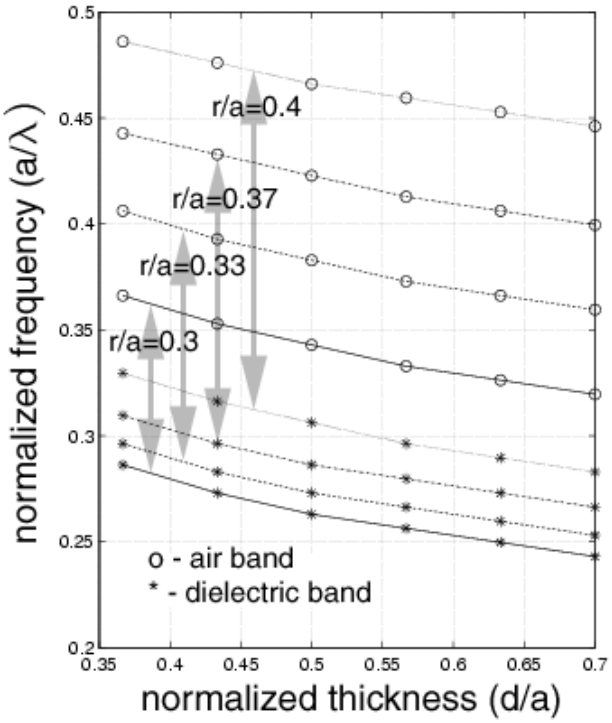

Figure 1.3: Position and size of the bandgap as a function of d/a and r/a in the triangular lattice with n=3.5. (Courtesy of Marko Lončar)

As mentioned previously, parameters of the band diagram are highly sensitive to d, r and a. Figure 1.3 illustrates how the bandgap edges shift in frequency as a function of d/a and r/a, in the case of the triangular lattice with $n = 3.5$. Therefore, if d/a increases, but r/a is kept constant, the band edges shift downwards in frequency and bandgap size remains approximately constant in the analyzed range. On the other hand, if d/a is kept constant, but r/a increases between 0.3 and 0.4, the bandgap edges shift upwards in frequency and the bandgap size increases. Even though the increase in the hole size leads to the increase

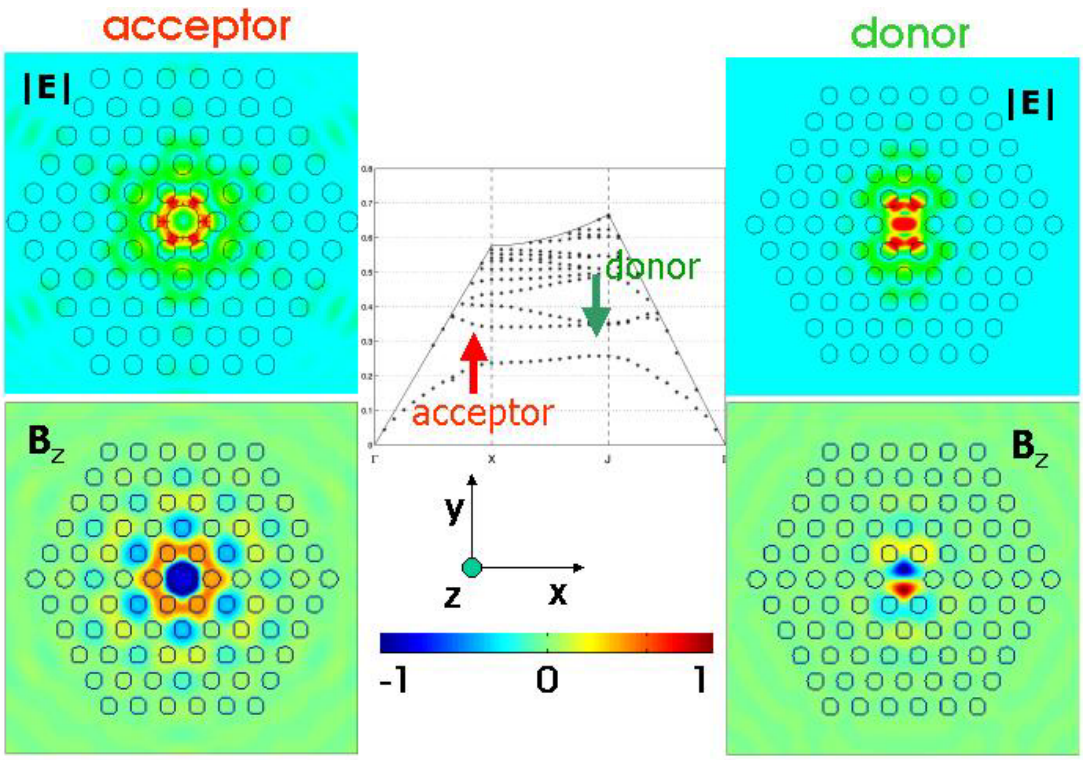

Figure 1.4: Acceptor defect state (monopole) and donor defect state (dipole) excited by changing the radius of a single PC hole.

of the bandgap, which is desirable for suppression of lateral loss, it also produces large out-of-plane losses, as we will see later. For this reason, we limit r/a of our structures to rather modest values of around 0.3. The control over a position of a bandgap by tuning r/a and d/a is a very powerful property of planar PCs, which implies that one can tune mirrors by lithography and etching, instead of growth. Furthermore, mirrors operating at many different wavelengths can be constructed on the same chip.

1.3 Point defects in planar photonic crystals

The simplest way of forming a microcavity starting from the photonic bandgap (PBG) structure shown in Figure 1.1 is by changing the radius of a single hole, or by changing its refractive index. The former method is more interesting from the point of fabrication, since lithographic tuning of parameters of individual holes is a simple process to implement. By increasing the radius of a single hole, an acceptor defect state is excited, i.e., pulled into the bandgap from the dielectric band. On the other hand, by decreasing the radius of an individual hole (or by tuning its refractive index between 1 and the refractive index of the slab), a donor defect state is excited and pulled into the bandgap from the air band.[27]

Acceptors tend to concentrate their electric field energy in regions where the large refrac-

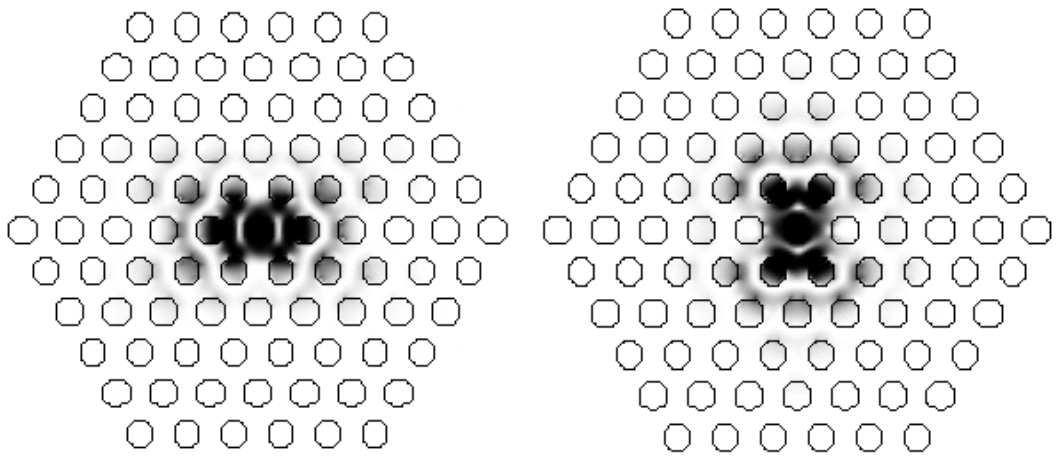

(a) (b)

Figure 1.5: Electric field intensity patterns of the (a) y-dipole and (b) x-dipole mode. The plotted intensity patterns are for the x-y plane at the middle of the slab.

tive index was located in the unperturbed PC, while the electric field energy of donors is concentrated in regions where there was air in the unperturbed PC, as shown in Figure 1.4. The donor defect state shown in Figure 1.4 is called a dipole mode. This mode has a double degeneracy[28] and can be separated into the x and y dipole modes, shown in Figure 1.5.

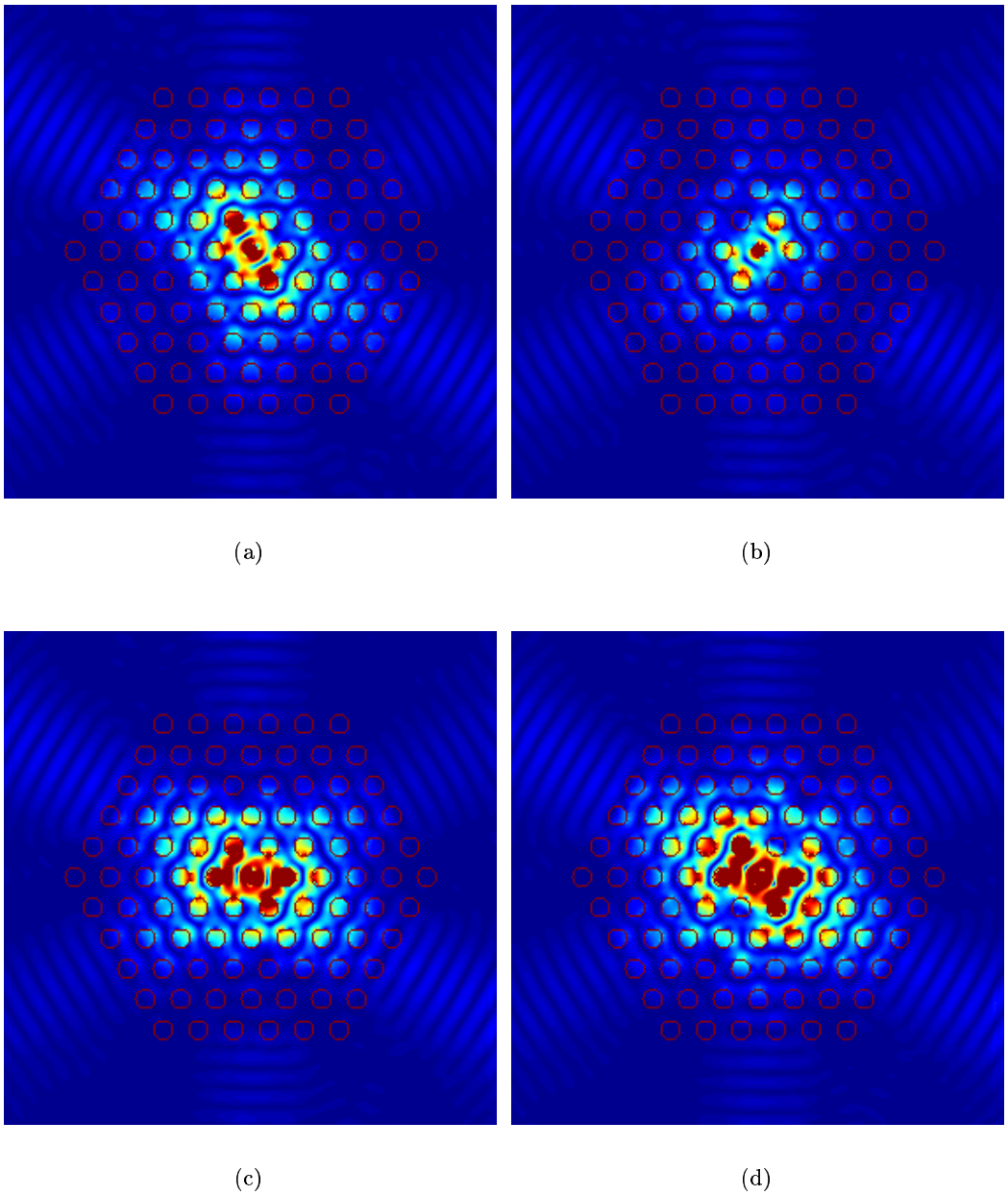

(a) (b)

(c) (d)

Figure 1.6: Electric field intensity patterns of the dipole mode as a function of time: (a) t=0; (b) t=T/8; (c) t=T/4; (d) t=3T/8, where $T = 2\pi c/\omega$ and ω is the radial frequency of the mode. The initial field is chosen in such a way that both x and y dipole modes are excited. The resulting field can be expressed as a superposition of the x and y dipole, with weighting factors depending on the initial field excitation.

The classification of the dipole mode into x and y states arises from the polarization of the electric field in the center of the defect. The radiation patterns of the x and y dipole modes resemble those of the x and y oriented electric dipoles, respectively, positioned in the center of the defect.

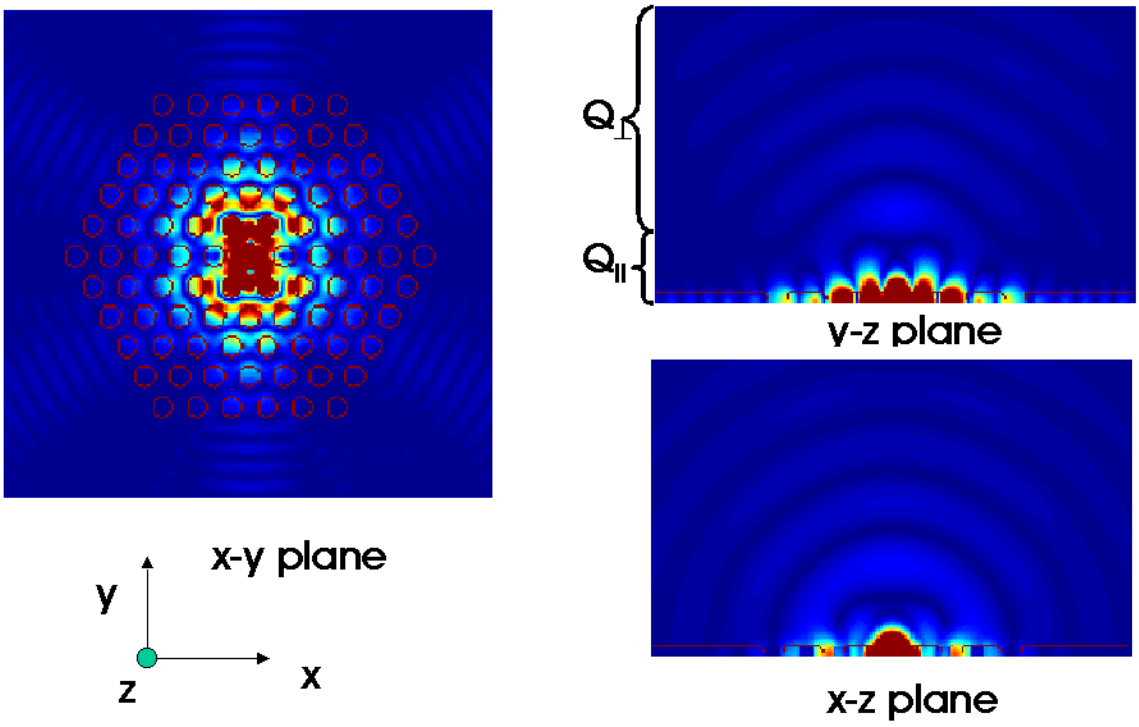

Figure 1.7: Radiation pattern of the x-dipole mode, in the x-y plane, and upper x-z and y-x half-planes. The separation of the total Q factor into $Q_{\perp}$ and $Q_{||}$ is also illustrated.

If only a single PC hole radius is reduced, the symmetry of the PC lattice is preserved and both x and y dipole modes can be excited at the same frequency. The resulting field can be expressed as a superposition of the x and y dipole, with weighting factors depending on the initial field excitation. If the two dipole components are excited with some phase difference, a rotation of the field as a function of time is observed, as shown in Figure 1.6. The energy switches in time between the x and y dipole modes, and the polarization of the field in the center of the defect rotates.

The total loss that a defect state suffers can be separated into the lateral (in-plane) loss,

and vertical (out-of-plane) loss. Similarly, the total quality factor of a defect mode can be expressed as a superposition of lateral and vertical quality factors:

$$\frac{1}{Q} = \frac{1}{Q_{||}} + \frac{1}{Q_{\perp}}. \tag{1.1}$$

$Q_{||}$ and $Q_{\perp}$ are inversely proportional to the lateral and vertical losses, respectively, as illustrated in Figure 1.7. In all of our calculations, the boundary for separation of vertical from lateral loss (i.e., the vertical quality factor $Q_{\perp}$ from the lateral quality factor $Q_{||}$) is positioned approximately at $\lambda/2$ from the surface of the membrane. For structures operating at bandgap frequencies, $Q_{||}$ increases as the number of PC layers around the defect increases, and the total quality factor Q approaches $Q_{\perp}$.[8] The vertical quality factor ($Q_{\perp}$) saturates after around five PC layers surrounding the defect. For our calculations, we also assume that $x = 0$, $y = 0$, $z = 0$ denotes the center of the cavity and $z = 0$ is the middle plane of the slab. For all presented analyses, five layers of PC holes surround the defect and the applied discretization of $a = 20$ points per lattice periodicity was used, unless noted otherwise.

1.4 Quality factors of single defect microcavities in planar photonic crystals

1.4.1 Changing the refractive index of a single hole

Microcavity formation via alteration of the refractive index of a single defect hole in triangular photonic crystal (PC) has been analyzed previously by our group.[28] In that analysis, we predicted that dipole-like donor states with quality factors up to 30000 should exist. We now believe that the quality factors of such microcavities are limited to several thousand, for reasons discussed below and presented in Reference 8. This discussion reveals the extreme sensitivity of microcavity quality factors to small distortions to the local PC geometry, which will later be used as a powerful design tool in cavity optimization.

In our previous work,[28] the mirror boundary conditions were applied in x, y and z directions to achieve an eight-fold reduction in the computational grid size. We have since realized that the manner in which even (symmetric) mirror boundary conditions are implemented

in our FDTD code results in numerical output that properly corresponds to an analyzed structure with slight deformations relative to the intended structure. For example, the combination of mirror boundary conditions used to select the x-dipole mode in a defect cavity leads to a deformation of the structure as shown in Figure 1.8. Holes on the x-axis are elongated in the y direction by 1 point in such a way that the distance between holes in x and y directions is preserved. Because hole-to-hole distances are preserved under this deformation, the half-spaces $y > 1/2$ and $y < -1/2$ actually maintain the unperturbed PC geometry when holes in the central row are elongated by 1/2 points both in the $\pm y$ directions. The symmetry of the PC surrounding the defect is therefore broken, and this contributes to artificially high Q factors for x-dipole modes. An even mirror BC was also applied in the z direction in our previous analysis, causing a slight increase of the thickness of the slab. The correct d/a ratios of the structures analyzed in Reference 28 would be 0.6, 0.46 and 1, instead the values of 0.53, 0.4 and 0.93, as noted there.

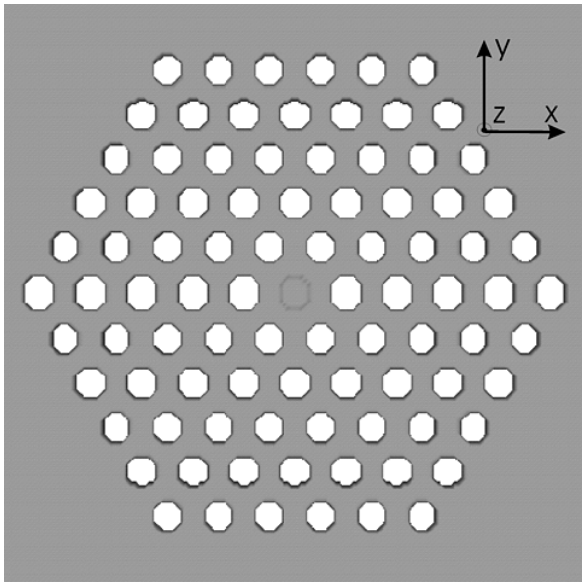

Figure 1.8: Deformation of the analyzed structure introduced by the application of mirror boundary conditions along the x and y axes and through the center of the defect. The applied mirror boundary conditions select the x-dipole mode, whose electric field pattern is shown in Figure 1.5. Holes on the x axis (in the central row, containing the defect) are elongated by 1 point in the y direction. The refractive index of the defect is $n_{defect} = 2.4$. Parameters of the structure are $r/a = 0.3$, $d/a = 0.6$ and in the used discretization $a = 15$.

The structure deformation is not the only problem caused by the application of mirror boundary conditions along the x and y axis. If we analyze the entire structure (without application of mirror BC's), but elongate the holes on the x axis by 1 point, the Q factor of the x-dipole mode increases to only about 4000. This means that the application of mirror BC at $x = 0$ and $y = 0$ planes causes additional effects that lead to the overestimation of Q factors. One of the reasons may be that the excited dipole mode does not have a symmetry described by the applied discretized mirror BC's. This may be partly due to the structure imperfection caused by discretization.

In order to avoid problems caused by the application of discretized mirror boundary conditions along the x and y axes, all analyses presented in this chapter are preformed by applying even mirror boundary conditions only to the lower boundary in the z direction. This reduces the computation size by one half and eliminates TM-like modes. Mur's absorbing boundary conditions are applied to all boundaries in x and y directions and to the upper boundary in z direction. To prove that the application of mirror BC at the lower z boundary does not change Q, we also analyzed the entire structures, with absorbing BC's applied to all boundaries and obtained the same results as in the analyses of one half of the structure.

For the exactly same set of parameters for which Q over 30000 was predicted in Reference 28 ($r/a = 0.3$, $d/a = 0.6$, $n_{defect} = 2.4$, $n_{slab} = 3.4$, 5 layers of holes around the defect and $a = 15$), we now calculate $Q_{||} = 2260$, $Q_{\perp} = 1730$ and $\frac{a}{\lambda} = 0.3137$ for the x-dipole mode, and $Q_{||} = 1867$, $Q_{\perp} = 1007$ and $\frac{a}{\lambda} = 0.3182$ for the y-dipole mode. The selection between the x and y dipole mode is made by applying the initial field distribution of appropriate symmetry. The difference in parameters of the two dipole modes comes partly from the asymmetry of the structure introduced by imperfect discretization. In a 2D PC with infinite slab thickness, these two modes would be degenerate.[28] In the thin slab, however, the y-dipole mode suffers more vertical scattering at the edges of holes and, therefore, has a lower $Q_{\perp}$.

1.4.2 Changing the radius of a single hole

The lithographic tuning of parameters of individual holes is a much simpler process than the control over the refractive index of a single hole. As mentioned previously and illustrated in Figure 1.4, acceptor defect states can be excited by increasing the radius of a single hole, while donor states can be excited by reducing the radius of a single hole. One can notice in the same figure that the electric field of the analyzed acceptor mode (monopole) is concentrated close to the edges of the large defect hole, which can lead to an increase in surface recombination losses. For this reason, some donor states may represent a better choice for the design of active devices, such as lasers or LEDs. Furthermore, for the design of optical microcavities for cavity QED with neutral atoms, a strong field intensity is required in the air region, where the atom can be trapped. Again, donor type states represent a better choice for these applications.

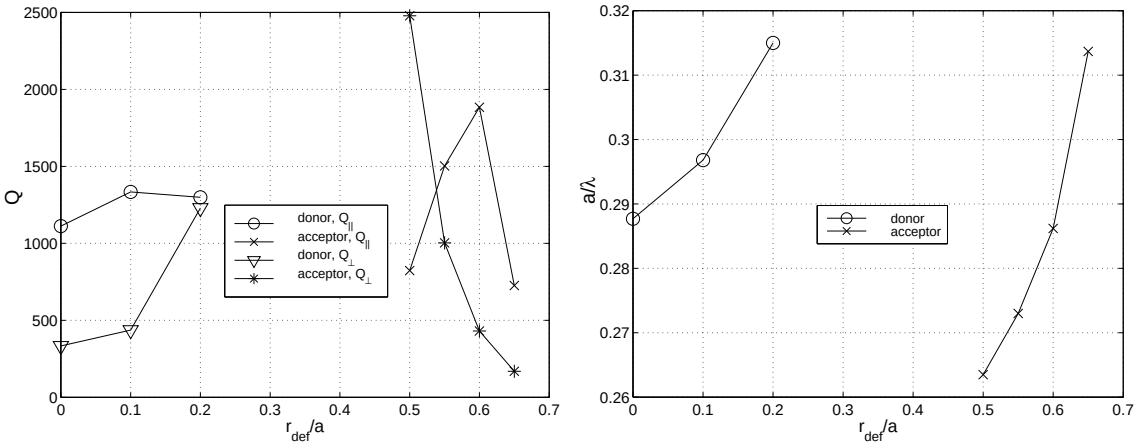

(a) (b)

Figure 1.9: Parameters of donor (dipole) and acceptor (monopole) modes in the single defect structure ($r/a = 0.3$, $d/a = 0.65$) as a function of the defect hole radius r_{def}: (a) Q factors; (b) frequency in units a/λ.

Parameters of acceptor (monopole) and donor (dipole) states as a function of the radius of the defect hole (r_{def}) are shown in Figure 1.9. In these plots, the parameters of photonic crystal are $r/a = 0.3$, $d/a = 0.65$ and $n = 3.4$ (the band diagram for this set of parameters

is shown in Figure 1.2). By tuning the radius of the defect hole, we also tune the frequency of the defect mode throughout the bandgap. In this process, we can optimize the quality factor of this mode, and maximize it at the value of around 2500.

A small increase in Q factors can be obtained by further reducing the radii of PC holes, as illustrated in Table 1.1 for dipole modes and a range of microcavity parameters. However, the reduction in hole size leads to a decrease in the size of the bandgap, a delocalization of the defect mode and an increase in its mode volume. On the other hand, the increase in r/a can lead to an increase in the bandgap and a reduction in lateral losses, as presented in Figure 1.3, but vertical scattering at the edges of holes also increases, and $Q_\perp$ drops. Therefore, it is important to find an optimum r/a which leads to small vertical losses, yet preserves good lateral confinement.

Even after the reduction in r/a, the maximum Q factors are still of the order of several thousand, which is not high enough for some of our applications (such as cavity QED). In later sections, we will present more sophisticated cavity designs that can lead to much higher Q factors.

Table 1.1: Q factors of dipole modes excited in microcavities formed by decreasing the radius of a single PC hole.

r/a	r_{def}/a	d/a	a/λ	$Q_{\|\|}$	$Q_\perp$
0.25	0.15	0.75	0.277	230	1840
0.25	0.2	0.75	0.284	116	3190
0.275	0.15	0.75	0.286	778	920
0.275	0.2	0.75	0.297	470	2078

1.5 Simple multi-defect cavities

Let us analyze simplest multi-defect cavities, produced by omitting multiple holes in a PC array. Since the main advantage of using photonic crystals over standard optoelectronic circuits is in the ability to localize light into small mode volumes, we will concentrate on small size cavities in the shapes of hexagons, rings and triangles, and with a side equal to $2a$. These structures are multi-mode with increased modal volumes, but they may

have advantages over single defect designs in some situations, such as for the fabrication of electrically pumped devices. However, we will see that these structures actually have modest Q factors, limited by mainly vertical losses.

Let us first consider a hexagon with a side equal to $2a$, produced by omitting multiple PC holes. The unperturbed PC has the following set of parameters: $r/a = 0.3$, $d/a = 0.65$, $n = 3.4$ and $a = 20$. One of the modes that could be excited in this hexagonal structure is a monopole shown in Figure 1.10. Its parameters are $a/\lambda = 0.2886$, $Q_{||} = 1547$ and $Q_{\perp} = 713$. The mode radiates laterally, in six ΓX directions. $Q_{\perp}$ is quite small, and, therefore, vertical scattering is very critical.

If we keep the central hole of this structure (in the center of a hexagon), thereby producing a ring with a side equal to $2a$, and excite the same mode as the one shown in Figure 1.10, its parameters are $a/\lambda = 0.29436$, $Q_{||} = 1581$ and $Q_{\perp} = 542$. Therefore, the mode senses the central hole only weakly and the overlap with air in it slightly increases the mode frequency. $Q_{||}$ remains unchanged, while $Q_{\perp}$ decreases slightly, due to increased vertical scattering at the edges of this extra hole.

Finally, let us analyze a triangle with a side of $2a$, and the mode shown in Figure 1.10. Parameters of this mode are $a/\lambda = 0.3086$, $Q_{||} = 352$ and $Q_{\perp} = 365$. Therefore, this type of the microcavity suffers from even larger out-of-plane losses.

Certainly, a more thorough analysis of these structures could be done to carefully scan the range of PC parameters, but our first results seem to indicate that simple multi-defect cavities of small size, produced by omitting multiple holes within the PC array, are not very good candidates for the design of high Q cavities.

1.6 Fractional edge dislocations in planar photonic crystals

Let us now study the lattice defect similar to the one produced by the application of even mirror BC in our original FDTD code. This type of defect has not been discussed previously, and we will call it *fractional edge dislocation*, by analogy with the edge dislocations in solid-state physics. The edge dislocations in solid-state physics are formed by adding extra planes of atoms to a crystal lattice. In this case, however, we add only a fraction of an extra plane

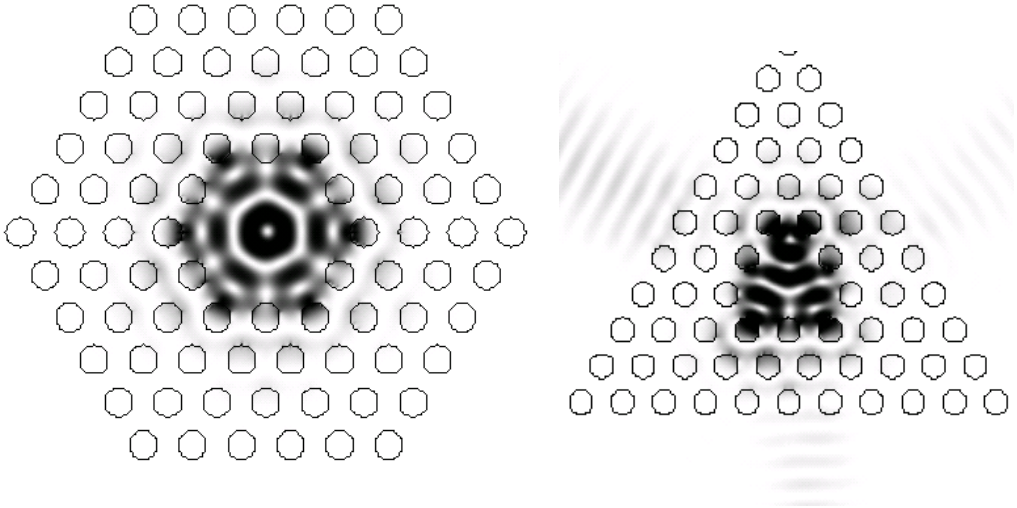

(a) (b)

Figure 1.10: Electric field intensity patterns of the modes excited in the large (a) hexagonal; (b) triangular microcavity.

of photonic crystal lattice atoms along the symmetry axis. For example, if the distance between lattice planes in some direction is l, we can insert a fraction of a lattice plane of the thickness fl, where $f < 1$. This is, naturally, impossible in atomic crystal lattices. As we will see in a moment, a dramatic improvement in Q factors over single defect microcavities can be obtained by introducing this type of lattice defect. The two previously introduced sets of PC parameters are again used here: (1) $n = 3.4$, $d/a = 0.75$ and $r/a = 0.275$; (2) $n = 3.4$, $d/a = 0.65$ and $r/a = 0.3$. They are, respectively, referred to as the 1st and 2nd set of parameters.

A microcavity structure consisting of a single defect and a fractional edge dislocation is shown in Figure 1.11. The structure in this Figure is based on the 1st set of PC parameters, but we present results of the analyses for both the 1st and 2nd set of PC parameters in this section. For all analyzed structures, a single defect is formed by reducing the radius of the central hole to $r_{def}/a = 0.2$, and a fractional edge dislocation is formed by elongating the holes along the x axis (including the defect hole) by p points in the y direction, in such a way that the distance between holes is preserved. We define p here as the elongation

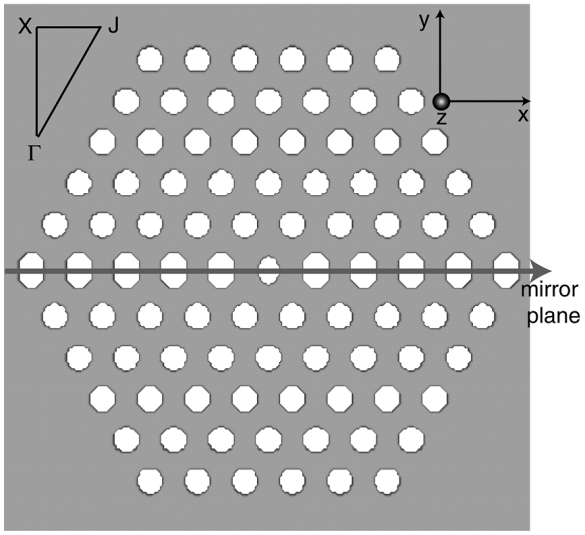

Figure 1.11: Microcavity structure consisting of a single defect (produced by reducing the radius of the central hole to $r_{def}/a = 0.2$ from $r/a = 0.275$) and a fractional edge dislocation of the order $p = 4$ parallel to the $y = 0$ plane. $a = 20$ in the applied discretization.

parameter. If we recall that the lattice periodicity a is equal to 20 computational points in the FDTD program units, the elongation step $\Delta p = 1$ corresponds to 5% of lattice periodicity. Therefore, the fractional edge dislocation of the order p is formed when the holes in the central row are elongated by $p/2$ points both in the $+y$ and $-y$ direction (i.e., elongated by p points total), but the half-spaces $y > p/2$ and $y < -p/2$ remain identical to the unperturbed PC. In other words: a total number of p discrete planes are inserted at $y = 0$.

The symmetry of the PC surrounding the defect is broken by this deformation, which separates the doubly degenerate x and y dipole modes in frequencies. The presented defect of the PC lattice spoils the Q factor of the y-dipole mode. On the other hand, for the x-dipole mode shown in Figure 1.12, this deformation leads to a significant Q improvement. Parameters of the x-dipole mode, as a function of the elongation parameter p, are shown in Figures 1.13 and 1.14. Therefore, by tuning p, the quality factor reaches values of over 10000. The mode volume V_{mode} does not change significantly with p and is approximately equal to $0.5(\frac{\lambda}{n})^3$. For structures operating at telecommunication wavelength $\lambda = 1550nm$, the elongation step $\Delta p = 1$ corresponds to approximately $23nm$. From Figure 1.13, it follows that even when the elongation is accidentally detuned by 20nm (i.e., p changed from

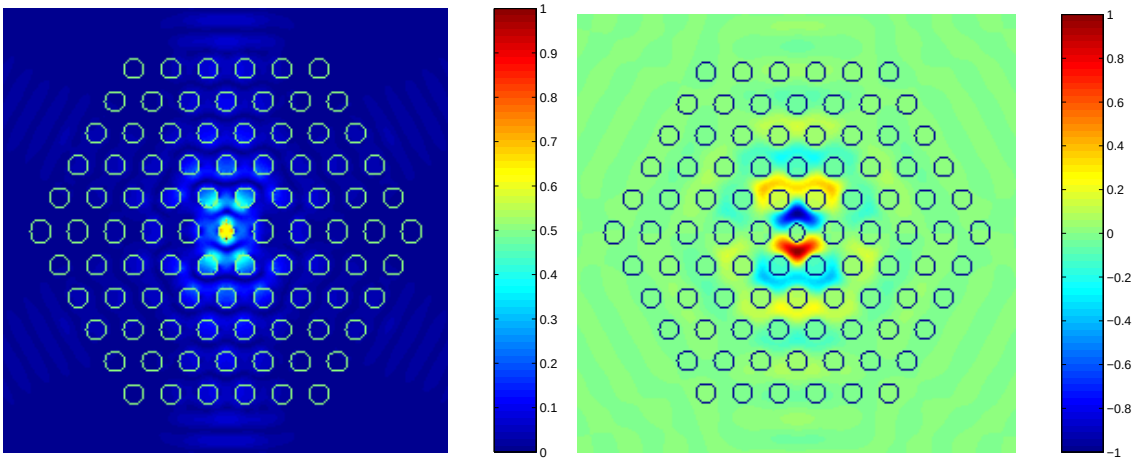

(a) (b)

Figure 1.12: (a) Electric field intensity and (b) z component of magnetic field of the x-dipole mode, excited in the structure where the radius of the central PC hole is reduced and fractional edge dislocation of the order $p = 2$ is added. Parameters of PC are described by the 1st set. The plotted intensity patterns are for the x-y plane in the middle of the slab.

2 to 3), Q still remains in the range of 10000. The insensitivity of Q to small variations in p is very important, since the small detuning in p during the fabrication process does not destroy properties of the structure. Thus, such structures are predicted to be relatively robust and manufacturable.

It is also interesting to note that the frequency of the mode decreases as p increases, even though the amount of low refractive index material increases. However, the net amount of low refractive index material does not matter. What matters more is where the low refractive index is positioned, relative to the unperturbed PC. The explanation of the decrease in frequency is very simple, if we recall the x-dipole mode pattern shown in Figure 1.12. This is a donor type defect mode, as previously stated, that concentrates its electric field energy density in low refractive index regions of the unperturbed PC. As p increases, layers of PC holes are moved away from the defect in the y direction. For example, the n-th layer of holes parallel to the x axis will now be positioned at $y = \pm na\sqrt{3}/2 \pm p/2$, instead of $y = \pm na\sqrt{3}/2$. Therefore, material with large refractive index (semiconductor) will now be positioned at places where the mode expects to "see" air, leading to a corresponding

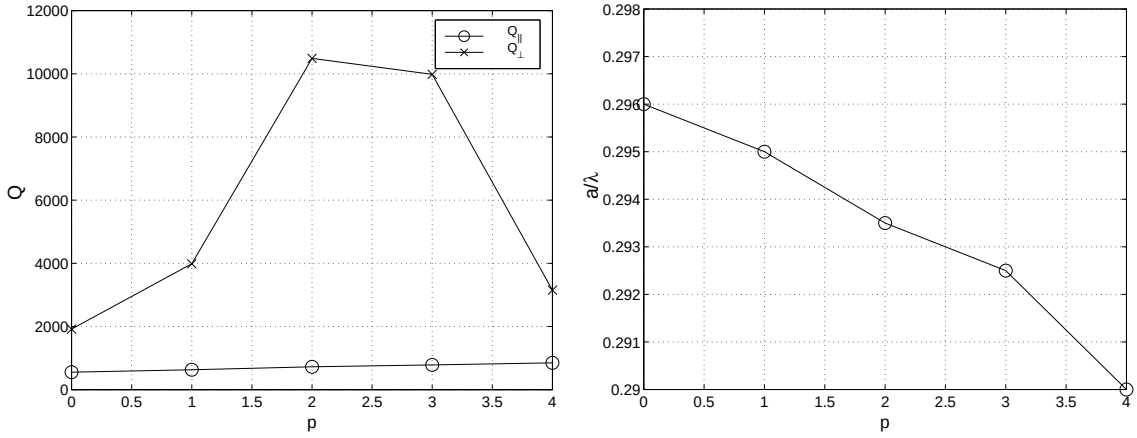

(a) (b)

Figure 1.13: Parameters of the x-dipole mode in a single defect structure as a function of the elongation parameter p. The PC has the 1st set of parameters and the defect is formed by reducing the radius of the central hole to $r_{def}/a = 0.2$. (a) Q factors; (b) frequency in units a/λ.

decrease in the mode's frequency.

Q factor improvements can also be achieved by adding fractional edge dislocations to the previously described structures where the refractive index of the central hole is tuned. Recall that the analyzed structure had $d/a = 0.6$, $r/a = 0.3$, $n = 3.4$, $n_{defect} = 2.4$ and $a = 15$. The variation of Q factor and a/λ of the x-dipole mode in this structure, as a function of the discrete elongation parameter p, as well as the dependence of Q factor on the number of PC layers around the defect for $p = 3$, are shown in Figures 1.15 and 1.16. The analyzed x-dipole mode mostly resonates in the direction of y axis, i.e., in the ΓX direction of photonic crystal. The tuning of the elongation parameter p is, therefore, analogous to tuning of a spacer in the micropost cavity, which leads to tuning of mode's frequency and Q factor. By increasing the number of PC periods around the defect, the total quality factor Q approaches $Q_{\perp}$, as shown in Figure 1.16. It is important to note that $Q_{||}$ does not increase exponentially with the number of PC layers around the defect, as noted previously in Reference 28. Instead, it saturates at large number of PC layers. The reason is in the choice of a boundary for separation of $Q_{\perp}$ from $Q_{||}$, positioned at

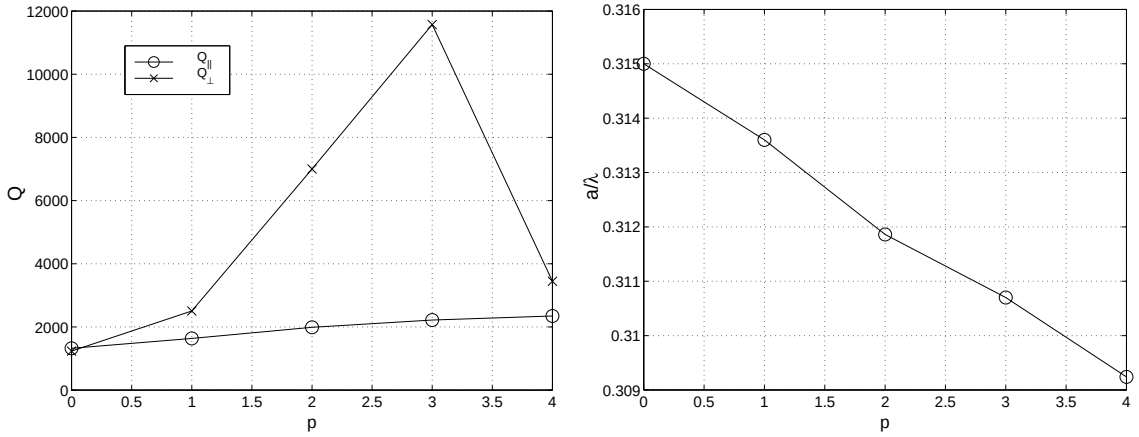

(a) (b)

Figure 1.14: Parameters of the x-dipole mode in a single defect structure as a function of the elongation parameter p. The PC has the 2nd set of parameters and the defect is formed by reducing the radius of the central hole to $r_{def}/a = 0.2$. (a) Q factors; (b) frequency in units a/λ.

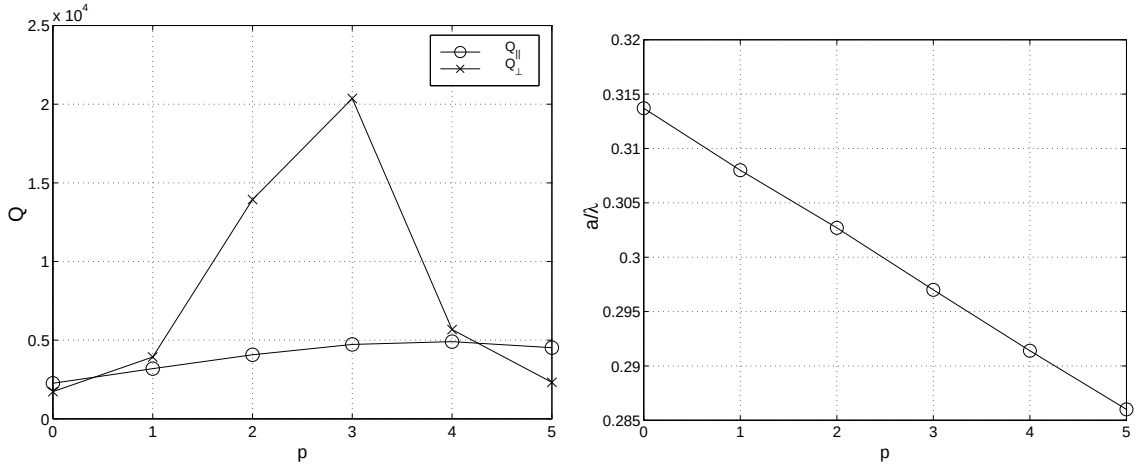

(a) (b)

Figure 1.15: (a) Q factors and (b) frequencies of x-dipole modes in a single defect structure, as a function of the elongation parameter p. Defect is formed by changing the radius of the central hole to $n_{defect} = 2.4$. Parameters of PC are $d/a = 0.6$, $r/a = 0.3$, $n = 3.4$ and $a = 15$.

approximately $\lambda/2$ from the surface of the membrane. From the radiation pattern of the x-dipole mode shown in Figure 1.7, we can see that some portion of the out-of-plane loss (mostly in the x direction) still gets collected in $Q_{||}$. This loss cannot be suppressed by increasing the number of PC layers around the defect, and it determines the value at which $Q_{||}$ saturates. However, a much larger out-of-plane loss is collected in $Q_{\perp}$, which ultimately determines the total quality factor Q.

In Figures 1.13, 1.14 and 1.15 one can observe that an increase in the elongation parameter p can be used to tune the $Q_{\perp}$ factor of a mode, but it also leads to a decrease in the dipole mode's frequency. This implies that by increasing p, the mode is pulled deeper into the bandgap, away from the air band edge, which leads to its better lateral confinement and an increase in its $Q_{||}$. Therefore, we can simultaneously achieve a reduction in vertical losses and an improvement in lateral confinement (i.e., an increase in both $Q_{\perp}$ and $Q_{||}$, and a reduction in the mode volume).

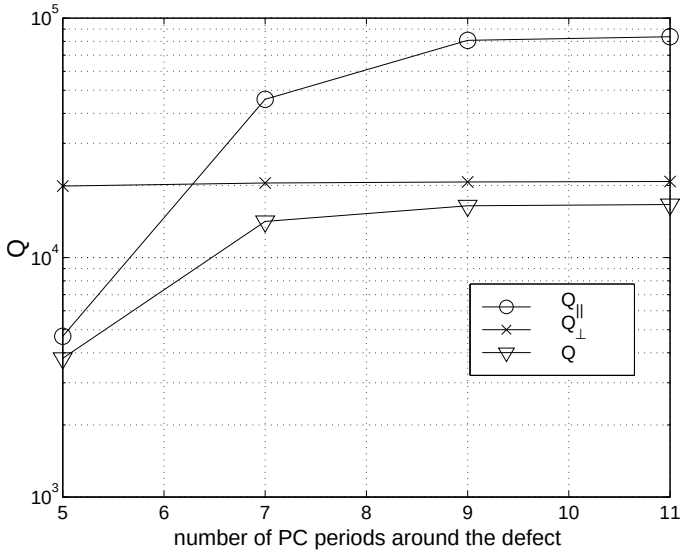

Figure 1.16: Q factor for $p = 3$, as a function of the number of PC layers around the defect. Defect is formed by changing the refractive index of the central hole to $n_{defect} = 2.4$. Parameters of PC are $d/a = 0.6$, $r/a = 0.3$, $n = 3.4$ and $a = 15$.

Since the mode frequency decreases as a function of the elongation parameter p, it is desirable to start in the elongation process with a mode whose frequency is close to the upper

boundary of the bandgap, allowing enough space to achieve an optimum $Q_\perp$ within the bandgap when the structure is tuned. In that case, the lateral confinement is preserved and $Q_{||}$ can be improved by increasing the number of PC layers around the defect.

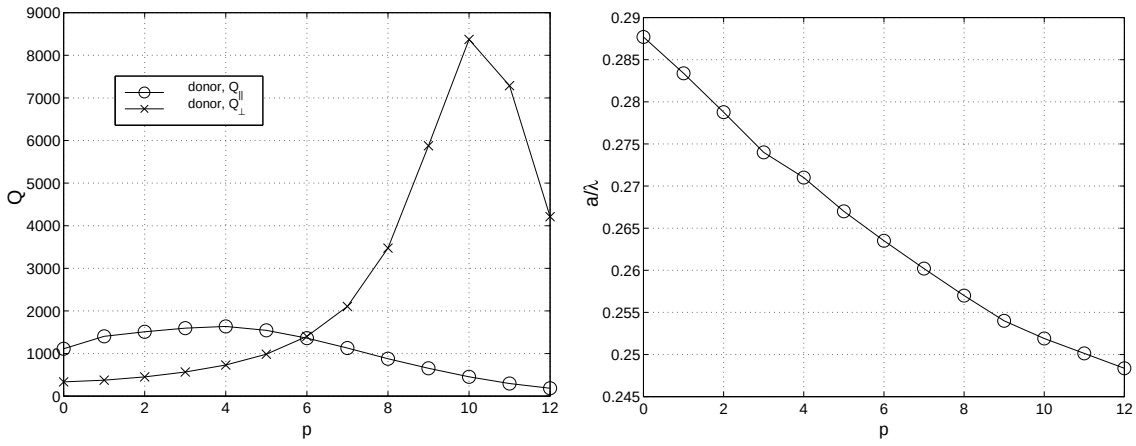

(a) (b)

Figure 1.17: Parameters of the x-dipole mode in the single defect structure ($r/a = 0.3$, $d/a = 0.65$, $r_{def}/a = 0$, $n = 3.4$ and $a = 20$) as a function of the elongation parameter p: (a) Q factors; (b) frequency in units a/λ.

The opposite example is illustrated in Figure 1.17. We analyze the x-dipole mode in a single defect structure containing a fractional edge dislocation. The used PC has the 2nd set of parameters and the single defect is formed by omitting the central hole, i.e., $r_{def}/a = 0$. Recall that the bandgap in the planar PC with these parameters extends from approximately $a/\lambda = 0.26$ to 0.33, as shown in Figure 1.2. Therefore, for $p = 6$ the defect mode already enters the air band. However, a weak localization of the x-dipole mode still exists for $p > 6$, because the mode is mostly composed of the wavevectors at the X point, where the dielectric band boundary is somewhat lower (at about $a/\lambda = 0.23$). Although X components are dominant in the x-dipole mode, the localized defect mode consists of many different wavevector components, as will be obvious from the Fourier transforms of the mode profiles presented later in this chapter. Therefore, the mode can couple to the air band mode at the J point after $p = 4$, it looses the lateral confinement and its $Q_{||}$ drops. Even though $Q_\perp$ reaches a value larger than 8000 at $p = 10$, this happens at the frequency

which is already deep in the dielectric band. Therefore, the mode is limited by lateral losses at this point and an improvement in $Q_\perp$ does not influence the overall Q. For that reason, this particular structure can only be used for small Q improvements in the range of $p \leq 4$.

1.7 Fractional edge dislocations and tuning of holes around the defect

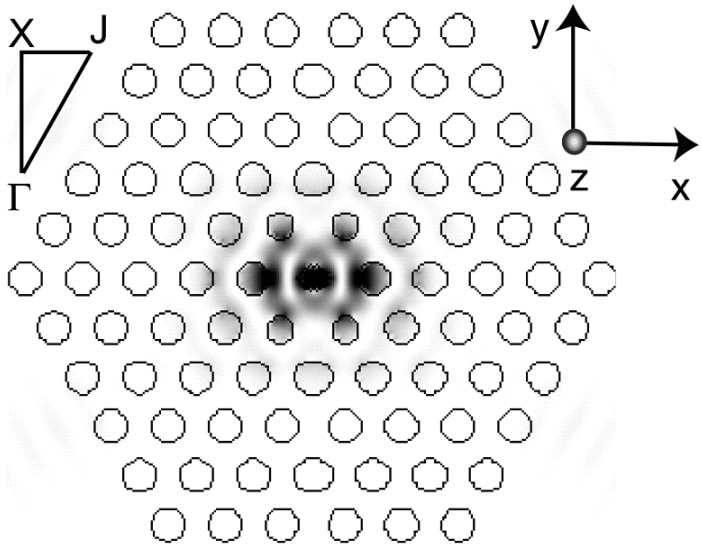

Figure 1.18: Electric field intensity pattern of the y dipole mode excited in the cavity where four holes closest to the defect in ΓJ directions are tuned. Their radii are reduced to $r_1/a = 0.225$ and they are simultaneously moved away from the defect in ΓJ direction by $r - r_1$. The radius of the central hole is $r_{def}/a = 0.2$ and PC has the first set of parameters. The fractional edge dislocation ($p = 2$, parallel to the $x = 0$ plane) is also present.

One can improve the Q factors even further by simultaneously tuning holes next to the defect and adding fractional edge dislocations.[8] Let us form the microcavity starting from the planar PC with either the 1st ot the 2nd set of parameters. The radius of the central hole is reduced to $r_{def} = 0.2a$ and the radii of the four closest holes in ΓJ directions are reduced to $r_1 = 0.225a$, or $r_1 = 0.25a$, for the 1st or 2nd set of PC parameters, respectively. These four holes are simultaneously moved away from defect, by $r - r_1$ in the ΓJ directions, which preserves the distance between them and the next nearest neighbors in the same

directions. This design improves the Q factor of the y-dipole mode and spoils the Q of the x-dipole mode. To improve Q factors even further, we elongate holes located on the y axis by p points in the x direction (i.e., add fractional edge dislocations parallel to $x = 0$ plane). The electric field intensity distribution of the y-dipole mode for $p = 2$ and the first set of PC parameters is shown in Figure 1.18. The dependence of the mode frequency and Q factor on parameter p is shown in Figure 1.19. V_{mode} does not change significantly with p and is in the range between $0.44(\frac{\lambda}{n})^3$ and to $0.59(\frac{\lambda}{n})^3$. Therefore, a Q factor over 30000 can be achieved in this structure for the dipole defect mode.

1.8 The effect of fractional edge dislocations

1.8.1 Relation between the Q factor and the Fourier transform of a mode

The 3D FDTD analysis can provide us with the near field distribution of the analyzed microcavity. The FDTD analysis of the far field would require large amounts of computer memory, and would be very computationally inefficient. However, we can compute the far field starting from the known near field distribution. Any wavefront can be considered as a source of secondary waves that add to produce distant wavefronts, according to Huygens principle. Let us assume that we know the field distribution across the surface S, positioned in the near field and above the free standing membrane, as in Figure 1.20. Our goal is to estimate the far field at the observation point O. The far fields can be considered as arising from the equivalent current sheets at the surface S.[29] For example, let S be the plane positioned at $z = 0$, in parallel to the surface of the membrane, and at a small distance Δz from it. This choice of surface S will allow us to relate the Q factor of a mode to the Fourier transform of its field pattern. The equivalent sources in the plane S can be represented in terms of the surface electric ($\vec{J}_s$) and magnetic ($\vec{M}_s$) currents:

$$\vec{J}_s = \hat{n} \times \vec{H} = -\hat{x}H_y + \hat{y}H_x \tag{1.2}$$

$$\vec{M}_s = -\hat{n} \times \vec{E} = \hat{x}E_y - \hat{y}E_x, \tag{1.3}$$

where $\hat{n}$ is a normal to the surface S. In a homogeneous, isotropic medium above S, a retarded potential $\vec{A}$ and a second retarded potential $\vec{F}$ can be estimated from the previously introduced surface currents:

$$\vec{A} = \mu_0 \int_S \frac{\vec{J}_s e^{-ikr}}{4\pi r} dS \tag{1.4}$$

$$\vec{F} = \epsilon_0 \int_S \frac{\vec{M}_s e^{-ikr}}{4\pi r} dS, \tag{1.5}$$

where k is defined as $k = \frac{2\pi}{\lambda} = \frac{\omega}{c}$ (λ is the mode wavelength measured in air) and r is the distance between the point where the potentials are evaluated and the surface element dS (i.e., between the points O and P).

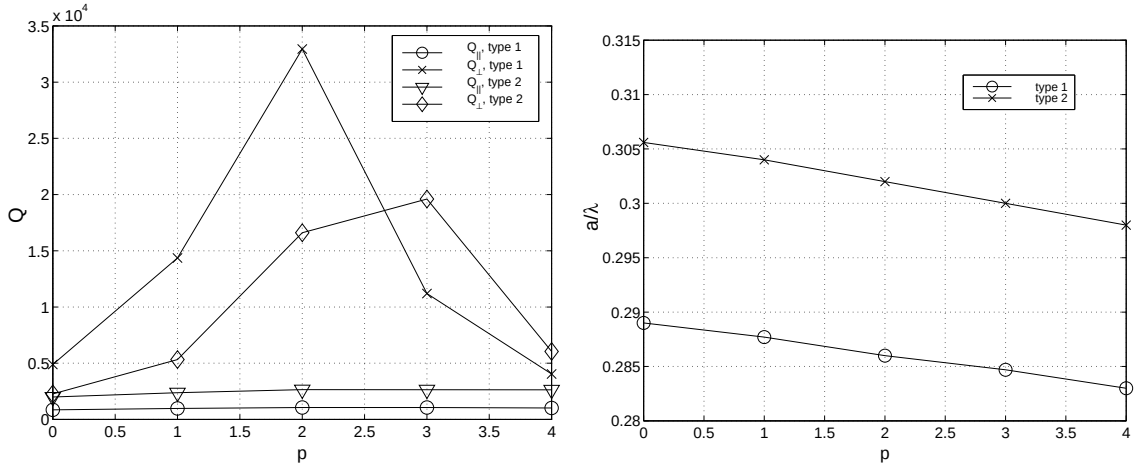

(a) (b)

Figure 1.19: Parameters of the y-dipole mode in the structure where four holes in ΓJ directions are tuned (as shown in Figure 1.18), as a function of the elongation parameter p: (a) Q factors; (b) frequency in units a/λ. The structure has either the first of second set of PC parameters, labeled as type 1 and type 2, respectively.

From Figure 1.20 it follows that $r \cong r_0 - r' cos(\psi)$. Let us now introduce radiation vectors $\vec{L}$ and $\vec{N}$:

$$\vec{N} = \int_S \vec{J}_s e^{ikr'cos(\psi)} dS \tag{1.6}$$

$$\vec{L} = \int_S \vec{M}_s e^{ikr'cos(\psi)} dS \tag{1.7}$$

Then we have

$$\vec{A} = \mu_0 \frac{e^{-ikr_0}}{4\pi r_0} \vec{N} \tag{1.8}$$

$$\vec{F} = \epsilon_0 \frac{e^{-ikr_0}}{4\pi r_0} \vec{L} \tag{1.9}$$

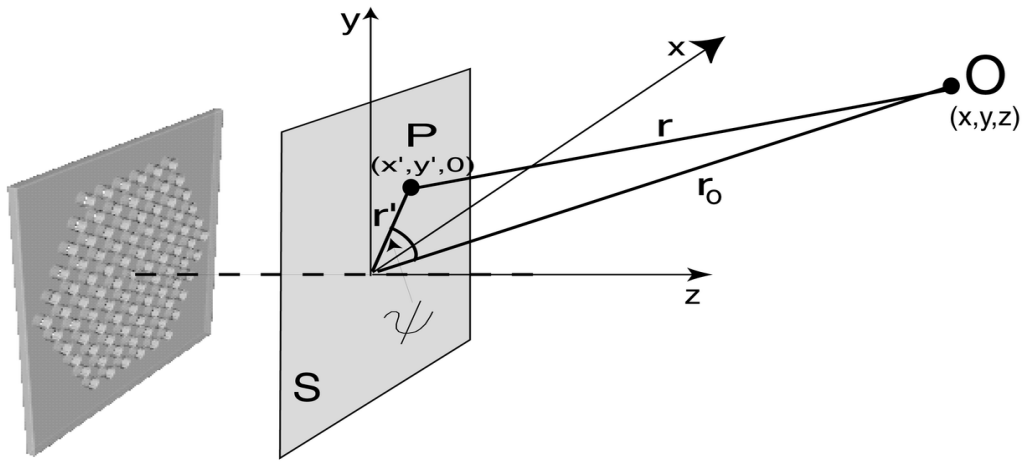

Figure 1.20: Estimating the radiation field at the observation point O from the known near field at the surface S.

From Figure 1.20 we also have

$$kr'cos(\psi) = \frac{k}{r_0}(xx' + yy'), \tag{1.10}$$

where $(x', y', 0)$ are the coordinates of the point P in the plane S and (x, y, z) are the

coordinates of the observation point O.

From the equations 1.6 and 1.7 it follows that radiation vectors $\vec{N}$ and $\vec{L}$ represent the 2D Fourier transforms of surface currents $\vec{J}_s$ and $\vec{M}_s$, evaluated at the value of the wave-vector $\vec{k}_{||} = k(x/r_o\hat{x} + y/r_o\hat{y})$ (in rectangular coordinates), i.e., $\vec{k}_{||} = k\sin\theta(\cos\phi\hat{x} + \sin\phi\hat{y})$ in circular polar coordinates:

$$\vec{N} = FT_2(\vec{J}_s)\Big|_{\vec{k}_{||}=k(\frac{x}{r_0},\frac{y}{r_0})} \tag{1.11}$$

$$\vec{L} = FT_2(\vec{M}_s)\Big|_{\vec{k}_{||}=k(\frac{x}{r_0},\frac{y}{r_0})} \tag{1.12}$$

$$\begin{aligned} FT_2(f(x,y)) &= \iint d_x d_y f(x,y) e^{i\vec{k}_{||}\cdot(x,y)} = \\ &= \iint d_x d_y f(x,y) e^{i(k_x x + k_y y)} \end{aligned} \tag{1.13}$$

Components of radiation vectors can, therefore, be expressed in terms of the Fourier transforms of the field components at the surface S:

$$N_x = -FT_2(H_y)\Big|_{\vec{k}_{||}} \tag{1.14}$$

$$N_y = FT_2(H_x)\Big|_{\vec{k}_{||}} \tag{1.15}$$

$$L_x = FT_2(E_y)\Big|_{\vec{k}_{||}} \tag{1.16}$$

$$L_y = -FT_2(E_x)\Big|_{\vec{k}_{||}} \tag{1.17}$$

$$\vec{k}_{||} = k(\frac{x}{r_0},\frac{y}{r_0}) = k\sin\theta(\cos\phi\hat{x} + \sin\phi\hat{y}) \tag{1.18}$$

It is important to note that for any observation point O, the previously introduced wave-vector $\vec{k}_{||}$ lies within the light cone (i.e., $|\vec{k}_{||}| \leq k$, where $k = \frac{2\pi}{\lambda}$). *Therefore, radiation vectors are purely determined by Fourier components located within the light cone.*

Far fields can be expressed in terms of retarded potentials:

$$\vec{E} = -i\omega\vec{A} - \frac{i\omega}{k^2}\nabla(\nabla\cdot\vec{A}) - \frac{1}{\epsilon_0}\nabla\times\vec{F} \tag{1.19}$$

$$\vec{H} = -i\omega\vec{F} - \frac{i\omega}{k^2}\nabla(\nabla\cdot\vec{F}) - \frac{1}{\mu_0}\nabla\times\vec{A} \tag{1.20}$$

Under the assumption that all terms in fields decaying faster than $1/r_o$ can be neglected, the electric field components at an arbitrary point O are

$$E_\theta = \eta H_\phi = -i\frac{e^{-ikr_o}}{2\lambda r_o}(\eta N_\theta + L_\phi) \tag{1.21}$$

$$E_\phi = -\eta H_\theta = i\frac{e^{-ikr_o}}{2\lambda r_o}(-\eta N_\phi + L_\theta) \tag{1.22}$$

$$\eta = \sqrt{\frac{\mu_o}{\epsilon_o}}, \tag{1.23}$$

where (r_o, θ, ϕ) represent the coordinates of the point O in the spherical polar coordinate system. The radiation intensity (power per unit solid angle) is then equal to[29]

$$K(\theta,\phi) = \frac{\eta}{8\lambda^2}\left(\left|N_\theta + \frac{L_\phi}{\eta}\right|^2 + \left|N_\phi - \frac{L_\theta}{\eta}\right|^2\right), \tag{1.24}$$

and the total averaged radiated power into the half-space $z > 0$ is given by

$$P_1 = \int_0^{\pi/2}\int_0^{2\pi} d_\theta d_\phi sin(\theta) K(\theta,\phi) \tag{1.25}$$

The radiation vectors in spherical polar coordinates can be expressed from their components in rectangular coordinates:

$$N_\theta = (N_x cos\phi + N_y sin\phi)cos\theta \tag{1.26}$$

$$N_\phi = -N_x sin\phi + N_y cos\phi, \tag{1.27}$$

where N_x, N_y, L_x and L_y were previously given as the 2D Fourier transforms of the appropriate field components tangential to the surface S. *Therefore, just by knowing the Fourier transforms of the tangential field components at the plane S, we can evaluate the total averaged radiated power and the far field distribution. Furthermore, the radiated power depends only on the wave-vector components located within the light cone. Therefore, the reduction in radiation loss and improvement in Q factor can be achieved by suppressing the Fourier components within the light cone, or by redistributing them outside the light cone.*

In the case when most of the radiated power is collected at vertical incidence (i.e., at small θ), the expression 1.25 can be simplified as follows:

$$\begin{aligned} P_2 &= \frac{\eta}{8\lambda^2 k^2} \iint\limits_{|\vec{k}_{||}|\leq k} d\vec{k} \left(\left| N_x + \frac{L_y}{\eta} \right|^2 + \left| N_y - \frac{L_x}{\eta} \right|^2 \right) \\ &= \frac{\eta}{8\lambda^2 k^2} \iint\limits_{|\vec{k}_{||}|\leq k} d\vec{k} \left(\left| FT_2(H_y) + \frac{1}{\eta} FT_2(E_x) \right|^2 + \left| FT_2(H_x) - \frac{1}{\eta} FT_2(E_y) \right|^2 \right) \end{aligned} \tag{1.28}$$

The integral of the cross-terms in the equation 1.28 gives approximately the radiated power. This can be proved easily starting from the expansion of fields in terms of the Fourier components and the expression for the radiated power as an integral of the z component of the Poynting vector $\vec{\Gamma}$ over the surface S. This leads to the following expression for the averaged radiated power:

$$P_3 = 2\frac{\eta}{8\lambda^2 k^2} \iint\limits_{|\vec{k}_{||}|\leq k} d\vec{k} \left(|FT_2(H_x)|^2 + |FT_2(H_y)|^2 + \frac{1}{\eta^2}|FT_2(E_x)|^2 + \frac{1}{\eta^2}|FT_2(E_y)|^2 \right) \tag{1.29}$$

It is important to note that if some field component $u(x, y)$ is odd with respect to the x coordinate (i.e., $u(x, y) = -u(-x, y)$), then its Fourier transform must be equal to zero for any point in the Fourier space with $k_x = 0$. Similarly, any field component which is odd with respect to the y coordinate has a Fourier transform which is zero for any point with $k_y = 0$.

Let us introduce the radiation factor RF which is directly proportional to the radiated power P:

$$RF_i = \frac{P_i}{W}, i = 1, 2, 3..., \tag{1.30}$$

where W represents the total energy of a mode in the half-space above the middle of the membrane. The Q factor of a mode can be expressed as

$$Q = \omega \frac{W}{P} = \frac{\omega}{RF} \tag{1.31}$$

1.8.2 The effect of fractional edge dislocations on the Q factor of the dipole mode in free standing membrane

We consider here the same microcavities presented previously in this chapter. The unperturbed photonic crystal parameters are $r/a = 0.275$, $d/a = 0.75$ and $n = 3.4$, where r, a, d and n represent the hole radius, the periodicity of the triangular lattice, the thickness of the slab and the refractive index of the semiconductor material, respectively. In the FDTD method we apply the disretization of 20 pixels per periodicity a. Therefore, a fractional edge dislocation of order $p = 1$ corresponds to the insertion of extra material whose thickness is equal to $1/20a$. In the microcavity of our interest the central hole radius is decreased to $r_{def}/a = 0.2$ and a fractional edge dislocation of order p is applied along the x axis, as shown in Figure 1.11. Field components of the x-dipole mode in the analyzed structure are shown in Figure 1.21, as a function of the elongation parameter p. For the x-dipole mode, E_x and B_y components are even, while E_y and B_x components are odd with respect to both symmetry axes x and y. Therefore, it is expected that E_y and B_x (i.e., L_x and N_y) do not contribute significantly to the radiated power in this case, since their Fourier transforms are equal to zero along both k_x and k_y axes. This is also illustrated in Figure 1.22. Therefore, in the case of the analyzed x-dipole mode, we can approximate the expression 1.29 even further:

$$P_4 = 2\frac{\eta}{8\lambda^2 k^2} \iint\limits_{|\vec{k}_{||}| \leq k} dk_x dk_y \left(\left| FT_2(H_y) \right|^2 + \frac{1}{\eta^2} |FT_2(E_x)|^2 \right) \tag{1.32}$$

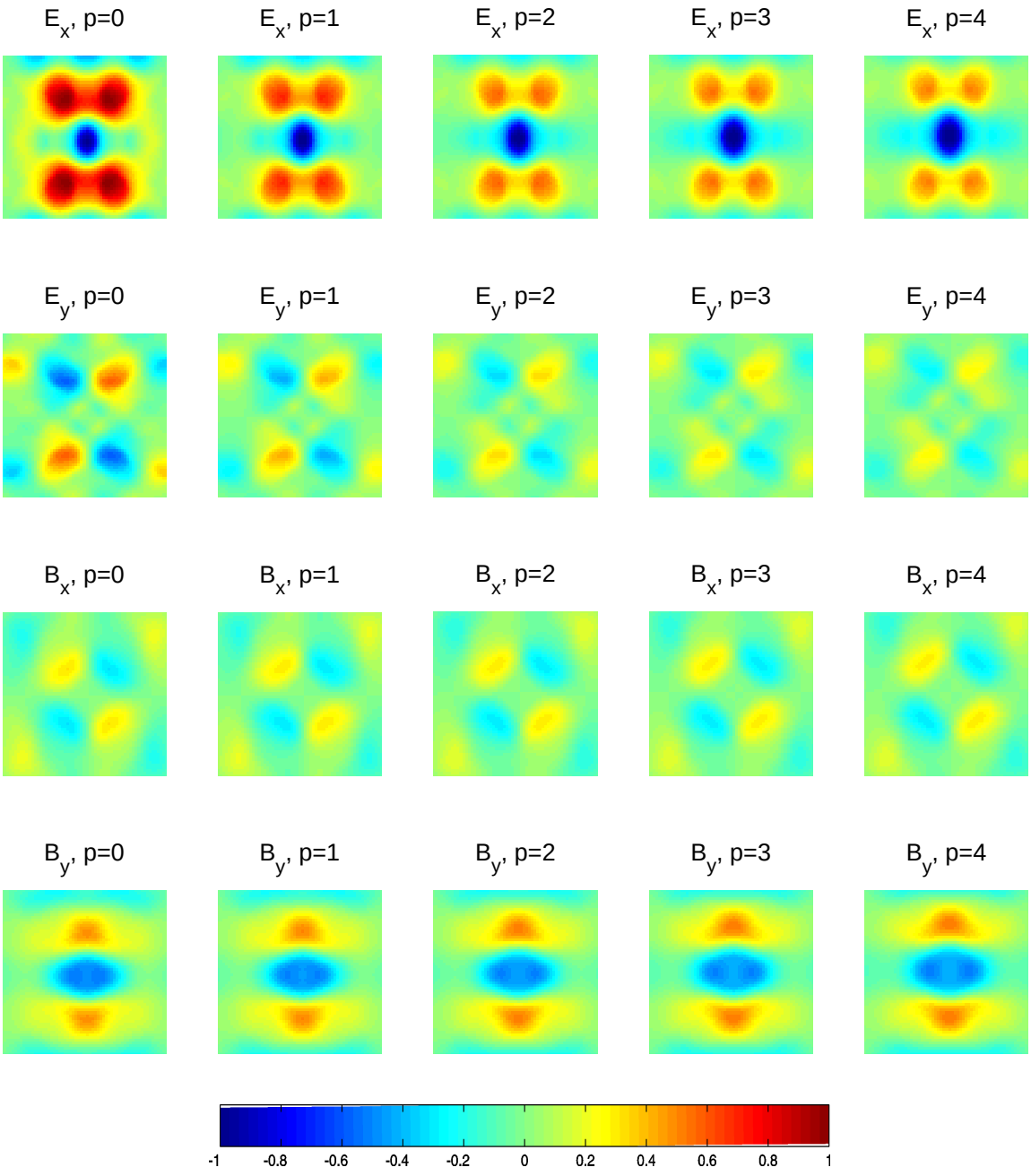

Figure 1.21: Field components of the x-dipole mode at the surface S positioned at approximately $d/4$ from the surface of the membrane. The analyzed structure is shown in Figure 1.11.

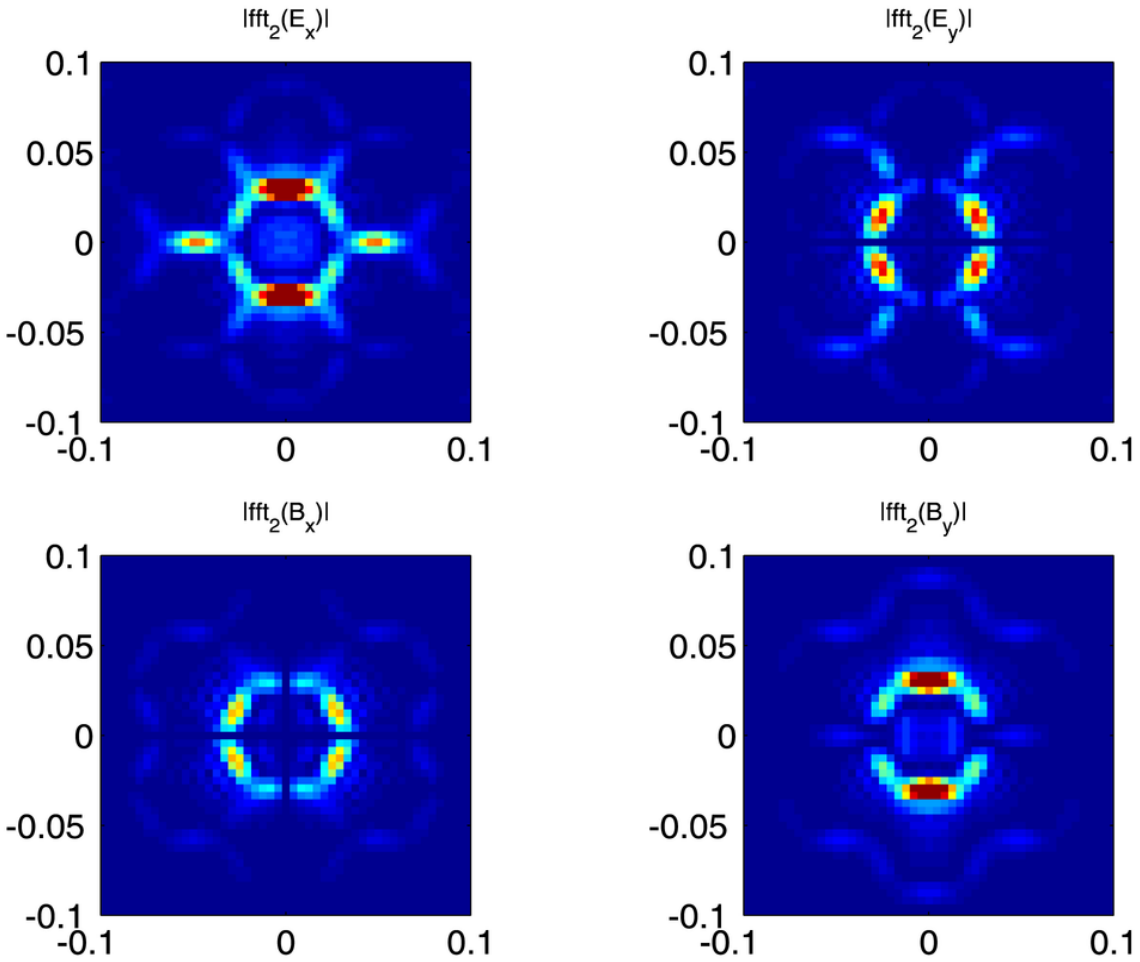

Figure 1.22: 2D Fast Fourier Transforms (fft_2) of the field components of the x-dipole mode in the structure from Figure 1.11. A fractional edge dislocation is of the order $p = 0$ in this case. The light cone can be respresented as a disk with the radius approximately equal to 0.015. The horizontal and vertical axes correspond to $\frac{k_x}{2\pi}$ and $\frac{k_y}{2\pi}$, respectively.

In order to minimize the radiated power, it is necessary to minimize (within the light cone) the Fourier transforms of the even field components E_x and B_y. In general case, these Fourier transforms are non-zero at small values of $|\vec{k}_{||}|$ (i.e., in the light cone). However, they can be minimized by balancing the intensities of positive and negative field lobes. Indeed, we can observe in Figure 1.21 that by varying the elongation parameter p, we also tune the sizes of the central (negative) lobes in E_x and B_y, as well as the intensity distribution between the positive and negative lobes. Therefore, the tuning in p is expected to lead to tuning in Fourier transforms of the even field components, and subsequently to

tuning in radiated powers.

The Fourier components of the x-dipole mode in the structure with $p = 0$ are shown in Figure 1.22. When the elongation parameter p changes in the analyzed range from 0 to 4, peaks in the Fourier space preserve their position, but their intensities are tuned. This can be observed in Figure 1.23. Clearly, Fourier components within the light cone are minimized for $p = 2$, where Q factor reaches its maximum. *Therefore, the optimization of Q factor of the dipole mode (after the application of fractional edge dislocations) is a result of suppression of the wave-vector components within the light cone. This suppression is a product of balancing between the energies of the positive and negative field lobes of the even field components. The Q factor optimization is achieved in this case without a significant mode delocalization.*

The radiation factors and Q factors are evaluated using the expressions derived previously

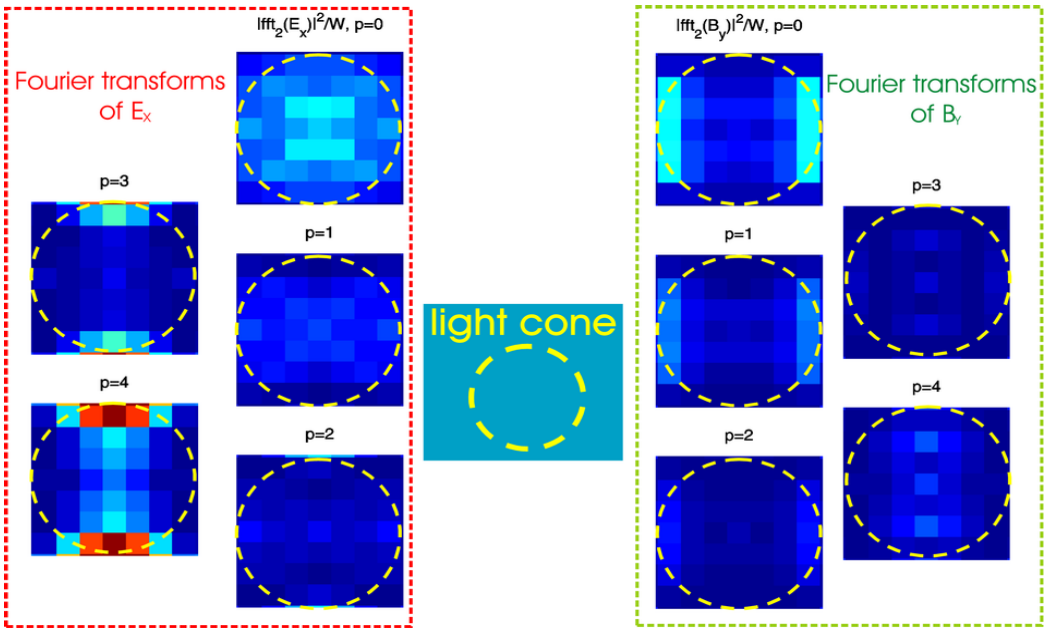

Figure 1.23: 2D Fourier transforms of the even field components of the x-dipole mode in the structure shown in Figure 1.11, as a function of the elongation parameter p. The light cone can be respresented as a disk inscribed into each square. Clearly, the intensities of Fourier transforms within the light cone are minimized for $p = 2$, where Q factor reaches its maximum.

and results are shown in Figure 1.24. A good agreement with Q factors calculated in the FDTD simulations is observed.

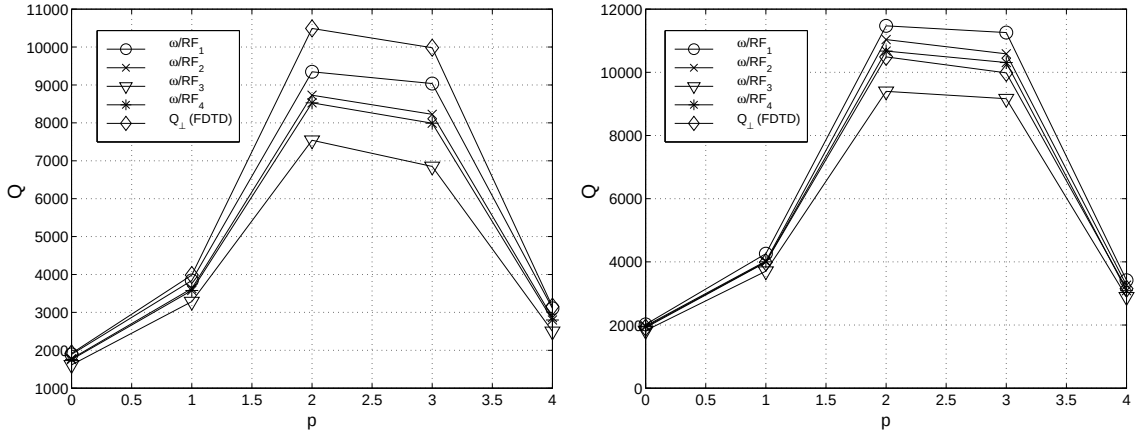

Figure 1.24: Q factors estimated from the FDTD, or from the Fourier transforms of the tangential field components. The analyzed structure has the following set of parameters: $r/a = 0.275$, $d/a = 0.75$, $n = 3.4$, $a = 20$, $r_{def}/a = 0.2$, and fractional edge dislocations of order p are added along the x axis. The plane S is positioned: (a) directly above the surface of the membrane, at a distance equal to $d/4$ from it; (b) at a distance equal to $\lambda/2$ from the surface of the membrane.

In Figure 1.24(a), $Q_\perp$ factors calculated using the FDTD are somewhat larger than Q factors calculated using the method presented in this article, because $Q_\perp$ includes only the radiation loss above the plane positioned at approximately $\lambda/2$ from the surface of the membrane. As we have discussed in our previous publication,[8] this approach excludes some small portion of the radiation loss, and the total Q factor achievable by increasing the number of the PC layers around the defect is somewhat smaller than $Q_\perp$. If we position the plane S at $\lambda/2$ from the surface of the membrane and repeat the previous calculations, a much better agreement with $Q_\perp$ is achieved, as shown in Figure 1.24(b). Radiation factors RF_2, RF_3 and RF_4 are estimated under the assumption that most of the radiation is collected at vertical incidence. This is not really true in the case of the x-dipole, for which reason there is an offset between the Q factors evaluated from $RF_i, i = 2, 3, 4$ and Q estimated from RF_1, which does not make any assumptions on the direction of radiation.

Using the method described in this section, we also calculated Q factors of the microcavity with defect produced by changing the refractive index of a single hole, and with fractional edge dislocations of order p applied along the x axis, as illustrated in Figure 1.8. The plane

S was positioned directly above the surface of the membrane in this case, and we estimated the radiated power from the expression 1.25 only. From Figure 1.16 it follows that the total Q factor saturates around 17000, when the number of layers around the defect increases in the structure with $p = 3$. This is very close to the maximum Q value estimated from the Fourier transforms of the field components, and plotted in Figure 1.25

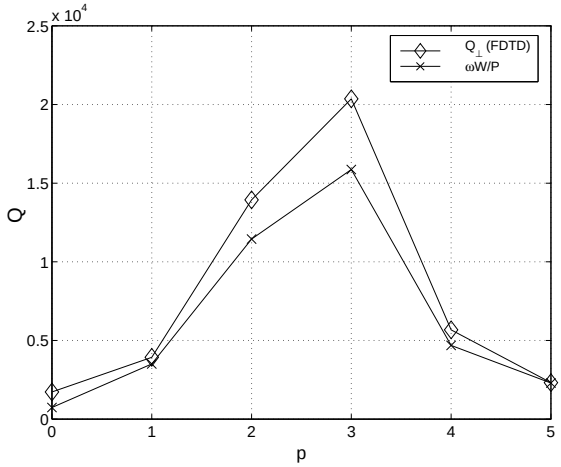

Figure 1.25: Q factor computed using the FDTD method, and from Fourier transforms of the parallel field components. The analyzed structure is shown in Figure 1.8.

1.9 Photonic crystal microcavities for cavity QED

In this section we consider the design of PC microcavities to achieve strong coupling between the cavity field and a single 'gas-phase' atom (that is, an atom located in free space rather than contained as an impurity in the dielectric slab). Our long-term goal is to investigate photonic bandgap structures for single-atom cavity quantum electrodynamics in the strong coupling regime.[30]

Let us consider a system consisting of a single atom positioned at location r_A within a cavity. The atomic and cavity resonance frequencies are labeled as ω_A and ω_C, respectively, but we assume that $\omega_A = \omega_C = \omega_0$. The Hamiltonian describing the interaction between

the atom and the field is given by the following expression:[30]

$$H_I = i\hbar\big(g(r_A)\hat{a}^\dagger\hat{\sigma}^- - g^*(r_A)\hat{a}\hat{\sigma}^+\big), \tag{1.33}$$

where $\hat{a}$ and $\hat{a}^\dagger$ are the annihilation and creation operators for the single mode and cavity under consideration, $\hat{\sigma}^\pm$ are the Pauli operators for raising and lowering of the atom, and $g(r_A)$ is the coupling rate between the atom and the cavity. The coupling rate $g(r_A)$ can be described as

$$g(r_A) = g_0\frac{\epsilon(r_A)|E(r_A)|}{max[\epsilon(r)|E(r)|]}, \tag{1.34}$$

where g_0 denotes the vacuum Rabi frequency

$$g_0 = \gamma_\perp\sqrt{\frac{V_0}{V_{mode}}} \tag{1.35}$$

$$V_0 = \frac{c\lambda^2}{8\pi\gamma_\perp} \tag{1.36}$$

In the previous expression, $\gamma_\perp$ represents the atomic dipole decay rate, i.e. the spontaneous emission rate in free space, λ is the mode wavelength and V_{mode} is the mode volume which is defined as

$$V_{mode} = \frac{\iiint \epsilon(r)|E|^2 dV}{max[\epsilon(r)|E|^2]} \tag{1.37}$$

The cavity field decay rate κ is proportional to the ratio of the angular frequency of the mode (ω_0) and the mode quality factor (Q):

$$\kappa = \frac{\omega_0}{4\pi Q} \tag{1.38}$$

The time decay of electromagnetic field energy stored in the cavity is given by the following expression:

$$W(t) = W(0)e^{-\frac{\omega_0 t}{Q}} = W(0)e^{-4\pi\kappa t} \tag{1.39}$$

In the *weak coupling regime*, the atom-field coupling rate $g(r_A)$ is much smaller than the loss rates of the system, such as the atomic dipole decay rate $\gamma_\perp$ and the cavity field decay rate κ. In this case, the atom undergoes the radiative energy decay at an enhanced rate, and this decay rate enhancement is given by the Purcell factor, which is proportional to the ratio of the cavity Q factor and the mode volume V_{mode}.[31] On the other hand, in the *strong coupling regime*, the atom-field coupling rate $g(r_A)$ is much larger than the loss rates of the system $\gamma_\perp$ and κ, i.e., $g(r_A) >> \kappa, \gamma_\perp$. This implies that the atom-cavity system has enough time to couple itself coherently, and the emission from the microcavity shows an oscillation instead of the usual exponential decay. In order to achieve strong coupling, we need to use an atom with a long lifetime (i.e., a small spontaneous emission rate $\gamma_\perp$), such as Cesium, with $\gamma_\perp = 2.6MHz$. The atom needs to be placed at the point r_A where its interaction with the cavity field is maximized (i.e., $\epsilon(r_A)|E(r_A)|$ is maximized). The cavity must have a small mode volume V_{mode} and a large Q factor, which leads to minimization of κ and maximization of g_0, and subsequent maximization of $g(r_A)$. The maximization of the microcavity mode quality factor (Q) and the minimization of the mode volume (V_{mode}) are the rules that are also followed when designing PC microcavities for semiconductor lasers. However, in a cavity for strong coupling, an atom must be trapped at the point where it interacts most strongly with the cavity field. Therefore, an additional design goal is imposed in this case: the cavity mode should have the E-field intensity as high as possible in the air region. When designing a laser cavity, the problem is the opposite: one tends to maximize the overlap between the gain region and the cavity field and, therefore, wants to have the strongest E-field in the semiconductor region.

Let us introduce the critical atom (N_0) and photon (m_0) numbers

$$N_0 = \frac{2\kappa\gamma_\perp}{g(r_A)^2} \tag{1.40}$$

$$m_0 = \left(\frac{\gamma_\perp}{2g(r_A)}\right)^2 \tag{1.41}$$

It follows that the strong coupling is possible if both N_0 and m_0 are smaller than 1.

Our goal is to build quantum networks by interconnecting quantum nodes, consisting of optical microcavities with atoms trapped within them at the points where they can couple very strongly to the cavity field.[32] Quantum nodes would be connected via optical waveg-

uides (e.g., photonic crystal waveguides), or optical fibers. The information (qubit) would be stored in the internal state of an atom trapped within a microcavity. In order to transmit the quantum information from the transmitting node T to the receiving node R, the following procedure would be applied: 1. the reading beam is applied to the transmitting node T and the atomic state (where the quantum information is stored) is mapped to the state of an optical photon via cavity QED; 2. the photon travels through the optical waveguide or fiber to the receiving node R; 3. in the receiving node R, the state of this photon is mapped to the state of an atom trapped in the receiving node, again through the cavity QED. In the transmitting node, the reading beam transfers the atom from the state $|1\rangle$ into an excited state $|e\rangle$, from which it subsequently decays into the ground state $|0\rangle$, with a generation of a single photon. Therefore, we have the following mapping in the node T:

$$|1\rangle_{atom}|0\rangle_{field} \longrightarrow |e\rangle_{atom}|0\rangle_{field} \longrightarrow |0\rangle_{atom}|1\rangle_{field} \tag{1.42}$$

In the case of strong coupling, when the loss rates of the system are much smaller than the coherent coupling rate $g(r_A)$, this mapping sequence is the dominant pathway. If, for example, the cavity Q drops, the probability of this sequence decreases. Therefore, a very strong coupling is necessary for efficient transfer of information from atomic to photonic state in quantum nodes.[32]

We plan to use photonic crystal microcavities with Cs atoms trapped in them as quantum nodes, and photonic crystal waveguides for communication between individual quantum nodes. In order to predict whether strong coupling can occur in the previously introduced photonic crystal microcavities, we must calculate the upper limits of critical atom and photon numbers N_0 and m_0 and compare them to 1. In other words, it is acceptable to overestimate calculated critical numbers. As the number of PC layers around the defect increases, the total quality factor Q approaches $Q_\perp$ and V_{mode} drops due to the better latteral confinement. Hence, we can calculate N_0 and m_0 by assuming $Q = Q_\perp$ and by using V_{mode} calculated for five PC layers around the defect. This can only cause a slight overestimation of N_0 and m_0.

The material and PC properties are chosen in such a way that cavities operate at $\lambda = 852nm$ (the wavelength corresponding to the atomic transition in ^{133}Cs). The material system of our choice is $Al_{0.3}Ga_{0.7}As$, which is transparent at this wavelength.

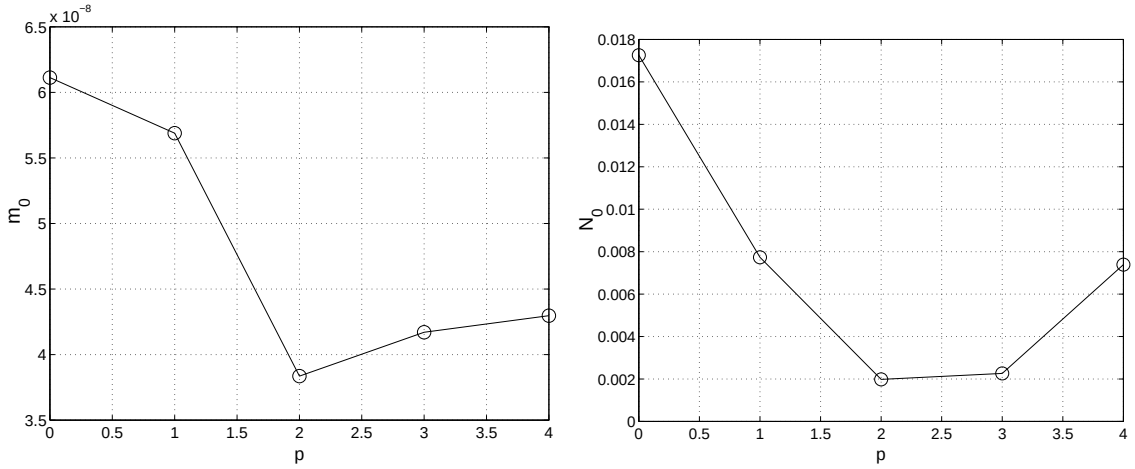

(a) (b)

Figure 1.26: Parameters of the x-dipole mode in the single defect structure ($r/a = 0.275$, $d/a = 0.75$, $r_{def}/a = 0.2$, $n = 3.4$ and $a = 20$) as a function of the elongation parameter p: (a) m_0; (b) N_0

1.9.1 Single defect with fractional edge dislocation

Let us now study the cavities introduced in the Section 1.6 as candidates for cavity QED. We concentrate on structures with the 1st set of PC parameters, i.e., $r/a = 0.275$, $d/a = 0.75$, $a = 20$ and the defect hole radius is $r_{def}/a = 0.2$. $Q_{||}$, $Q_{\perp}$ and a/λ of this structure, as a function of the elongation parameter p, are shown in Figure 1.13. We now calculate the critical atom (N_0) and photon (m_0) numbers as a function of the elongation parameter p for the same x-dipole mode, and the result is shown in Figure 1.26. From the electric field intensity pattern of the x-dipole mode shown in Figure 1.12, one can see that the electric field intensity is very strong within the defect hole. Therefore, an atom should be trapped there in order to interact most strongly with the cavity field. From the calculated critical atom and photon numbers, it then should be possible to achieve very strong coupling. At $\lambda = 852nm$, the parameters of such a cavity are $r = 70nm$, $d = 190nm$, $a = 250$ and $r_{def} = 50nm$. Due to extremely small mode volumes in these cavities, strong coupling is

possible even for moderate values of Q factors, as can be seen in Figures 1.13 and 1.26. Furthermore, m_0 is much smaller than N_0, which means that we can try to improve Q

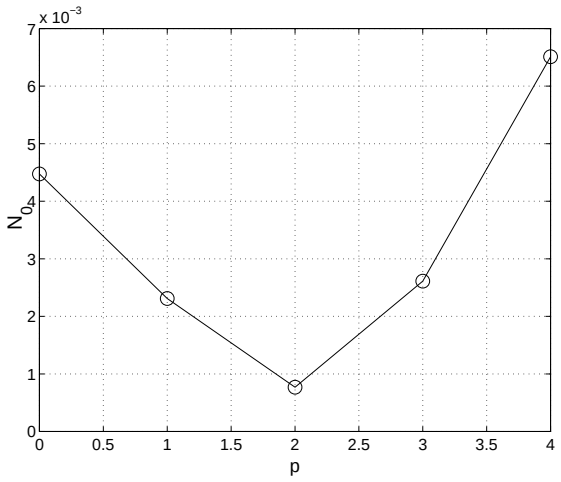

Figure 1.27: N_0 of the x-dipole mode in the structure where four holes in ΓJ direction are tuned, as a function of the elongation parameter p. The structure has the first set of PC parameters.

factors further, at the expense of increasing V_{mode}. Calculated lateral quality factors ($Q_{||}$) are much smaller than vertical ones ($Q_{\perp}$), since the cavities operate very close to the edge of the air band and only five PC layers surround the defect. However, by increasing the number of PC layers around the defect, we can increase $Q_{||}$ above $Q_{\perp}$ and make the total Q factor of the cavity determined only by $Q_{\perp}$.

1.9.2 Tuning holes around the defect

Q factors over 30000 were predicted for structures presented in Section 1.7, where in addition to single defect and fractional edge dislocation, the sizes and positions of 4 holes in ΓJ direction are tuned. The structure and the electric field profile are shown in Figure 1.18, and the dependence of the y-dipole mode frequency and Q on the elongation parameter p is shown in Figure 1.19. We can now calculate critical atom and photon numbers for an atom placed in the center of the central hole of the reduced radius, for the structure with the first set of PC parameters. The calculated m_0 is around $5 \cdot 10^{-8}$ for all p values, and

the calculated N_0 is presented in Figure 1.27. Again, these calculations predict that very strong coupling is achievable by this design.

1.9.3 Coupled dipole defect modes

The significance of surface effects that could perturb atomic radiative structure within the small defect hole is still unknown. For that reason, we will try to investigate ways of increasing the radius of the hole where the coupling between the atom and the cavity field should occur. Let us now analyze the cavity designs where a strong E-field intensity can be achieved in the center of an unperturbed hole. The idea is to use coupling between two dipole defect states.

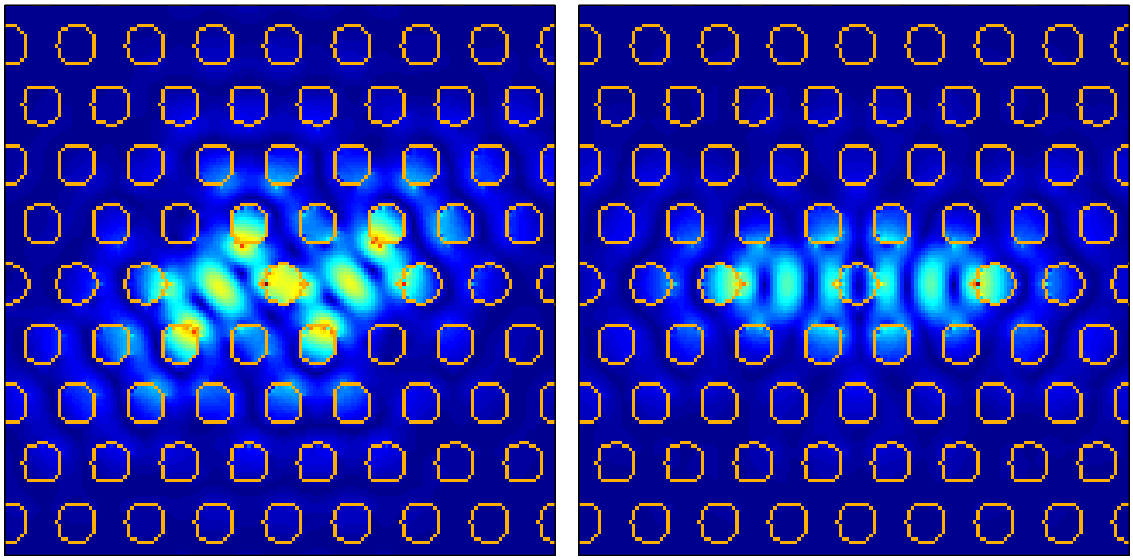

(a) (b)

Figure 1.28: Electric field intensity patterns of the coupled dipole modes: (a) constructively; (b) destructively coupled defect states.

Examples of resonant modes of microcavities formed by coupling two single defects are presented in Figure 1.28. Based on the resultant electric field intensity in the central, un-

perturbed hole, we call them *constructively* or *destructively* coupled defect states. These modes have different frequencies, as well as Q factors. We will analyze properties of constructively coupled states, since the central, unperturbed hole would be a good place for an atom.

We have analyzed a series of structures with different geometric parameters. The best results are obtained for two coupled y-dipoles in the structure with $r_{def}/a = 0.2$, $d/a = 0.75$, $r/a = 0.275$, $n = 3.4$ and $a = 20$. Holes in the ΓX direction, in columns containing defects, are elongated by two points in the x direction. The mode pattern of the constructively coupled y-dipoles is shown in Figure 1.29(a). Parameters of the shown mode are: $a/\lambda = 0.29$, $Q_{||} = 580$, $Q_{\perp} = 6100$, $V_{mode} = 0.93(\lambda/n)^3$, $m_0 = 1.5 \cdot 10^{-7}$ and $N_0 = 0.0135$. An atom can now be trapped in the central hole of unperturbed radius. For $\lambda = 852nm$, this radius is $r = 68nm$, which is a significant improvement over the previous design, for which an atom must be trapped within a $50nm$ radius hole. Again, strong coupling is achievable in this cavity.

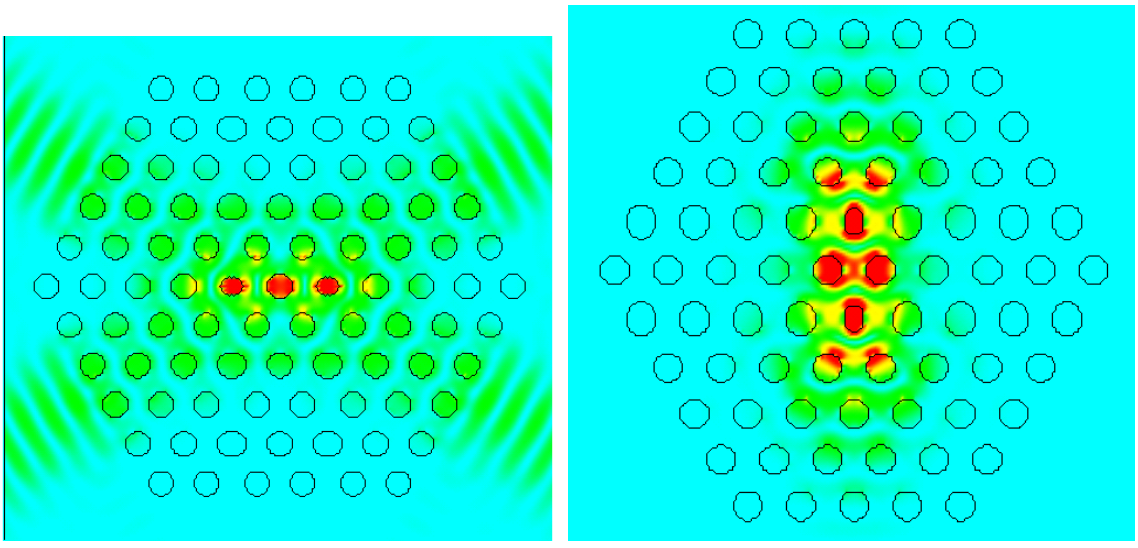

(a) (b)

Figure 1.29: Electric field intensity patterns of the constructively coupled dipole modes in the structure with the following parameters: $r_{def}/a = 0.2$, $d/a = 0.75$, $r/a = 0.275$, $n = 3.4$ and $a = 20$; (a) coupled y-dipoles; (b) coupled x-dipoles.

An alternative way of forming the coupled defects state is coupling two x-dipole modes, represented in Figure 1.29(b). We use the same PC parameters as previously: $r_{def}/a = 0.2$, $d/a = 0.75$, $r/a = 0.275$, $n = 3.4$ and $a = 20$, and holes in ΓJ direction, in rows containing defects, are elongated by two points in the y direction. The mode pattern of the constructively coupled x-dipoles is shown in Figure 1.29(b). Parameters of the mode are: $a/\lambda = 0.288$, $Q_{||} = 740$, $Q_{\perp} = 12120$, $V_{mode} = 0.69(\lambda/n)^3$, $m_0 = 1.4 \cdot 10^{-7}$ and $N_0 = 0.0063$. Strong coupling is achievable for an atom trapped in any of the two central holes of unperturbed radius (positioned between the defects). For $\lambda = 852nm$, this radius is again $r = 68nm$.

1.10 Optimization of Q factors of acceptor modes

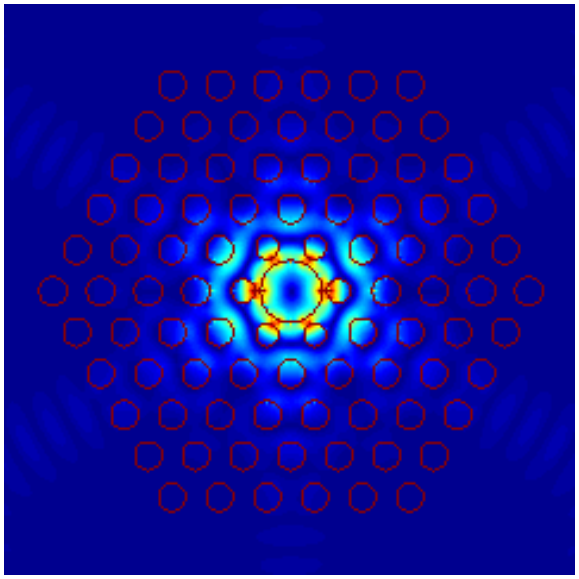

Figure 1.30: Fine tuning of six holes around the central defect helps in the optimization of the Q factors of the acceptor state (monopole), whose electric field intensity is shown in this figure. For example, by reducing the radii of these six holes to $r_1/a = 0.25$ (from $r/a = 0.3$ in the unperturbed photonic crystal) and moving them simultaneously in six ΓJ directions to preserve the distance between them and their next nearest neighbors, we can improve the Q factor of the monopole mode from 170 to almost 1000 for the central hole radius $r_{def}/a = 0.65$, and improve the Q factor of the monopole mode from 2500 to around 10000 when the central hole radius is equal to $r_{def}/a = 0.5$.

In the subsection 1.4.2, we have shown that the Q factor of the acceptor mode (monopole), excited in the microcavity formed by increasing the radius of a single PC hole, can reach the value of 2500 at maximum. However, Q factors of acceptor states are also very sensitive to fine tuning of the geometry around a single defect. For example, the tuning of the six nearest neighbor holes can help in improving the Q factor significantly. In this process, we decrease the radii of these six holes to r_1 (from the original r in the unperturbed PC), and move them simultaneously across the distance equal to $r - r_1$ in six ΓJ directions, in order to preserve the distances between them and their next-nearest neighbors in the same directions. This is illustrated in Figure 1.30. For example, let us consider microcavities formed in the PC with the same parameters as in the subsection 1.4.2: $r/a = 0.3$, $d/a = 0.65$ and $n = 3.4$. When the central hole radius is increased to $r_{def}/a = 0.65$, the monopole mode with $Q \approxeq 170$ can be excited, as shown in Figure 1.9. However, if in addition to forming this single defect we reduce the radii of the six nearest neighbor holes to $r_1/a = 0.25$ and reposition them in the ΓJ directions, we can improve the quality factor of the same monopole mode to a value of almost 1000. Similarly, for the central defect with the radius $r_{def}/a = 0.5$, we were previously able to reach the Q factor of almost 2500 for the analyzed acceptor state. By tuning six nearest neighbor holes in this structure to $r_1/a = 0.25$, we can improve this quality factor to a value of around 10000.

1.11 Influence of the low refractive index cladding on parameters of planar PC structures

The principal geometries of planar photonic crystal research can be divided into two categories: structures based on optically thin semiconductor membranes (free-standing membranes, with air cladding),[7–9, 11, 20] and structures fabricated in the slab waveguide consisting of a semiconductor core and cladding layers of lower refractive index.[12] The difference lies in the design of the waveguide used for the vertical confinement. Our group at Caltech has been studying free-standing membranes for the past few years. In this section, the influence of symmetric low-refractive index cladding layers on the properties of the dipole defect modes is tested.

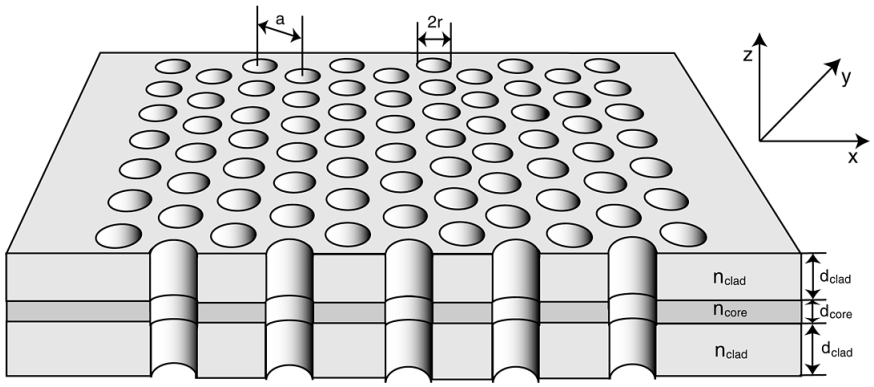

Figure 1.31: Slab waveguide patterned with a triangular array of air holes.

The analyzed structure is shown in Figure 1.31. The refractive index of the core is $n_{core} = 3.4$, and the refractive index of the cladding can have one of the following values: (1) $n_{clad} = 1$, corresponding to air (in the case of the free standing membrane); (2) $n_{clad} = 1.5$, corresponding to oxide (e.g., AlO_x cladding on $GaAs$ core, or SiO_2 cladding on Si core; (3) $n_{clad} = 2.9$, corresponding to $Al_xGa_{1-x}As$ cladding on $GaAs$ core, with $x \approxeq 20\%$. The same two types of previously analyzed PC arrays are again treated in this section, with addition of claddings: (1) $r/a = 0.275$, $d_{core}/a = 0.75$ and $d_{clad}/d_{core} = 2.2$; (2) $r/a = 0.3$, $d_{core}/a = 0.65$ and $d_{clad}/d_{core} = 2.56$. The chosen values of d_{clad} correspond to $a/0.6$, which is approximately $\lambda/2$, i.e., one half of the dipole mode wavelength, measured in air. Band diagrams for the TE-like modes in the PC structures with the previously introduced sets of parameters and claddings are shown in Figures 1.32 and 1.33. Band diagrams of these structures without claddings are shown in Figure 1.2. Several observations are worth noting at this point. Bands from the dispersion diagram of the structure without cladding layers remain present in the dispersion diagrams of structures with cladding layers. However, there is an offset in their positions, due to the presence of more high-refractive index material. Moreover, additional modes also occur in the presence of cladding layers. These new modes are positioned above the light line in the cladding, and below the light line in air, which implies that they can propagate in the cladding, without leaking into air. These additional modes exist at frequencies within the original bandgap and can represent a new lateral loss mechanism. We will show the result of such losses on the electric field intensity patterns of cavity modes later in this section.

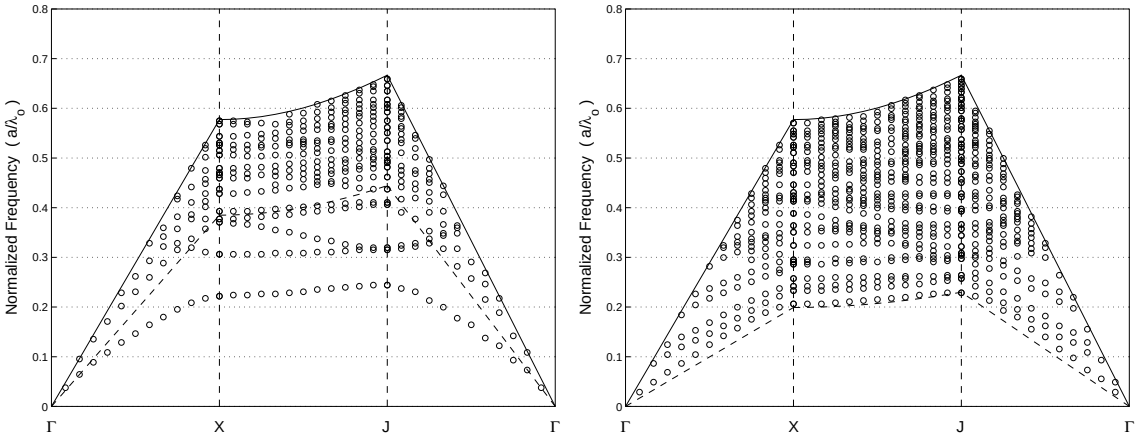

(a) (b)

Figure 1.32: Band diagrams for TE-like modes in the structure with $n_{core} = 3.4$, $d_{core}/a = 0.75$, $r/a = 0.275$: (a) $d_{clad} = 2.2d_{core}$ and $n_{clad} = 1.5$; (b) $d_{clad} = 2.2d_{core}$ and $n_{clad} = 2.9$. Band diagrams were calculated using the 3D FDTD method. The full line is the light line in air, and the dashed line is the light line in the appropriate cladding.

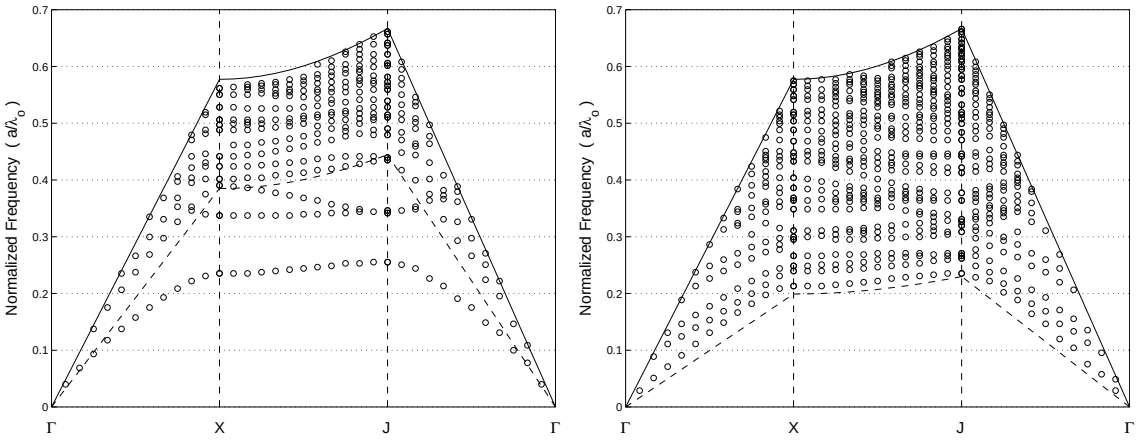

(a) (b)

Figure 1.33: Band diagrams for TE-like modes in the structure with $n_{core} = 3.4$, $d_{core}/a = 0.65$, $r/a = 0.3$: (a) $d_{clad} = 2.56d_{core}$ and $n_{clad} = 1.5$; (c) $d_{clad} = 2.56d_{core}$ and $n_{clad} = 2.9$. Band diagrams were calculated using the 3D FDTD method. The full line is the light line in air, and the dashed line is the light line in the appropriate cladding.

An alternative way of viewing this problem is that the band diagram of the entire structure is obtained by combining the dispersion diagrams of the core and the cladding. Certainly, the overall dispersion diagram is not a simple superposition of the two, but can be viewed that way in the first approximation. In order to achieve a bandgap in the resulting structure, we would have to design the two components in such a way that their bandgaps overlap. Parameters of the x-dipole mode, excited in the structure where the radius of a single PC hole is reduced, are shown in Figure 1.34. Frequency and Q factor of the mode are plotted as a function of the radius of the defect hole (r_{def}) and the type of the supporting waveguide. The boundary for separation of $Q_{\perp}$ from $Q_{||}$ is positioned approximately at 0.7λ from the center of the slab, implying that losses in the cladding layers are included in $Q_{||}$.

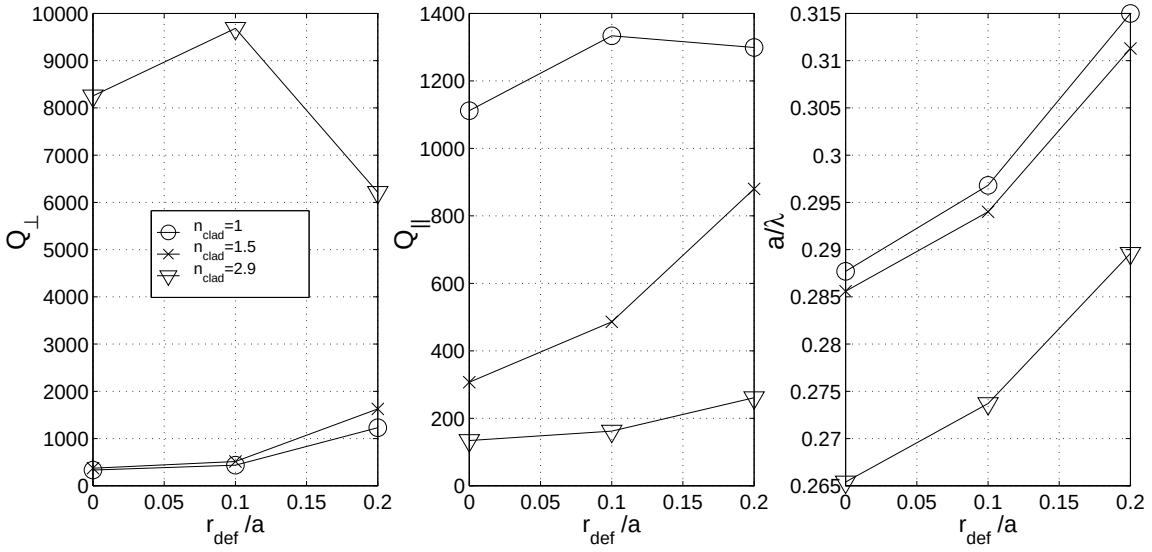

Figure 1.34: Parameters of the donor mode (x-dipole) in the single defect structure ($r/a = 0.3$, $d/a = 0.65$) as a function of the defect hole radius r_{def}, and the type of the supporting waveguide.

The first observation is that the presence of cladding layers reduces vertical losses and increases lateral losses. The larger the refractive index of a cladding, the larger is the drop in $Q_{||}$ and increase in $Q_{\perp}$. However, before jumping to any conclusions, it is important to thoroughly understand what limits the total Q factor in each case. Starting from the discussion of band diagrams presented earlier, the drop in $Q_{||}$ in the presence of cladding layers comes from the fact that the number of additional modes guided in these layers

increases when n_{clad} increases. These additional modes represent a new mechanism of lateral loss, and a serious problem arises when the DBR confinement of the defect mode is lost, which happens for both $n_{clad} = 2.9$ and $n_{clad} = 1.5$ in our calculation. At that point, there is nothing we can do to improve $Q_{||}$ and the total Q factor is limited by $Q_{||}$. Therefore, we cannot take the advantage of the improved $Q_{\perp}$, since much smaller $Q_{||}$ limits Q. It is also important to note that the frequency of the defect mode drops when n_{clad} increases. This is expected, since the mode overlaps with more dielectric material of refractive index larger than 1.

Table 1.2: Q factors of the x-dipole mode excited in microcavities formed by omitting a single PC hole, in the presence of symmetric cladding.

n_{clad}	No of PC layers	a/λ	$Q_{\|\|}$	$Q_{\perp}$	Q
1	5	0.2877	1112	334	257
1	7	0.288	1507	336	274
1.5	5	0.2856	307	371	168
1.5	7	0.2855	251	485	165
2.9	5	0.2654	134	8254	132
2.9	7	0.2667	130	10130	128

To prove that the loss of lateral confinement really happens in this case, we analyze how $Q_{||}$ and $Q_{\perp}$ of the x-dipole defect mode change as a function of the number of PC layers. We perform this analysis of loss for cavities in photonic crystal made in waveguide material where the refractive index of the cladding was set to 1, 1.5 and 2.9. Results are shown in Table 1.2. The analyzed mode is excited in the cavity formed by omitting a single hole (i.e., $r_{def} = 0$). The increase in the number of PC layers around the defect results in an increase in $Q_{||}$ only for the structure with air cladding (i.e., $n_{clad} = 1$). Therefore, this is the only structure having a complete lateral confinement. On the other hand, $Q_{||}$, $Q_{\perp}$ and the total Q factor for waveguide structures with low refractive index cladding remain approximately constant when the number of PC layers increases. The electric field intensity patterns of the x-dipole mode, on the vertical slice through the center of the defect (x-z plane) are shown in Figure 1.35. It can be seen in these plots that the defect mode couples to modes guided within the cladding layers, thereby resulting in a large lateral loss. The

lateral PC confinement is lost in this case, although from the radiation patterns one can also see that the vertical loss is much smaller in the presence of $n_{clad} = 2.9$ cladding, as has been predicted in the past.

We also analyze the influence of waveguide cladding layers on properties of the y-dipole defect mode excited in the structure presented in Section 1.7. The result is shown in Figure 1.36. There is again a dramatic drop in $Q_{||}$ in the presence of claddings, but the increase in $Q_{\perp}$ is not significant in this case.

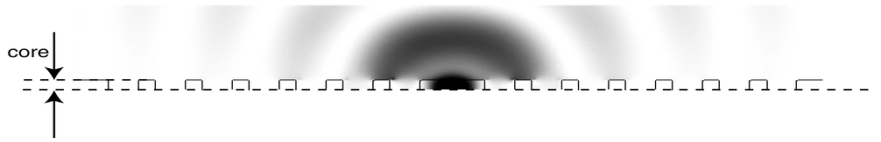

(a)

(b)

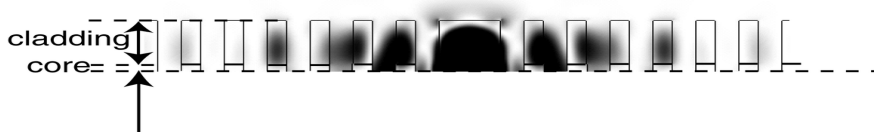

(c)

Figure 1.35: The electric field intensity patterns of the donor mode (x-dipole) in a single defect structure ($r/a = 0.3$, $d/a = 0.65$, $r_{def} = 0$), as a function of the type of the supporting waveguide: (a) no cladding ($n_{clad} = 1$); (b) $n_{clad} = 1.5$; (c) $n_{clad} = 2.9$. The field intensity is shown in the $x - z$ plane (vertical plane) through the center of the defect, and for $z > 0$.

Therefore, although the low refractive index claddings can help in reduction of vertical loss, this improvement is not very significant for the most sophisticated cavity designs. Unfortunately, additional lateral losses are predicted in the presence of cladding layers, due to modes guided within these cladding regions. In order to preserve the lateral confinement in the presence of claddings, and to gain the advantage from the reduction in vertical loss, cavities have to be designed in such a way that defect modes have symmetry different from modes guided in the claddings, which would prevent them from coupling to each other. Certainly, the parameter space of the clad waveguide and photonic crystal will have to be explored more thoroughly in order to minimize the number of these additional modes guided in cladding layers, and therefore minimize the additional lateral loss resulting from these modes. Since both the number of the additional modes guided in the cladding layers and the reduction in vertical loss are directly proportional to n_{clad}, the complexity of the problem of preserving the lateral confinement is directly proportional to the improvement in Q factor. Considering that the improvement in Q factor from reduction of vertical scattering in clad waveguide geometries is not very significant for our most sophisticated designs, we will continue to pursue our work on free standing membranes.

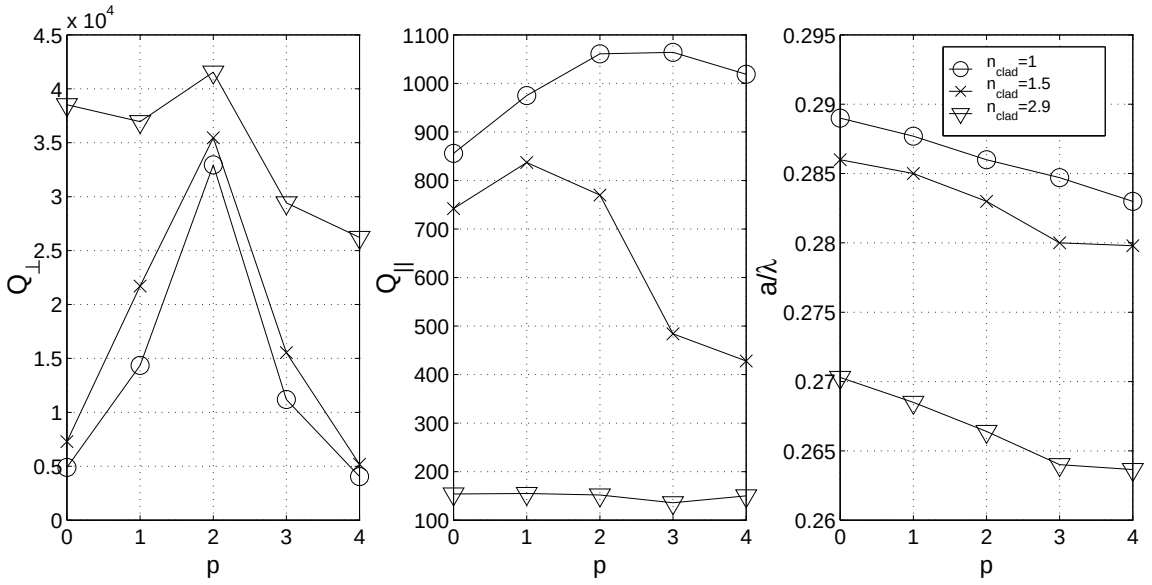

Figure 1.36: Parameters of the donor mode (y-dipole) in the defect structure, where four holes are tuned in the ΓJ directions ($r/a = 0.275$, $d/a = 0.75$, $r_1/a = 0.225$, $r_{def}/a = 0.2$), as a function of the elongation parameter p, and the type of the supporting waveguide.

1.12 Spontaneous emission control in optical microcavities based on planar photonic crystals

In 1946 Purcell predicted that the radiation rate of an atom could be modified by placing it in a wavelength-sized cavity.[33] The spontaneous emission rate was often considered an inherent property of atom, but Purcell described that it could actually be changed by modifying the atom's environment. However, it took almost 50 years after this groundbreaking discovery to be able to build cavities whose size is of the order of optical wavelength, and use Purcell's effect to modify light emission within a semiconductor.[34–37]

Two important parameters are used to describe the spontaneous emission properties of a system: Purcell factor and β factor. Purcell factor is defined as the ratio of the spontaneous emission lifetimes without and with the cavity. Since the topic of our interest is the spontaneous emission within a semiconductor, we define the Purcell factor as the ratio of the spontaneous emission lifetimes of an emitter in the bulk semiconductor, and in the semiconductor microcavity. Therefore, this factor is proportional to the spontaneous emission rate enhancement in the presence of a microcavity. On the other hand, the spontaneous emission coupling factor (β factor) of a given mode is defined as the ratio of the spontaneous emission rate into that mode and the spontaneous emission rate into all modes.[38] The importance of this parameter lies in the fact that the laser threshold reduces as β approaches 1.[38,39] If we can simultaneously enhance the spontaneous emission within the semiconductor and achieve β close to 1, we can build a light source with high quantum efficiency and broad modulation width, based on the single-mode spontaneous emission.[37]

The great experimental work on this topic has been done by employing post mirocavities,[37] or microdisks.[35,36] Over the past few years much scientific attention has been focused on the use of photonic crystals for spontaneous emission control.[2] However, due to the complex geometry of the proposed microcavities, it was not possible to perform the detailed analysis of their Purcell and β factor. There are many analyses (both classical and quantum mechanical) of these parameters in the literature, but they consider only simple geometries and often use many approximations. These include the spontaneous emission factor of the injection laser,[40] the VCSEL of square cross-section,[41,42] the microdisk[43] and the ring laser.[44] In 1999, in collaboration with Prof. Yariv's group at Caltech, we proposed methods

for the calculation of these important parameters, which are flexible enough to incorporate highly complex geometries, including those of photonic crystals.[45–47] Methods are based on the classical model for atomic transitions and employ the FDTD method. We have theoretically identified that optical microcavities based on planar PCs can be used to achieve spontaneous emission control and our results are presented in this section. Unfortunately, these properties of planar PC structures have not been demonstrated yet experimentally.

1.12.1 Description of the proposed method for calculation of the β factor

Our starting point is the classical model for the β factor calculation.[40–42] Atomic transitions are modelled as classical oscillating electric dipoles with resonant frequencies equal to the atomic transition frequency ω_p. Different dephasing mechanisms are taken into account through the dipole lifetime τ_d, which corresponds to the homogeneous broadening of the spontaneous emission spectrum.[48]

No dipole sources

Consider first the electromagnetic field of the system when dipoles are not present. We solve the problem in a large box, which we call the computational domain and denote as V_{CD}. Appropriate boundary conditions, which depend on the physical situation of interest, have to be applied to the surface enclosing V_{CD}. We neglect the absorption losses (i.e., we assume that the conductivity of a medium is equal to zero). At any point inside the box, the set of Maxwell's curl equations has to be satisfied:

$$\vec{\nabla} \times \vec{H} = \epsilon(\vec{r}) \frac{\partial \vec{E}}{\partial t} \tag{1.43}$$

$$\vec{\nabla} \times \vec{E} = -\mu_0 \frac{\partial \vec{H}}{\partial t} \tag{1.44}$$

Let $\{\vec{E}_m(\vec{r})\}$ be the complete set of transverse orthonormal modes of the lossless cavity.[49–51] The orthonormality condition (with a position dependent dielectric constant $\epsilon(\vec{r})$) is defined

as follows:[50]

$$\iiint_{V_{CD}} \epsilon(\vec{r})\vec{E}_m(\vec{r}) \cdot \vec{E}_n^*(\vec{r})d^3\vec{r} = \delta_{mn}, \tag{1.45}$$

where δ_{mn} is the Kronecker's delta. The transversality condition is given by the following:[50]

$$\vec{\nabla} \cdot \left(\epsilon(\vec{r})\vec{E}_m(\vec{r})\right) = 0 \tag{1.46}$$

Each of these modes satisfies the following wave equation:

$$\vec{\nabla} \times \left[\vec{\nabla} \times \vec{E}_m(\vec{r})\right] = \mu_0\epsilon(\vec{r})\omega_m^2\vec{E}_m(\vec{r}), \tag{1.47}$$

where ω_m is the frequency of a mode. In the mode expansion method we express the total electric field of the cavity using the modes from the set $\{\vec{E}_m(\vec{r})\}$:[49,50]

$$\vec{E}(\vec{r},t) = \sum_m \vec{E}_m(\vec{r})f_m(t) = \sum_m \vec{\eta}_m(\vec{r},t) \tag{1.48}$$

Each term $\vec{\eta}_m(\vec{r},t)$ in the previous expansion satisfies the following wave equation:

$$\vec{\nabla} \times \vec{\nabla} \times \vec{\eta}_m = -2\kappa_m\mu_0\epsilon(\vec{r})\frac{\partial\vec{\eta}_m}{\partial t} - \mu_0\epsilon(\vec{r})\frac{\partial^2\vec{\eta}_m}{\partial t^2}, \tag{1.49}$$

where κ_m is the field decay rate for the m-th mode, which accounts for the radiation outside the box. For some optical mode described by frequency ω_m and the quality factor[52] Q_m, the field decay rate is given by

$$\kappa_m = \frac{\omega_m}{2Q_m}. \tag{1.50}$$

From the equations (1.45),(1.47) and (1.49), it follows that

$$\ddot{f}_m(t) + 2\kappa_m\dot{f}_m(t) + \omega_m^2 f_m(t) = 0 \tag{1.51}$$

with the solution:

$$f_m(t) = F_m e^{i\omega'_m t} e^{-\frac{\omega_m t}{2Q_m}}, \tag{1.52}$$

where $\omega'_m = \omega_m(1 - \frac{1}{4Q_m^2})^{\frac{1}{2}}$. For the cavity modes of interest Q_m is large enough so that we can assume $\omega'_m \approxeq \omega_m$.

We can discretize space and time in equations (1.43) and (1.44) and use the FDTD method to calculate the electromagnetic field of the system. We apply Mur's absorbing boundary condition[53] (ABC) to the boundaries of the computational domain which allows the radiation to escape outside, without reflecting back into V_{CD}.

The first step in our calculation involves isolating (filtering) the mode of interest in the optical cavity. The filtered mode is then normalized in the following way:

$$\iiint_{V_{CD}} \epsilon(\vec{r}) |\vec{E}_0(\vec{r})|^2 d^3\vec{r} = 1 \tag{1.53}$$

Once we have solved for the field pattern of the mode of interest, we then proceed to calculate the electric and magnetic fields of the system excited by oscillating dipoles.

Dipole sources

Let us assume we have N dipoles, all at the same time in the microcavity, that are randomly positioned and randomly polarized in the active region ($\vec{r}_p^{(i)}$ and $\hat{P}_0^{(i)}$ are the position and the polarization of the i-th dipole, respectively). We first consider dipoles which have a single oscillation frequency ω_p and lifetime τ_d, but random phases which are uniformly distributed in the range $[0, 2\pi)$ (ϕ_i is the initial phase of the i-th dipole).

The Maxwell curl equations now have the following form:

$$\vec{\nabla} \times \vec{H} = \epsilon(\vec{r}) \frac{\partial \vec{E}}{\partial t} + \frac{\partial \vec{P}}{\partial t} \tag{1.54}$$

$$\vec{\nabla} \times \vec{E} = -\mu_0 \frac{\partial \vec{H}}{\partial t} \tag{1.55}$$

where $\vec{P}(\vec{r},t)$ is given by the following expression:

$$\vec{P}(\vec{r},t)=\sum_{i=1}^{N}\hat{P}_0^{(i)}e^{j(\omega_p t+\phi_i)}e^{-\frac{t}{\tau_d}}\delta(\vec{r}-\vec{r}_p^{(i)}) \tag{1.56}$$

We discretize the equations (1.54)-(1.56) with the initial conditions $\vec{E}(\vec{r},t=0^-)=0$ and $\vec{H}(\vec{r},t=0^-)=0$. Mur's ABC is again applied to the boundaries of the computational domain V_{CD}. The electric field in the cavity can be separated into transverse and longitudinal parts:[50]

$$\vec{E}(\vec{r},t)=\vec{E}_T(\vec{r},t)+\vec{E}_L(\vec{r},t), \tag{1.57}$$

where

$$\vec{\nabla}\cdot\left(\epsilon(\vec{r})\vec{E}_T(\vec{r},t)\right)=0 \tag{1.58}$$

Using FDTD method we evolve real parts of the fields:

$$\vec{E}^{\Re}(\vec{r},t)=\Re\left[\vec{E}(\vec{r},t)\right] \tag{1.59}$$

$$\vec{H}^{\Re}(\vec{r},t)=\Re\left[\vec{H}(\vec{r},t)\right] \tag{1.60}$$

Let us choose a volume V (with outer surface S) to be a subset of V_{CD} containing all the dipoles and enclosing the microcavity. At time t, we calculate the energy radiated into all modes, $W_{\sum}(t)$, as

$$W_{\sum}(t)=W_{E,V}(t)+W_{H,V}(t)+\int_0^t P_{rad}(\tau)d\tau \tag{1.61}$$

$$W_{E,V}(t)=\iiint_V\frac{\epsilon(\vec{r})}{2}|\vec{E}_T^{\Re}(\vec{r},t)|^2d^3\vec{r} \tag{1.62}$$

$$W_{H,V}(t)=\iiint_V\frac{\mu_0}{2}|\vec{H}^{\Re}(\vec{r},t)|^2d^3\vec{r} \tag{1.63}$$

$$P_{rad}(\tau)=\iint_S(\vec{E}^{\Re}(\vec{r},\tau)\times\vec{H}^{\Re}(\vec{r},\tau))d\vec{S} \tag{1.64}$$

$P_{rad}(\tau)$ represents the power radiated out of the cavity, and $\vec{E}_T^{\Re}(\vec{r},t)$ is defined as

$$\vec{E}_T^{\Re}(\vec{r},t) = \Re\left[\vec{E}_T(\vec{r},t)\right] \tag{1.65}$$

The total energy radiated into all modes is

$$W_{\sum\infty} = \lim_{t\to\infty} W_{\sum}(t) \tag{1.66}$$

If we evolve the fields for a long enough time t' ($t' \gg \tau_d$), such that the energy of the electromagnetic field which remains within V at $t = t'$ is negligible, we can approximate $W_{\sum\infty}$ as

$$W_{\sum\infty} = W_{\sum}(t') \approxeq \int_0^{t'} P_{rad}(\tau)d\tau \tag{1.67}$$

The transverse electric field (which is the radiation field[49,50]) can be expressed as the superposition of the complete set of orthonormal modes of the closed cavity $\vec{E}_m(\vec{r})$, introduced previously:

$$\vec{E}_T(\vec{r},t) = \sum_n \vec{E}_n(\vec{r})g_n(t) \tag{1.68}$$

$\vec{E}_T(\vec{r},t)$ satisfies the following wave equation:

$$\begin{aligned}\vec{\nabla}\times\left[\vec{\nabla}\times\vec{E}_T\right] = &-2\mu_0\epsilon(\vec{r})\sum_m \kappa_m\vec{E}_m(\vec{r})\dot{g}_m(t)\\ &-\mu_0\epsilon(\vec{r})\frac{\partial^2\vec{E}_T}{\partial t^2} - \mu_0\frac{\partial^2\vec{P}_T}{\partial t^2},\end{aligned} \tag{1.69}$$

where $\vec{P}_T$ denotes the tranverse component of $\vec{P}$. From the equations (1.45), (1.47), (1.68) and (1.69) we obtain the differential equation for $g_m(t)$, corresponding to a localized mode

labeled by index m:

$$\begin{aligned}\ddot{g}_m(t) + \frac{\omega_m}{Q_m}\dot{g}_m(t) + \omega_m^2 g_m(t) = \\ = -\iiint\limits_{V_{CD}} d^3\vec{r}\vec{E}_m^*(\vec{r}) \cdot \frac{\partial^2 \vec{P}_T(\vec{r},t)}{\partial t^2} \\ = -\iiint\limits_{V_{CD}} d^3\vec{r}\vec{E}_m^*(\vec{r}) \cdot \frac{\partial^2 \vec{P}(\vec{r},t)}{\partial t^2}\end{aligned} \tag{1.70}$$

The transformation of the integral in the previous equation was proven previously in reference 50. The right hand-side in the equation (1.70) can be written in the following way:

$$\begin{aligned}G_m(t) = -\iiint\limits_{V_{CD}} d^3\vec{r}\vec{E}_m^*(\vec{r}) \cdot \frac{\partial^2 \vec{P}(\vec{r},t)}{\partial t^2} = \\ = G^{(m)} e^{j\omega_p t} e^{-\frac{t}{\tau_d}},\end{aligned} \tag{1.71}$$

where

$$G^{(m)} = \left[-\omega_p^2 + \frac{1}{\tau_d^2} - j\frac{2\omega_p}{\tau_d}\right] \sum_{i=1}^{N} \hat{P}_0^{(i)} \cdot \vec{E}_m^*(\vec{r}_p^{(i)}) e^{j\phi_i} \tag{1.72}$$

Under the condition that the transverse electric field is zero at $t = 0$ ($g_m(0) = 0$ for all m), we solve the equation (1.70) for $g_m(t)$:

$$g_m(t) = B_m\left(e^{j\omega_p t}e^{-\frac{t}{\tau_d}} - e^{j\omega_m t}e^{-\frac{\omega_m t}{2Q_m}}\right) \tag{1.73}$$

$$B_m = \frac{G^{(m)}}{\omega_m^2 - \omega_p^2 + \frac{1}{\tau_d^2} - \frac{\omega_m}{\tau_d Q_m} - j\omega_p(\frac{2}{\tau_d} - \frac{\omega_m}{Q_m})} \tag{1.74}$$

Let us label the fundamental mode by index 0. Then the energy radiated into the fundamental mode at time $t \to \infty$ can be calculated as follows:[41]

$$W_{0\infty} = \frac{1}{2}\int_0^\infty 2\kappa_0 dt \iiint\limits_{V_{CD}} \epsilon(\vec{r})\vec{E}_0(\vec{r},t) \cdot \vec{E}_0^*(\vec{r},t) d^3\vec{r}, \tag{1.75}$$

where

$$\vec{E}_0(\vec{r},t) = \vec{E}_0(\vec{r})g_0(t) \tag{1.76}$$

It follows that

$$W_{0\infty} = \kappa_0|B_0|^2\left[\frac{\tau_d}{2} + \frac{Q_0}{\omega_0} - \frac{2\left(\frac{1}{\tau_d}+\frac{\omega_0}{2Q_0}\right)}{(\omega_p-\omega_0)^2+(\frac{1}{\tau_d}+\frac{\omega_0}{2Q_0})^2}\right] \tag{1.77}$$

It should be noted that the choice of $\dot{g}_0(0)$ doesn't influence the value of $W_{0\infty}$. An alternative approach (which leads to the same result) is to calculate $W_{0\infty}$ in the following way:

$$W_{0\infty} = \int_0^\infty dt \frac{1}{2}\Re\left[\iiint_{V_{CD}} \vec{E}_0^*(\vec{r},t)\cdot\frac{\partial\vec{P}(\vec{r},t)}{\partial t}d^3\vec{r}\right] \tag{1.78}$$

The β factor of the fundamental mode is equal to the ratio of the total energy radiated into that mode and the total energy radiated into all modes.[40–42]

We include the inhomogenous broadening by using an approximate transition spectrum which has a Lorentzian shape, with the central frequency ω_s and FWHM equal to $\Delta\omega_s$:

$$F(w_p) = \frac{\frac{\Delta\omega_s}{2\pi}}{(\omega_p-\omega_s)^2+(\frac{\Delta\omega_s}{2})^2} \tag{1.79}$$

$$\int_{-\infty}^{+\infty} F(\omega_p)\,d\omega_p = 1 \tag{1.80}$$

$F(w_p)$ represents the density of dipoles (electronic states) at the frequency w_p. We average the result over different dipole resonant frequencies:

$$\beta = \frac{\sum\limits_{\omega_p} F(\omega_p)W_{0\infty}(\omega_p)}{\sum\limits_{\omega_p} F(\omega_p)W_{\sum\infty}(\omega_p)} \tag{1.81}$$

The value of the β factor when only homogeneous broadening is taken into account and dipoles have the frequency ω_p is denoted by β_H and given by

$$\beta_H = \frac{W_{0\infty}(\omega_p)}{W_{\sum\infty}(\omega_p)}, \tag{1.82}$$

1.12.2 Calculation of the spontaneous emission rate

For the detailed analysis of the method, the reader is referred to the Reference 47. The method is based on the fact that the spontaneous emission rate is proportional to the classical dipole radiation power:

$$\frac{\tau_{spont}^{bulk}}{\tau_{spont}^{cavity}} = \frac{P_{classical}^{cavity}}{P_{classical}^{bulk}}, \tag{1.83}$$

where τ_{spont} is the spontaneous emission lifetime. Therefore, the Purcell factor can be calculated as the ratio of the powers radiated by the classical dipole placed in the cavity, and in the bulk material. The FDTD method allows us to calculate these powers for any type of cavity geometry.

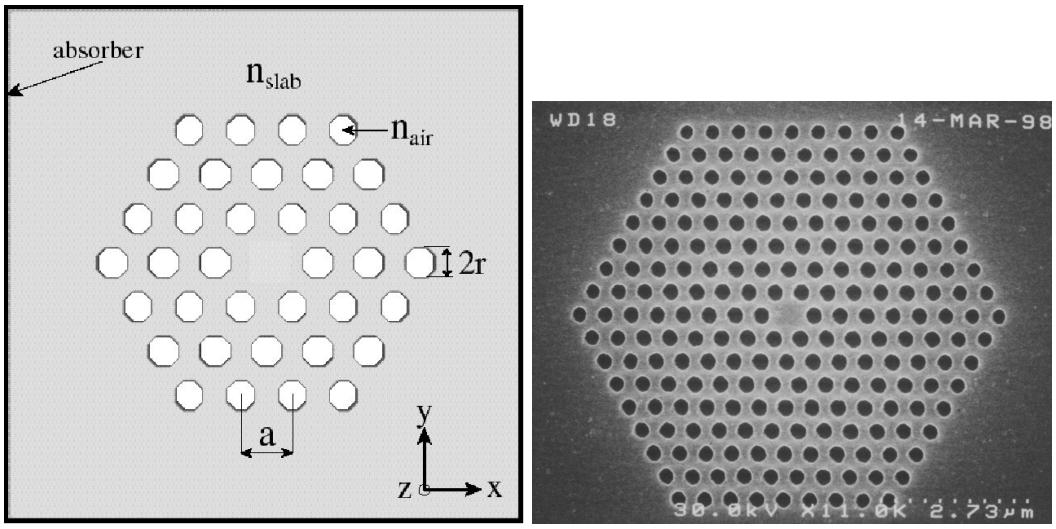

(a) (b)

Figure 1.37: (a) Schematic of a 2D slice through the middle of the patterned high index slab. A defect in the hexagonal lattice of air holes is formed by omitting the central hole of the array; (b) Top view of a microfabricated 2D hexagonal array of holes with a single central hole missing. The inter-hole spacing is a=500nm, and the radius of the holes is approximately 150nm.

1.12.3 β factor of the microcavity based on 2D PBG in an optically thin dielectric slab

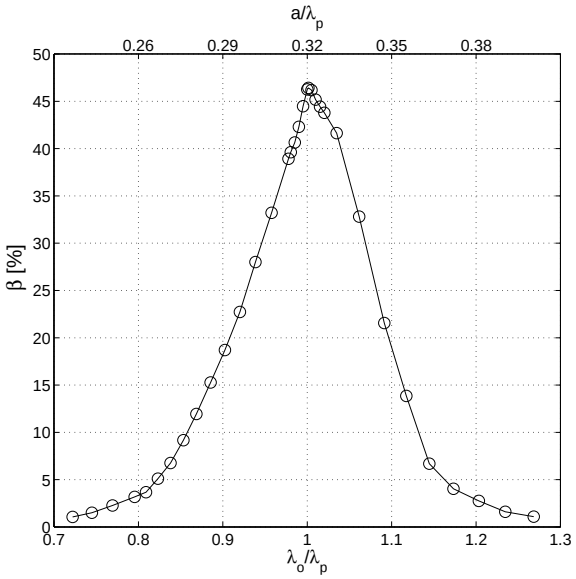

Figure 1.38: β_H dependence on the wavelength of the dipole excitation λ_p for the microcavity based on 2D PBG. λ_0 is the wavelength of the dipole mode. $\tau_d = 0.1ps$.

The microcavity that we analyze is an optically thin dielectric slab patterned with a 2D array of holes, as shown in Figure 1.37. A defect is made by omitting a central hole of the array. The parameters of the analyzed structure are $\frac{r}{a} = 0.3$, $\frac{d}{a} = 0.4$, $n_{slab} = 3.4$ and 3 periods of PC holes around the defect. In Figure 1.37 we show the top view of a microfabricated defect cavity in InGaAsP, designed for $1.55\mu m$ emission.[54] We consider the x-dipole mode to be the fundamental mode. Its normalized frequency is $\frac{a}{\lambda_0} = 0.32$ and quality factor is $Q_0 = 129$. If we assume that in reality $\lambda_0 = 1.55\mu m$, this corresponds to $d = 198nm$, $a = 495nm$, $r = 165nm$. The bandgap of the infinite 2D photonic crystal of this thickness extends from $\frac{a}{\lambda} = 0.2983$ to $\frac{a}{\lambda} = 0.3884$.[28] The active layer (QW) is again centered in the middle of the dielectric membrane. We assume that the QW couples most strongly to TE modes, so we only analyze dipoles with the polarization in the plane of the QW. Dipoles appear uniformly throughout the area of the defect (i.e., the omitted central hole). The lifetime of dipoles is assumed to be $\tau_d = 0.1ps$.

The results of β_H for different dipole wavelengths λ_p are shown in Figure 1.38. In order

to account for the inhomogeneous broadening, we approximate the emission spectrum from the QW by a Lorentzian, centered at λ_s and with FWHM denoted by $\Delta\lambda_s$. Using the averaging technique described in Section 1.12.1, we calculate the value of the β factor for different values of the inhomogeneous broadening and the central frequency of the spectrum matched to the frequency of the fundamental mode. The results are given in Figure 1.39.

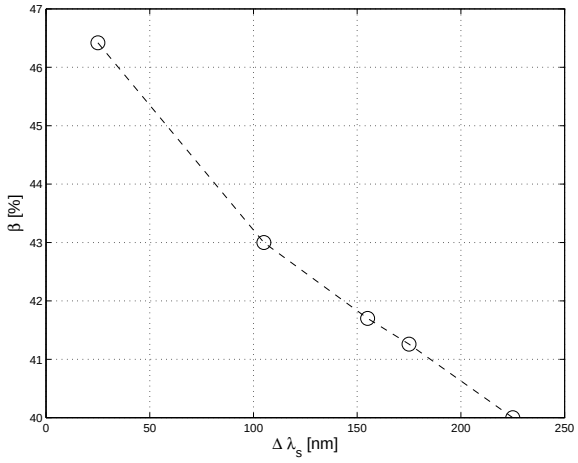

Figure 1.39: β factor calculation for the dipole mode of the microcavity based on 2D PBG in an optically thin dielectric slab; parameters of the cavity are described in text. On x axis we plot the FWHM of the emission spectrum. It is assumed that the emission is centered around $\lambda_0 = 1.55\mu m$.

In order to separate the contribution of guided modes and radiation modes to the β factor one can use the following approximate expression:

$$\beta = \frac{1}{N_g + \rho\Delta\lambda_s}, \tag{1.84}$$

where $\Delta\lambda_s$ is the width of the spontaneous emission spectrum, N_g is the number of guided modes within the spontaneous emission spectrum and ρ is an effective density of radiation modes at λ_s. In (1.84) it is assumed that the same amount of spontaneous emission goes into all guided modes within the emission spectrum and that the density of radiation modes is constant within $\Delta\lambda_s$. N_g can be counted from the spectrum determined using the FDTD. For $\Delta\lambda_s = 25nm$, $N_g = 2$ (doubly degenerate fundamental mode) and $\beta_H = 46.42\%$,

we calculate the effective density of radiation modes to be $\rho = 0.00617nm^{-1}$ which is around ten times smaller than in the microdisk which has a peak value of $\beta = 30.56\%$ and $\rho = 0.05nm^{-1}$, as we predicted in Reference 45. We attribute such a small ρ to the suppression of radiation modes by the 2D photonic crystal over a finite in-plane angular range, and to enhancement of spontaneous emission into the defect mode. This spontaneous emission enhancement is analyzed later in this chapter.

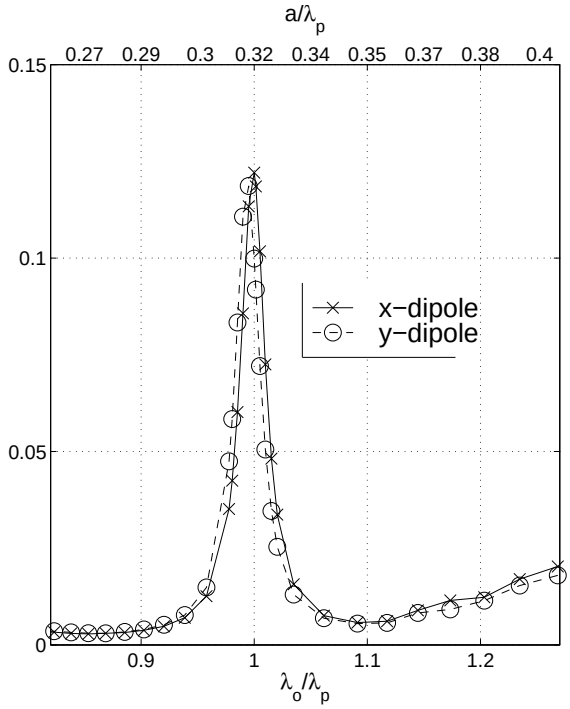

Figure 1.40: Total energy (in arbitrary units) radiated by a single electric dipole oriented in the x or y direction and positioned in the center of the defect. The microcavity is based on a 2D PBG in an optically thin dielectric slab. On the bottom x axis we show the ratio of the wavelength of the fundamental x-dipole mode λ_0 and the dipole's wavelength λ_p. On the top x axis we represent the ratio of the interhole spacing a and the dipole's wavelength λ_p.

We have also calculated the total energy radiated by a single electric dipole positioned in the center of the defect and oriented in the x or y direction for a range of dipole wavelengths λ_p. The dipole lifetime is assumed to be $0.1ps$. The result is shown in Figure 1.40. It can be observed that the total energies radiated by x and y oriented electric dipoles are approximately the same. This is explained by the fact that the fundamental mode is a set

of doubly degenerate dipole modes and the x oriented electric dipole strongly couples to x-dipole mode, while the y oriented electric dipole strongly couples to y-dipole mode. A small offset in positions of peaks is caused by a small difference in frequencies of x and y dipole modes, discussed in Section 1.4.1. As expected, the total radiated energies reach their maximum when dipole's wavelength coincides with the wavelength of the fundamental mode. When dipole's wavelength is offset from the wavelength of the fundamental mode in either direction, the total radiated energy drops, because we move within the bandgap and there is no other mode that the electric dipole can transfer its energy to. The drop in the total energy is gradual, due to the fact that the dipole emission spectrum is $25nm$ wide and at small distances from λ_0 tails of the emission spectrum still couple to the fundamental mode. Within the bandgap and off λ_0 we would have the inhibited spontaneous emission. A very interesting observation is that the total energy radiated by a dipole starts to increase slowly for $a/\lambda_p > 0.35$. This is due to coupling of dipole emission to conduction band modes (bottom of the conduction band is at $a/\lambda_p = 0.38$). One would expect the similar increase in the total radiated energy at lower frequencies, due to the coupling of dipoles to the valence band modes (valence band top is positioned at $a/\lambda_p = 0.29$). However, such increase is not observed in our calculations.

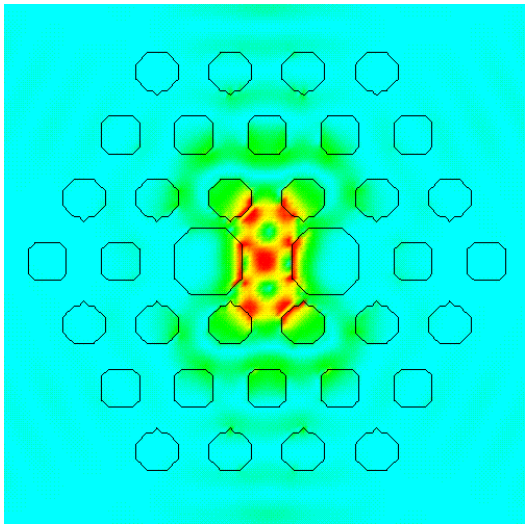

Figure 1.41: Cavity geometry for splitting of the dipole mode degeneracy and 2D slice through the middle of the slab showing the x-dipole mode electric field amplitude.

This is explained by the fact that valence (dielectric) band modes have their electric field energy concentrated in the high dielectric constant regions in the unperturbed photonic crystal. On the other hand, we position the electric dipole in the center of the defect, which corresponds to the air (hole) region in the unperturbed photonic crystal. This means that the electric field intensity of the valence band modes is small at electric dipole position and their coupling is weak. Therefore, there is no increase in the energy radiated by an electric dipole positioned in the center of a defect, due to the coupling to valence band modes. This also explains the high β values achievable for large FWHM of the emission spectrum, as shown in Figure 1.39, when the pumping area is small and limited to the defect. Therefore, in order to obtain a large β value in this type of the microcavity for large FWHM of the emission spectrum, it is desirable to have a defect mode frequency closer to the valence band top than to the conduction band bottom and to pump only the defect area. The latter can be achieved in practice by use of single quantum dot emitters.

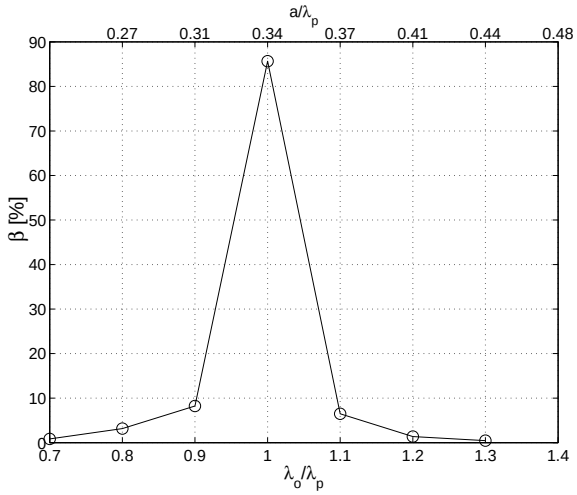

Figure 1.42: β factor dependence on the wavelength of the dipole excitation λ_p for the microcavity designed for degeneracy spliting of the dipole mode. Only the homogeneous broadening is taken into account.

The β factor can be almost doubled using the degeneracy splitting of the dipole modes. Degeneracy splitting can be accomplished by lowering the defect symmetry relative to that of the hexagonal lattice (as an example, by increasing the radius of the two nearest neighbor

holes along the x axis).[28] In the previously analyzed PBG membrane we increase the radii of the two nearest neighbor holes to $0.5a$ and move them $0.2a$ simultaneously toward the center defect in order to maintain the rib size in the x direction. We analyze the β factor of the x-dipole mode (shown in Figure 1.41), whose parameters are $Q = 224$ and $\frac{a}{\lambda_0} = 0.34$. The applied discretization was 15 units per interhole spacing a. In this microcavity, the y-dipole mode is pushed completely outside the bandgap.

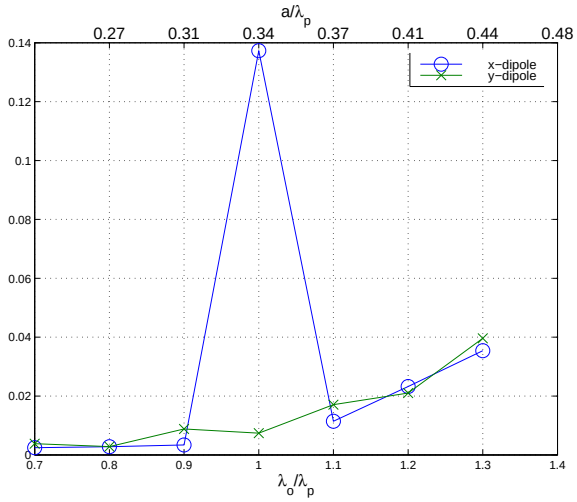

Figure 1.43: Total energy (in arbitrary units) radiated by a single electric dipole oriented in the x or y direction and positioned in the center of the defect. The microcavity geometry is designed for degeneracy splitting of the dipole mode and parameters are given in text. On the bottom x axis we show the ratio of the fundamental mode wavelength λ_0 and the dipole wavelength λ_p. On the top x axis we represent the ratio of the interhole spacing a and the dipole's wavelength λ_p.

Using the method described in previous sections, we calculate the β factor for this microcavity when only homogeneous broadening is taken into account. The homogeneous broadening is $25nm$, corresponding to dipole's lifetime of $0.1ps$ at $\lambda_0 = 1.55\mu m$. The emitting region is again assumed to be a single TE QW, positioned in the middle of the membrane. In order to decrease the amount of computation, we average β only over a single x and y oriented dipole positioned in the center of the defect. This approximation is good enough if the pumping area is small and limited to the defect. We test a range of dipole wavelengths λ_p. The result is shown in Figure 1.42. When dipole wavelength matches the wavelength of the

fundamental mode and the FWHM of the emission spectrum is equal to $25nm$, β factor as high as 85% can be achieved.

Once again, we calculate the total energy radiated by a single electric dipole positioned in the center of the defect and oriented in the x or y direction for a range of dipole wavelengths λ_p. The dipole lifetime was assumed to be $0.1ps$. The result is shown in Figure 1.43. The total energy radiated by the y oriented electric dipole is negligible within the bandgap. This can be explained by the fact that the y oriented electric dipole couples strongly to the y-dipole mode, which is pushed out of the bandgap with this cavity geometry. On the other hand, the total energy radiated by the x oriented electric dipole is still very strong within the bandgap, since it couples to the x-dipole mode which is located in the bandgap. A rise in the total radiated energy for both dipole orientations is again observed at high frequencies and the previous explanation (for the structure without degeneracy splitting) still holds.

In all previous calculations, it was assumed that the active region is a single quantum well positioned in the center of the membrane. Finally, we test the influence of the QW offset from the middle of the membrane to the β factor. We analyze β of the same structure at $\lambda_p = \lambda_0$, but for the QW positioned Δz above the middle of the membrane. Even when the QW is offset $70nm$ from the middle of the mebrane, β remains around 80%. The small drop in β due to the QW offset comes from the fact that the electric field intensity of the x-dipole mode doesn't change very strongly along the z direction within a membrane.[28]

1.13 Spontaneous emission rate modification in optical microcavities based on planar PC

Using the method described in the Section 1.12.2, we calculate the Purcell factors for the optical microcavity based on the planar PC. The analyzed structure is a single defect microcavity with the following parameters: $r/a = 0.3$, $d/a = 0.65$, $r_{def} = 0$, $a = 20$ and five layers of holes around the defect. We analyze the structure without ($p = 0$) and with ($p = 4$) fractional edge dislocation. Q factors and frequencies of the x-dipole mode for this set of parameters are shown in Figure 1.17. The classical dipole emitter, oscillating at the frequency of the defect mode, is placed in the center of the defect and oriented in the direc-

tion of the x axis. The calculated Purcell factors (spontaneous emission rate enhancements relative to the bulk semiconductor) are 29 and 58, for $p = 0$ and $p = 4$, respectively. The two-fold increase in the Purcell factor for $p = 4$ comes from the twofold increase in Q factor. Therefore, even for the modest values of the Q factor (several hundred), large Purcell factors are achievable in optical microcavities based on planar PC. This also implies large values of the β factor, as discussed in the previous sections. It is important to note that the calculated spontaneous emission rate enhancements represent theoretical limits. They are estimated for a zero linewidth source whose frequency is matched to the frequency of the defect mode, and which is positioned at the point of the maximum field intensity. In reality, the finite linewidth of the source and the spatial distribution of emitters introduce the reduction in Purcell factor: the averaged value will be much below the one estimated in this section. In order to reach the theoretical limit of the Purcell factor, it is important to have a narrow linewidth source positioned in the center of the defect and perfectly matched to the frequency of the cavity mode. Quantum dot emitters will be experimentally explored for this matter.

1.14 Fabrication

Our group at Caltech has developed fabrication procedures for making optical mirocavities based on planar PC, using a variety of semiconductor materials (Si, or III-V materials). In this section, only the fabrication procedure for cavities based on $Al_xGa_{1-x}As$ is presented. The material and PC properties are chosen in such a way that cavities operate at $\lambda = 852nm$ (the wavelength corresponding to the atomic transition in ^{133}Cs).

The fabrication procedure is outlined in Figure 1.44. The fabrication process starts by spinning of $100nm$ thick high molecular weight PMMA (polymethylmethacrylate) on top of the wafer. The PMMA layer is subsequently baked on a hot plate at 150^oC for 20 minutes. A desired 2D PC pattern is beamwritten on the PMMA by electron beam lithography in a Hitachi S-4500 electron microscope. The exposed PMMA is developed in a 3:7 solution of 2-ethoxyethanol:methanol for 30 seconds. The pattern is then transferred into the $Al_xGa_{1-x}As$ layer using the Cl_2 assisted ion beam etching. After that, the sacrificial $AlAs$ layer can either be (a) oxidized (step 6) or (b) dissolved in hydrofluoric acid (HF)

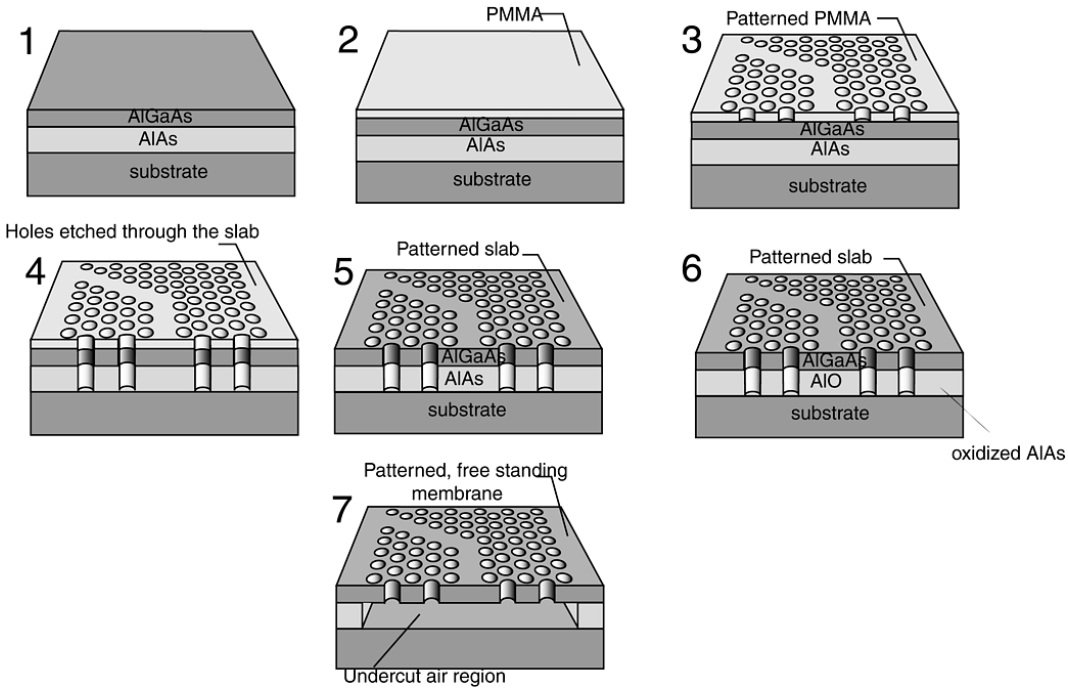

Figure 1.44: Fabrication procedure for optical microcavities based on $Al_xGa_{1-x}As$.

diluted in water (step 7). The oxidized AlO can also be dissolved in KOH. HF attacks $AlAs$ very selectively over $Al_xGa_{1-x}As$ for $x < 0.4$.[55] Therefore, the percentage of Al in our $Al_xGa_{1-x}As$ layer is around 30%. Finally, the remaining PMMA may be dissolved in acetone.

The SEM pictures showing the top views of the fabricated microcavities are shown in Figure 1.45.

1.15 Conclusion

Optical microcavities based on planar photonic crystals have been designed with Q factors over 10000 and mode volumes of the order of $0.5\left(\frac{\lambda}{n}\right)^3$. Large spontaneous emission rate enhancements (60) and β factors (85%) can be achieved in these structures, which makes them excellent candidates for light sources based on the single mode spontaneous emission, with high quantum efficiency and broad modulation width. We have also demonstrated theoretically that PC cavities can be designed for strong interaction with atoms trapped

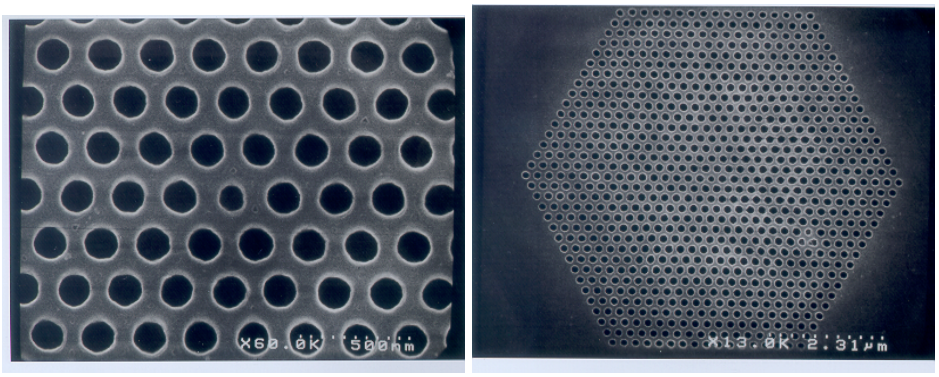

(a) (b)

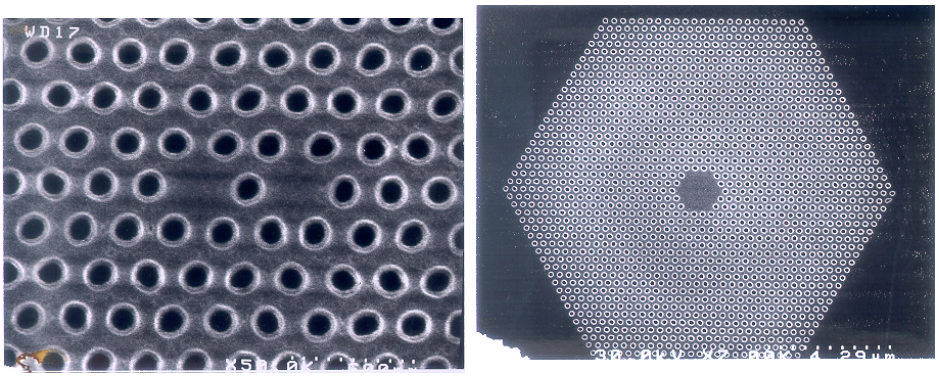

(c) (d)

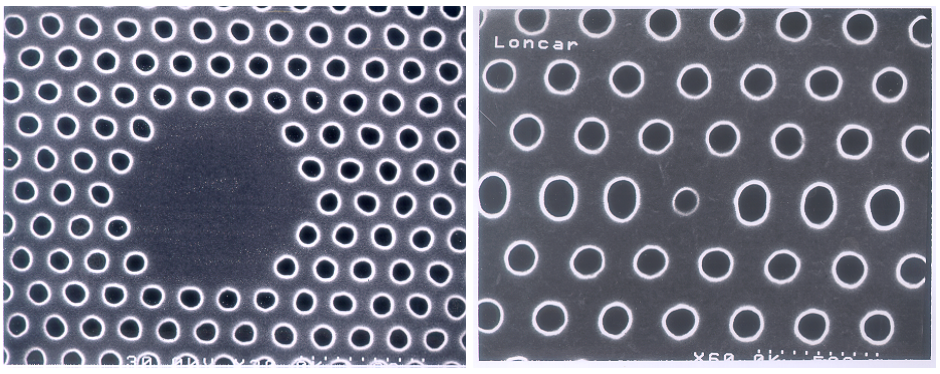

(e) (f)

Figure 1.45: SEM pictures showing the top views of the fabricated structures in $Al_xGa_{1-x}As$.

in one of the PC holes, which opens the possibility for using them in cavity QED experiments, or as building blocks of quantum networks. Structures have been fabricated and are presently being characterized for this purpose. Critical issues for further investigation include efficient coupling of light in and out of the PC microcavities, as well as the significance of surface effects that could perturb atomic radiative structure within the small defect hole. The extremely small mode volume in these structures also poses an interesting theoretical question of how standard cavity QED models must be modified when the single-photon Rabi frequency greatly exceeds the atomic hyperfine spacing. Using InAs quantum dots as internal photoluminescence sources, we have recently probed spectra of our photonic crystal microcavities, and experimentally demonstrated Q factors as high as 3000 for the x-dipole mode in the structures with fractional edge dislocations.[56] An extremely good match between theory and experiment was observed, since the theoretically predicted Q value for this structure was around 4000. We have also experimentally observed the tuning of Q values and frequencies of modes as a function of the elongation parameter p.

Chapter 2 Metallic photonic crystals

2.1 Introduction

For years, a significant amount of scientific work has been focused on improving the extraction efficiency of light emitting diodes. Many interesting approaches have been proposed to accomplish this, such as the use of thin light emitting layers with surface texturing,[57] resonant cavities[58] or photon recycling.[59] External quantum efficiencies of 31% were achieved by employing reflection from a bottom metal mirror together with a textured top semiconductor surface.[60] More than 10 years ago, scientists at the Walter Schottky Institute in Germany[61] were able to improve the extraction efficiency of a flat AlGaAs/GaAs double heterostructure light-emitting diode, by adding a 1D periodic metallic structure on top of it. After etching a 1D grating on the semiconductor surface and coating it with a thin metal layer, the extraction efficiency increased from 1% to 1.5%. Even though the measured efficiencies were quite modest, these results were very important, since they broke a taboo that adding metal to a light emitting device can only ruin its efficiency.

Apart from efforts to improve light extraction from a semiconductor device, it is also possible to enhance the light emission rate within a semiconductor. This approach is based on Purcell's prediction in 1946 that the radiation rate of an atom placed within a wavelength-sized cavity can be changed.[33] A 12-fold enhancement of spontaneous emission was recently measured in a semiconductor optical microcavity at low temperatures.[36] Metallic structures were identified as candidates for very large decay rate enhancement - much larger than the one achievable by semiconductor photonic crystals. Yablonovitch and coworkers[62] were able to measure a 55 times reduction in lifetime, when an InGaN/GaN quantum well (QW) was positioned close ($12nm$) to a thin silver layer. Unfortunately, they were not able to extract any light outside the structure.

In order to build an ideal, highly efficient light-emitting diode (LED), it is desirable to improve the extraction efficiency and simultaneously enhance the spontaneous emission rate.

A 15-fold emission intensity enhancement, with Purcell factor $F_p = 2$, was observed in 2D periodic photonic crystals, made out of semiconductors.[63] Metallic photonic crystals have also attracted significant scientific attention in recent years. In 1996, scientists from the thin film photonics group at the University of Exeter in United Kingdom observed a photonic bandgap for surface modes on a silver surface textured with a hexagonal array of dots.[64] Two years later, researchers at NEC and their collaborators[65] observed sharp peaks in the transmission of light through a metallic layer patterned with a hexagonal array of subwavelength holes. Both experimental results were attributed to the peculiar properties of surface plasmons polaritons - modes that exist at the interface of two media with opposite signs of the real part of dielectric constant.

At the beginning of 1999, we started our work on using metallic photonic crystals to build highly efficient LEDs. Our attempt was inspired by the potential that metals have with regards to the spontaneous emission rate enhancement,[62] and the possibility of efficient light extraction with properly designed periodic structures.[63] We envisioned metallic photonic bandgap structures (PBGs) as periodic metallic structures (similar to printed circuits) on the surface of a semiconductor wafer. This approach brings with it a key advantage over semiconductor PBGs: there is no need to etch through the semiconductor, which simplifies the fabrication procedure, and also avoids nonradiative losses due to surface recombination. However, there were many problems encountered along the way of making an efficient light emitting device. The biggest were inherent absorption losses in metals at optical frequencies. Nevertheless, we were able to achieve large efficiencies,[66,67] as will be described in this chapter.

2.2 Optical properties of bulk metals

At optical wavelengths, metals are characterized by a large, negative real part of dielectric constant. Both real and imaginary parts of their dielectric constant exhibit a strong frequency dependence. Some types of metals (such as alkali, or noble metals) can be successfully modeled as free electron gases in this frequency range. As an example, the dielectric constant of silver is dominated by free electron behavior below $4eV$.[68] Optical properties of free electron metals can be described using a simple Drude-Lorentz model.[68,69] This model

assumes that the response of the metal to an external field can be obtained by multiplying the response of a single free electron by a number of electrons (i.e., all free electrons respond in phase to the external field excitation). The motion of an electron in the applied electric field is described by the dynamic equation:

$$m\frac{\partial \vec{v}}{\partial t} = -\Gamma m\vec{v} - e\vec{E}_{tot}, \tag{2.1}$$

where m, e and $\vec{v}$ are mass, charge and velocity of electron, respectively, Γ is the damping rate and $\vec{E}_{tot}$ is the total electric field acting on the electron. The damping rate Γ can be expressed as $\Gamma = 2\pi\nu$, where ν is the collision frequency (the frequency of scattering events). In the Drude-Lorentz model, an electron reaches thermal equilibrium with a system through a series of scattering events with ion cores. Without scattering, electron oscillations excited by the external AC electric field would not be damped. The difference between Drude and Lorentz models lies in the definition of $\vec{E}_{tot}$. In the Drude model, the influence of the electric field of other electrons is neglected, i.e., $\vec{E}_{tot} = \vec{E}$, where $\vec{E}$ is the externally applied electric field. However, in the Lorentz model $\vec{E}_{tot} = \vec{E} - \frac{\vec{P}_{fe}}{\epsilon_0\chi_0}$, where $\vec{P}_{fe}$ is the polarization of the free electron gas and χ_0 is the DC response of this polarization to the electric field. Since all free electrons respond identically to the external field, the total current of the free electron gas can be expressed as

$$\vec{J} = -ne\vec{v}, \tag{2.2}$$

where n is the concentration of free electrons. Current can also be expressed as

$$\vec{J} = \frac{\partial \vec{P}_{fe}}{\partial t} \tag{2.3}$$

After plugging equations 2.2 and 2.3 into the dynamic equation 2.1, we arrive at the differential equation describing $\vec{P}_{fe}$ in the Lorentz-Drude model:

$$\frac{\partial^2 \vec{P}_{fe}}{\partial t^2} + \Gamma\frac{\partial \vec{P}_{fe}}{\partial t} = \epsilon_0\omega_p^2\vec{E}_{tot}, \tag{2.4}$$

where ω_p is the plasma frequency of a metal, defined as

$$\omega_p^2 = \frac{ne^2}{\epsilon_0 m} \tag{2.5}$$

The behavior of metals is described by equation 2.4 and Maxwell curl equations:

$$\vec{\nabla} \times \vec{H} = \epsilon_\infty \epsilon_0 \frac{\partial \vec{E}}{\partial t} + \frac{\partial \vec{P}_{fe}}{\partial t} \tag{2.6}$$

$$\vec{\nabla} \times \vec{E} = -\mu_0 \frac{\partial \vec{H}}{\partial t}, \tag{2.7}$$

where ϵ_∞ is the relative dielectric constant describing the behavior of a metal at large frequencies and includes all other conduction mechanisms beside free electrons.
Let us assume that the AC electric field with frequency ω is applied to metal:

$$\vec{E} = \vec{E}_0 e^{i\omega t} \tag{2.8}$$

The total dielectric constant of a metal at frequency ω can be expressed as

$$\epsilon(\omega) = \epsilon_\infty \epsilon_0 - i\sigma(\omega)/\omega, \tag{2.9}$$

where $\sigma(\omega)$ is the conductivity of the metal due to free electrons. The relation between $\sigma(\omega)$ and $\vec{J}$ is

$$\vec{J} = \frac{\partial \vec{P}_{fe}}{\partial t} = \sigma(\omega)\vec{E} \tag{2.10}$$

From equations 2.4, 2.8, 2.9 and 2.10 we can easily derive $\epsilon(\omega)$ in the Lorentz model:

$$\epsilon(\omega) = \epsilon_\infty \epsilon_0 + \frac{\epsilon_0 \omega_p^2}{\omega_p^2/\chi_0 - \omega^2 + i\omega\Gamma}, \tag{2.11}$$

or in the Drude model:

$$\epsilon(\omega) = \epsilon_\infty \epsilon_0 + \frac{\epsilon_0 \omega_p^2}{-\omega^2 + i\omega\Gamma} \tag{2.12}$$

Starting from the Drude model, for lossless medium ($\Gamma = 0$) and for $\epsilon_\infty = 1$, we obtain a famous relationship for the dielectric constant of metals at optical frequencies:

$$\epsilon(\omega) = \epsilon_0 \left(1 - \frac{\omega_p^2}{\omega^2}\right) \tag{2.13}$$

Therefore, at frequencies smaller than the plasma frequency, metals have a negative real part of dielectric constant.

2.3 Nonradiative surface plasmons on smooth surfaces

Surface plasma oscillations are coherent oscillations of free electrons on a metallic surface. These charge oscillations are followed by an electromagnetic wave called the surface plasmon (SP). Surface plasmons (also called surface plasmons polaritons) are electromagnetic surface waves that propagate along metallic surfaces, have their intensity maximum at the surface and exponentially decaying fields perpendicular to it. The conditions for occurrence of such localized waves at the boundary between two media are as follows[70] :

1. Two regions on different sides of the boundary must have opposite signs of the real part of the dielectric constant (otherwise, a strong field localization at the surface cannot be obtained). Following our discussion in the previous section, this is possible at the interface between a metal operating at frequencies below ω_p and any dielectric.

2. Polarization of the SP wave has to be TM (p). This means that the wave has a B field parallel to the surface of the metal and E field components in the plane perpendicular to $\vec{B}$.

The simplest case to analyze is the SP wave occurring on a smooth, infinite surface separating half-spaces filled with metal and dielectric, respectively. Let the relative dielectric constants of metal and dielectric be $\epsilon_1 = \epsilon_1' - i\epsilon_1$" and ϵ_2, respectively. At frequency ω, such that ϵ_1' and ϵ_2 have opposite signs, a TM wave can be excited at this interface, propagating along the surface with wavevector k and exponentially decaying in the perpendicular direction with decay constant α_i (where $i = 1, 2$ corresponds to two different regions). The

dispersion relation for this wave is:[70]

$$k = k' + ik" = \frac{\omega}{c}\sqrt{\frac{\epsilon_1\epsilon_2}{\epsilon_1 + \epsilon_2}}, \tag{2.14}$$

where c is the speed of light in vacuum. Therefore, the SP wave propagates with wavevector k' along the interface, and exponentially decays in the direction of propagation with decay constant $k"$:

$$k' = \frac{\omega}{c}\sqrt{\frac{\epsilon_1'\epsilon_2}{\epsilon_1' + \epsilon_2}} \tag{2.15}$$

$$k" = \frac{\omega}{c}\left(\frac{\epsilon_1'\epsilon_2}{\epsilon_1' + \epsilon_2}\right)^{3/2}\frac{\epsilon_1"}{2(\epsilon_1')^2} \tag{2.16}$$

The exponential decay in the direction of propagation occurs due to losses in metal, i.e.,

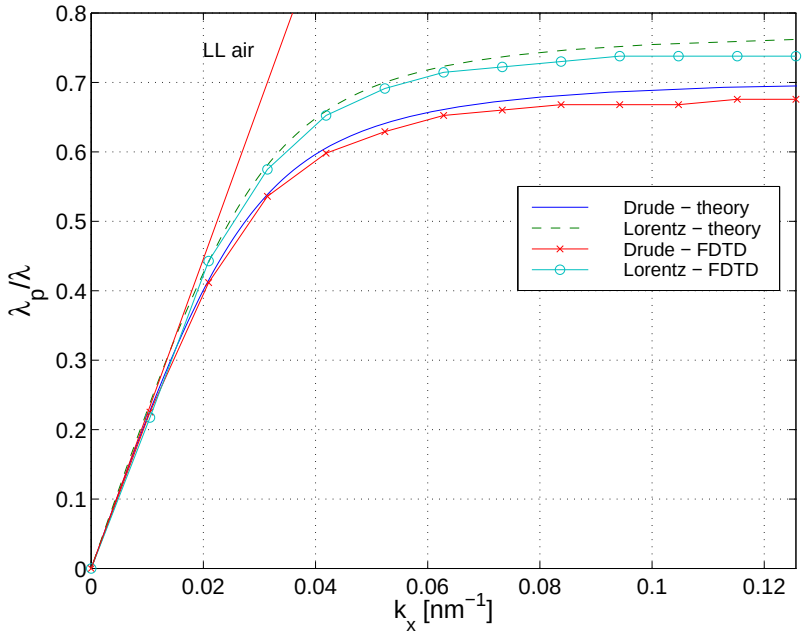

Figure 2.1: Dispersion diagrams for SP waves at the smooth interface between halfspaces filled with silver and air. Parameters of Drude and Lorentz model are: $\epsilon_\infty = 1$, $\omega_p = 2\pi c/\lambda_p$, where $\lambda_p = 140nm$, $\Gamma = 0$ and $\chi_0 = 10$.

for $\epsilon_1" \neq 0$.

Beside the exponential decay in the direction of propagation, the wave exponentially also decays in the perpendicular direction, into the two regions on the opposite sides of the

boundary. The decay constants α_i $(i = 1, 2)$ can be found easily from the following relation:

$$k^2 - \alpha_i^2 = \epsilon_i (\frac{\omega}{c})^2 \tag{2.17}$$

ϵ_1' and ϵ_1" can be expressed from the Drude or Lorentz model introduced previously. For $\epsilon_1' \gg \epsilon_1$" (which holds for metals at optical wavelengths), α_i are real and equal to

$$\alpha_1 = \frac{\omega}{c} \sqrt{\frac{-(\epsilon_1')^2}{\epsilon_1' + \epsilon_2}} \tag{2.18}$$

$$\alpha_2 = \frac{\omega}{c} \sqrt{\frac{-(\epsilon_2)^2}{\epsilon_1' + \epsilon_2}} \tag{2.19}$$

The penetration depths of the SP wave into the two media are then

$$d_{p1} = 1/\alpha_1 = \frac{\lambda}{2\pi} \sqrt{\frac{\epsilon_1' + \epsilon_2}{-(\epsilon_1')^2}} \tag{2.20}$$

$$d_{p2} = 1/\alpha_2 = \frac{\lambda}{2\pi} \sqrt{\frac{\epsilon_1' + \epsilon_2}{-(\epsilon_2)^2}} \tag{2.21}$$

Throughout this chapter we will use the following parameters of Drude and Lorentz model for silver:[70, 71] $\epsilon_\infty = 1$, $\omega_p = 2\pi c/\lambda_p$, where $\lambda_p = 140nm$ (i.e., the energy of bulk plasmons is $\hbar\omega_p = 8.8eV$), $\Gamma = 0$ and $\chi_0 = 10$. Furthermore, coordinate axes are always chosen in such a way that the wave propagates in the x direction, and that the p-polarized (TM) light has x and y components of electric field and z component of magnetic field, while the s-polarized (TE) light has x and y components of magnetic field and z component of electric field. Dispersion relations of the SP wave excited at the interface between silver and air ($\epsilon_2 = 1$) are shown in Figure 2.1. Dispersion diagrams obtained by the finite-difference time-domain (FDTD) simulation are shown in the same plot. A very good match between theory and the FDTD simulation can be observed. (For the details of the FDTD code, please refer to the Appendix I of this thesis). λ denotes the wavelength of the SP mode measured in air, and k_x is the wavevector in the direction of propagation. In the same plot, we also show the light line in air ($\frac{\lambda_p}{\lambda} = \frac{\lambda_p c k_x}{2\pi}$). Therefore, SP waves occurring on a smooth surface are nonradiative. Their dispersion diagram lies below the light line in air, and they are completely confined to the surface of the metal (i.e., guided on it). In the general case

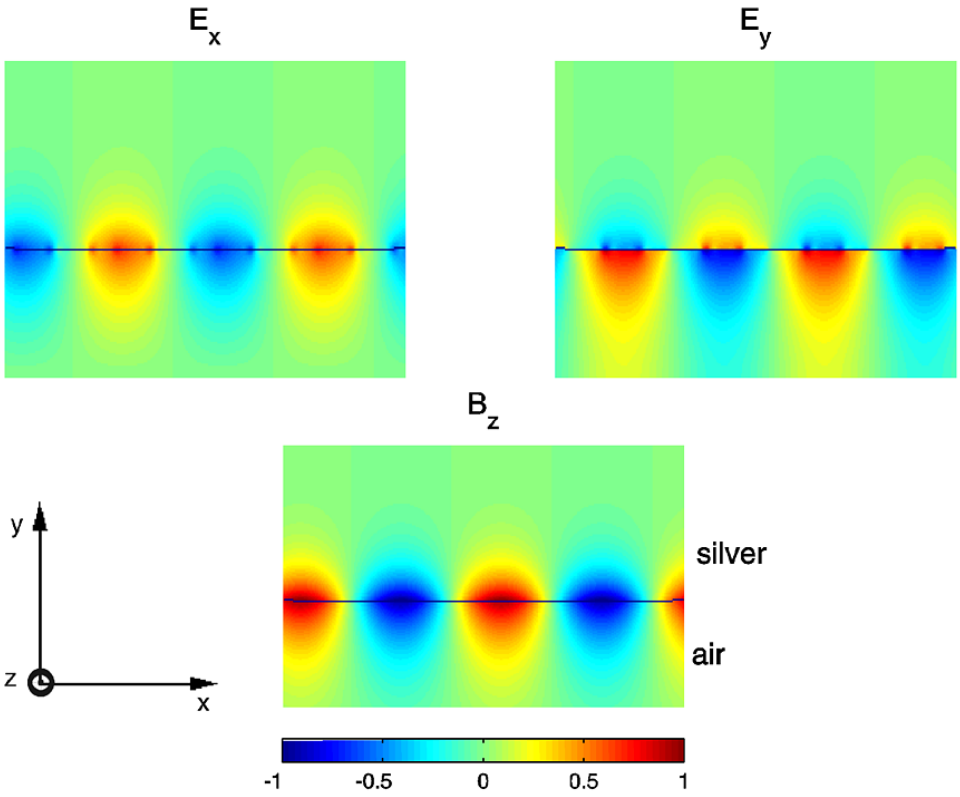

Figure 2.2: Field profile of the SP wave at the smooth interface between halfspaces filled with silver and air. In the FDTD analysis, Drude model was used, with parameters given in Figure 2.1. For the shown mode, $k_x = 0.0419nm^{-1}$ and $\lambda_p/\lambda = 0.6$. Horizontal dimensions of figures correspond to $300nm$.

of the SP wave excited at the interface between metal and dielectric with dielectric constant ϵ_2, the dispersion diagram would lie completely below the light line in that dielectric. The field patterns of the SP wave with $k_x = 0.0419nm^{-1}$ and $\lambda_p/\lambda = 0.6$, obtained using the FDTD method, are shown in Figure 2.2. Due to the opposite sign of dielectric constants of the two media, the perpendicular component of the electric field (E_y) also changes sign across the interface. A strong confinement to the interface and exponential decay in the perpendicular direction (y) can also be observed.

Another interesting observation is that the dispersion diagram flattens at large values of the wavevector. The flattening happens as ϵ_1' approaches ϵ_2 and the frequency of the SP wave saturates at $\omega_{max} = \frac{\omega_p}{\sqrt{\epsilon_\infty + \epsilon_2}}$ (according to Drude model). This implies that at those k_x

values, a very large density of surface plasmon states can be obtained (density of states $\rho(\omega)$ is proportional to $\frac{d\omega}{dk_x}$). On the other hand, from Fermi's golden rule, the recombination rate is directly proportional to $\rho(\omega)$. Therefore, at large values of the wavevector, a large increase in the recombination rate and a large lifetime reduction can be obtained. Yablonovitch and coworkers[62] observed this effect in 1999: the lifetime of an electron-hole pair in InGaN/GaN quantum well (positioned $12nm$ from silver mirror) was reduced 55 times. Even though the emitters in the quantum well were radiating 55 times faster in the presence of silver mirror, all of that radiation was coupled to surface plasmon waves confined to the interface between metal and semiconductor. Therefore, no radiation could be observed outside of the structure. The authors indicated at the very end of the paper a necessity for designing "an efficient antenna nanostructure" that could scatter light outside.

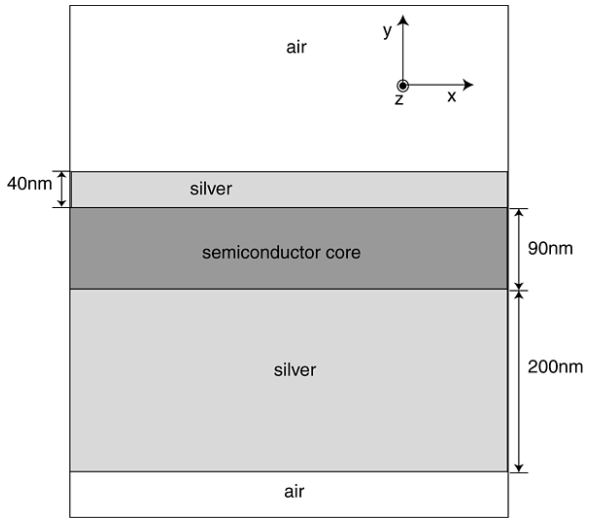

Figure 2.3: Semiconductor slab waveguide with metallic claddings, analyzed using the FDTD method. The structure is infinite in the z direction. Mur's absorbing boundary conditions are applied to boundaries in the y direction and Bloch boundary conditions are applied to boundaries in the x direction.

2.4 Coupled surface plasmons

At the beginning of 1999, we started our work on metallic photonic crystals at Caltech. The goal was to design structures that can efficiently extract radiation coupled to SP waves, and

therefore be used in light emitting devices. Instead of trying to reach the ultra-high density of states at large k_x, we decided to design structures that operate at frequencies lower than ω_{max}. Even though lifetime modifications cannot be as large as at the frequency ω_{max} (due to the smaller density of states), there are advantages of operating in this frequency region. One of them is that there is more freedom in choosing a material system, since there is no need to match the emission from a quantum well (QW) to ω_{max}. This frequency matching is a difficult and expensive process. For example, we recall that silver has $\lambda_p = 140nm$ and $\epsilon_\infty = 1$. Therefore, $\lambda_{min} = 2\pi c/\omega_{max}$ for silver layer on a typical III-V semiconductor (with refractive index of 3.5) is $510nm$, which is outside the emission range of standard III-V materials. For this reason, the UCLA researchers had to use GaN substrates with InGaN QWs, which are presently still expensive and difficult to grow.

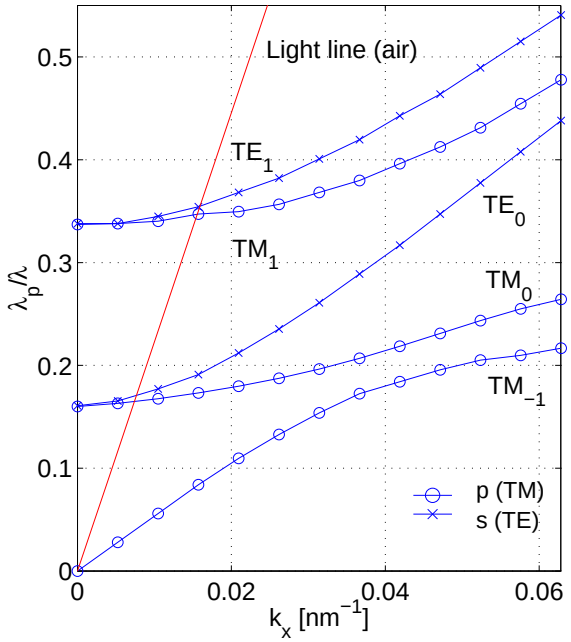

Figure 2.4: Band diagram of the structure shown in Figure 2.3. Absorption losses in silver were not included.

In order to couple the emission to SP waves at ω_{max}, Yablonovitch and coworkers[62] also had to position the QW very close ($12nm$) to the metal surface and within the fringing field depth of the SP. However, the nonradiative transfer between a QW and metal increases as

their distance decreases.[72] The question is then how much of the observed large reduction in lifetime at small distances is due to the coupling to SP waves, and what portion of it comes from other nonradiative processes. The only part that can be possibly extracted outside of the structure by properly designing an "antenna" (i.e., by structuring the surface of metal) is the portion coupled to SP waves. To reduce the non-radiative transfer, we decided to position the QW further from the metal surface (at distances of 40 to $50nm$). However, the intensity of SP waves decreases exponentially as a function of distance from the metallic surface. Now the advantage of operation below ω_{max} comes into play, since the penetration depth increases with λ, according to equation 2.21. Therefore, at larger wavelengths, SP waves extend more into the semiconductor and can interact with emitters in the QW positioned further from the metallic surface. In order to increase the field intensity at the position of the QW even more, we started exploring the coupled surface plasmon modes of two closely spaced metallic interfaces.[71] Again, the coupling between two metallic surfaces increases as a function of wavelength, since the penetration depths of the SP waves into the semiconductor increase.

Let us analyze (using the FDTD method) the band diagram of a semiconductor slab waveguide with metal cladding, shown in Figure 2.3 (also referred to as the metal clad microcavity[71]). The semiconductor membrane is $90nm$ thick, with refractive index of $n = 3.5$. The top semitransparent silver layer is $40nm$ thick, and the bottom non-transparent silver layer is $200nm$ thick. The band diagram would not change if the non-transparent silver layer was thicker than $200nm$. The advantage of setting this layer as thin as possible during the FDTD analysis is the reduction in computational memory and time needed for the simulation. The analyzed structure is surrounded by air on top and bottom and the slab is infinite in the horizontal plane, and the Drude model is used in the calculation for which the result is shown in Figure 2.4.

The coupling between SP waves of the top and bottom metal-semiconductor interface produces two additional electromagnetic waves:[71] the asymmetric coupled SP mode (ASP, corresponding to the branch TM_{-1}), and the symmetric coupled SP mode (SSP, corresponding to the branch TM_0). At large frequencies (approaching ω_{max}), the penetration depth of the SP wave into the semiconductor (d_{p2}) approaches zero (as can be seen in Figure 2.5), and the coupling between the SP modes of the two metallic surfaces diminishes. The

ASP and SSP branches then become degenerate and both turn into the dispersion relation of the SP wave excited on a single smooth surface between metal and semiconductor. From Figure 2.5, it follows that d_{p2} is approximately $80nm$ at a wavelength of $1\mu m$. Therefore, at a distance of $45nm$ (corresponding to the middle of the semiconductor slab), the SP field magnitude drops to 57% of its maximum value at the metal surface. However, if two metallic surfaces are positioned $90nm$ from each other, the field magnitude in the middle of the semiconductor core would be two times larger (in the case of constructive interference), because of contributions from the two interfaces. Therefore, we can achieve very strong fields at the position of our QW, without having to put the QW very close to the metal surface (as UCLA researchers did), and without fear of large non-radiative transfer.

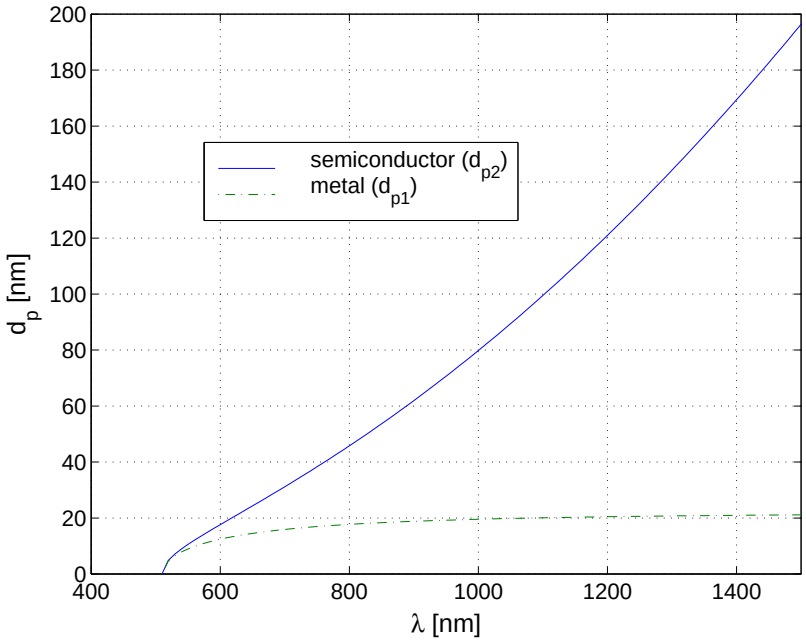

Figure 2.5: Penetration depth of the SP wave into metal or dielectric, as a function of its wavelength. The SP wave is excited at the interface between silver and semiconductor (refractive index $n = 3.5$). The penetration depth drops to 0 at the wavelength $\lambda_{min} = 2\pi c/\omega_{max} = 510nm$.

The field distributions of the ASP and SSP modes with $k_x = 0.026nm^{-1}$ and wavelengths $\lambda_p/0.132$ and $\lambda_p/0.1952$, respectively, are shown in Figures 2.6 and 2.7. The ASP mode has a maximum of the E_y field component in the middle of the membrane, while the SSP has a

minimum of the E_y field there. The names ASP and SSP come from the charge distribution on the metal plates, which is accompanied by the SP mode. In the case of the ASP, for example, the charge distribution on the plates must be asymmetric with respect to the middle of the slab. Let us analyze electromagnetic fields in the middle of the membrane, where the QW will be located in real structures. Perpendicular dipoles positioned in the QW will couple strongly to the ASP mode, while parallel dipoles can couple to the SSP mode. In addition, parallel dipoles can couple strongly to TE modes.

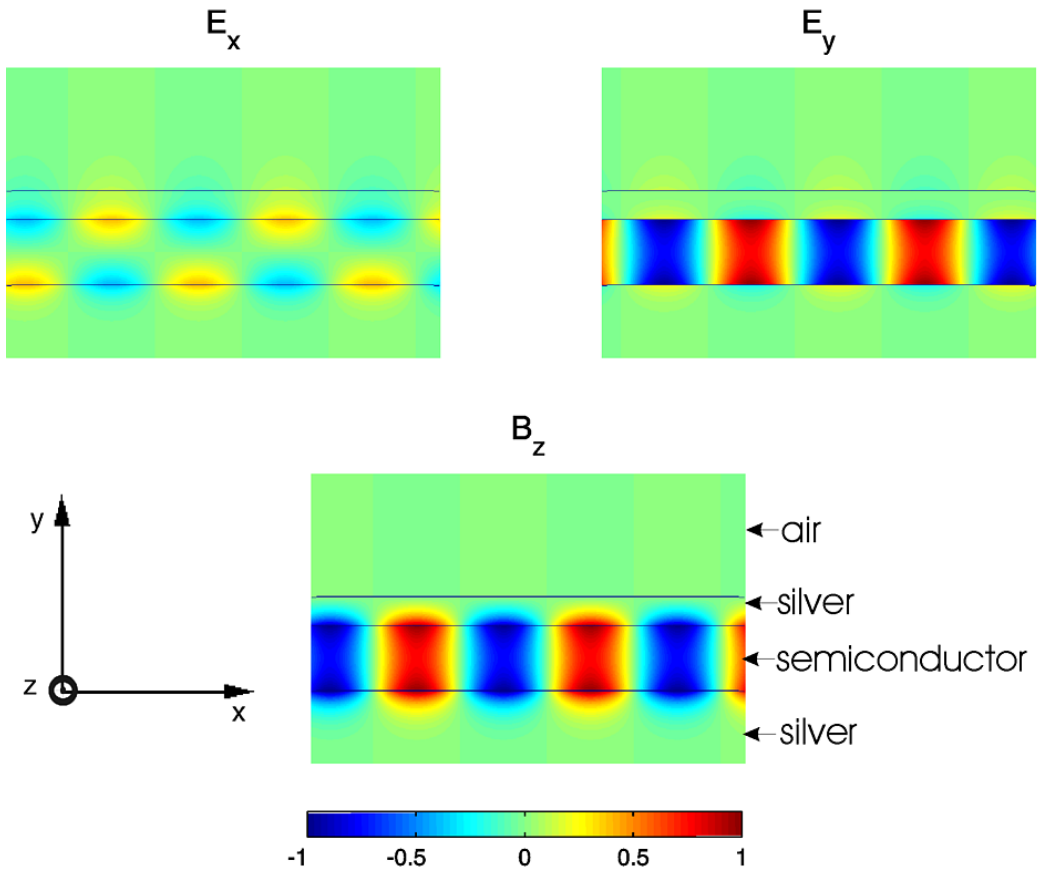

Figure 2.6: Electric and magnetic field components for the ASP (TM_{-1}) mode, with $\frac{\lambda_p}{\lambda} = 0.132$ and $k_x = 0.026nm^{-1}$. The analyzed structure has the same parameters as the one whose band diagram is shown in Figure 2.4. Horizontal dimension corresponds to $600nm$.

Three important properties of the previously presented band diagram are worth noting at this point. First, bands are lossy in reality, due to absorption both in the metal, and

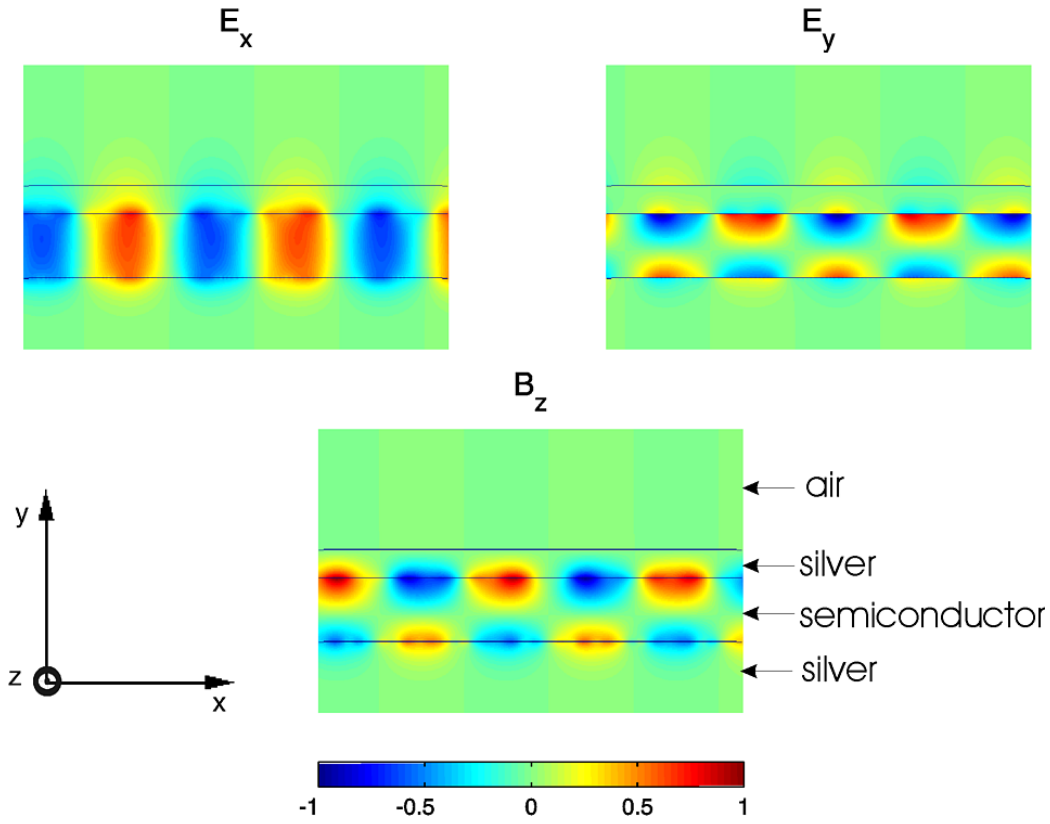

Figure 2.7: Electric and magnetic field components for the SSP (TM_0) mode, with $\frac{\lambda_p}{\lambda} = 0.1942$ and $k_x = 0.026nm^{-1}$. The analyzed structure has the same parameters as the one whose band diagram is shown in Figure 2.4. Horizontal dimension corresponds to $600nm$.

the semiconductor. This implies that each band is spread over some frequency range, determined by its Q factor. Therefore, the band cutoff (for example for TE_0 and TM_0 at frequency $0.16\omega_p$) is not abrupt, but gradual instead. Using the 1D finite difference method, we evaluated the cutoff frequency of the TE_0 mode when absorption losses in both metal and semiconductor were included and concluded that it was positioned at $\frac{\lambda_p}{\lambda} = 0.15$ instead of 0.16, as in the lossless band diagram shown in Figure 2.4. Secondly, the position of the TM_{-1} band is not very strongly dependent on the semiconductor core thickness. At large k_x values, this mode always coincides with the dispersion diagram of the SP mode on the semiconductor-metal interface. The final property of the band diagram is related to the modes of the top thin metallic film. The SP modes can occur on both surfaces of this metal layer (i.e., on air, or semiconductor side). For a very thin metal film (of the order

of a penetration depth of the SP wave into metal), these two SP modes are coupled.[70] As the thickness of this layer increases, the two states become decoupled and their dispersion relations converge to the dispersion relations of the SP modes at the interface between metal and air, or metal and semiconductor. Keeping in mind that the penetration depth of the SP wave into silver is on the order of $20nm$ or less (see Figure 2.5), we conclude that for a metal film thickness of $40nm$, these two states will be very weakly coupled. Moreover, the mode of the interface between air and metal will be very strongly damped in the metal and will have insignificant intensity within the semiconductor. Therefore, emitters in the QW cannot couple to this mode. Since it does not affect device properties, this mode is omitted from the dispersion diagrams for clarity. The other SP mode (of the interface between metal and semiconductor) is coupled with the appropriate SP mode of the bottom metal surface, producing the ASP and SSP states, shown in the band diagram.

2.5 Decay rate enhancement and external efficiency of semiconductor slabs with metal claddings

Let us denote by $\frac{1}{\tau_r}$ the rate at which photons are radiated outside the structure and by $\frac{1}{\tau_{nr}}$ the decay rate corresponding to all other mechanisms (such as absorption losses or the excitation of modes that remain trapped within the structure). The total decay rate is defined as

$$\frac{1}{\tau} = \frac{1}{\tau_r} + \frac{1}{\tau_{nr}} \tag{2.22}$$

The external efficiency (η_{ext}) can be expressed as follows:[63]

$$\eta_{ext} = \frac{\frac{1}{\tau_r}}{\frac{1}{\tau_r} + \frac{1}{\tau_{nr}}} = \frac{\frac{1}{\tau_r}}{\frac{1}{\tau}} \tag{2.23}$$

The Purcell factor (F_p) is defined as the spontaneous emission rate enhancement in a microcavity relative to a bulk semiconductor. On the other hand, we define the decay rate enhancement (F_d) as a ratio of the total decay rate in a microcavity and the spontaneous

emission rate in a bulk semiconductor:

$$F_d = \frac{\frac{1}{\tau}}{\frac{1}{\tau_0}} \tag{2.24}$$

The speed at which an LED can be modulated is proportional to F_d. When analyzing a light emitting device, we also care about the overall efficiency, defined as a product of F_d and the external efficiency η_{ext}:

$$F_d \cdot \eta_{ext} = \frac{\frac{1}{\tau_r}}{\frac{1}{\tau_0}} \tag{2.25}$$

The efficiency is a measure of how much faster the rate of light emission from the cavity

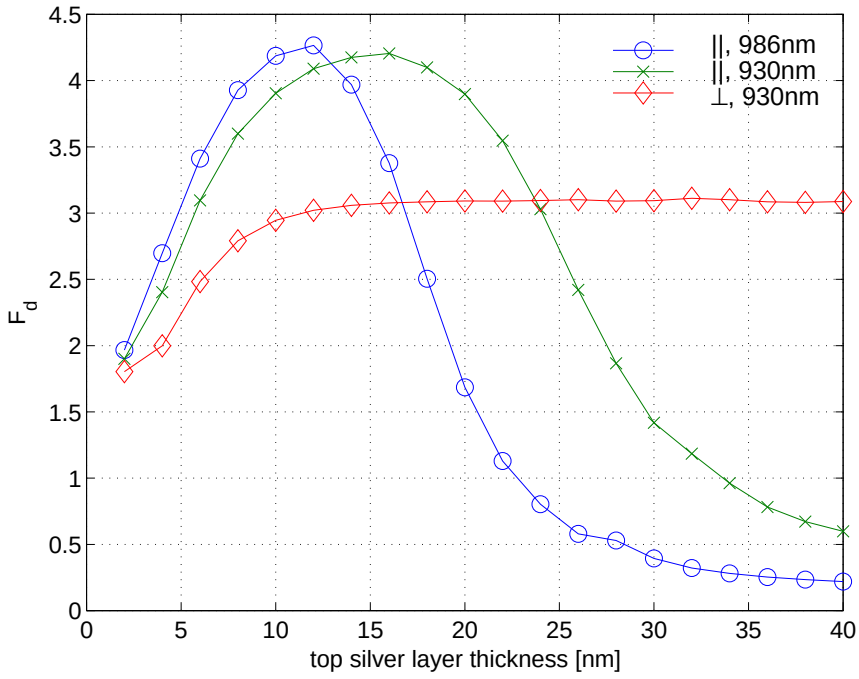

Figure 2.8: The calculated decay rate enhancement for the $90nm$ thick semiconductor core with metal claddings. The emitter is a parallel or a perpendicular dipole positioned in the middle of the membrane. The bottom metal layer is infinitely thick, while the top metal layer thickness changes. The dipole is oscillating at the wavelength of $986nm$ or $930nm$.

to the outside world is, than the spontaneous emission rate in a bulk semiconductor.

We evaluated F_d analytically for a metal clad semiconductor waveguide using the method described in Reference 73. The result is shown in Figure 2.8. Subscripts $||$ and $\perp$ denote

parallel and perpendicular dipoles, respectively. The reason for choosing wavelengths of $986nm$ and $930nm$ and the appropriate dipole orientations results from the emission properties of InGaAs QW used in the experiment that will be described later in this chapter. The main emission peak from the InGaAs/GaAs QW is centered at $986nm$, which corresponds to conduction to heavy hole band transitions (C-HH). There is also a peak at $930nm$, corresponding to conduction to light hole band transitions (C-LH), which becomes more prominent at higher pumping levels. C-HH transitions couple to electric fields polarized in the QW plane ($x-z$ plane). On the other hand, C-LH transitions couple twice as strongly to electric fields with polarization perpendicular to the QW plane (y direction) than to those polarized in the QW plane.[74] In the classical spontaneous emission model, C-HH transitions are represented with parallel dipoles, while C-LH transitions are represented with both parallel and perpendicular dipoles, weighted by factors 1/3 and 2/3, respectively. Therefore, in our metal clad semiconductor waveguide, we can achieve lifetime reductions

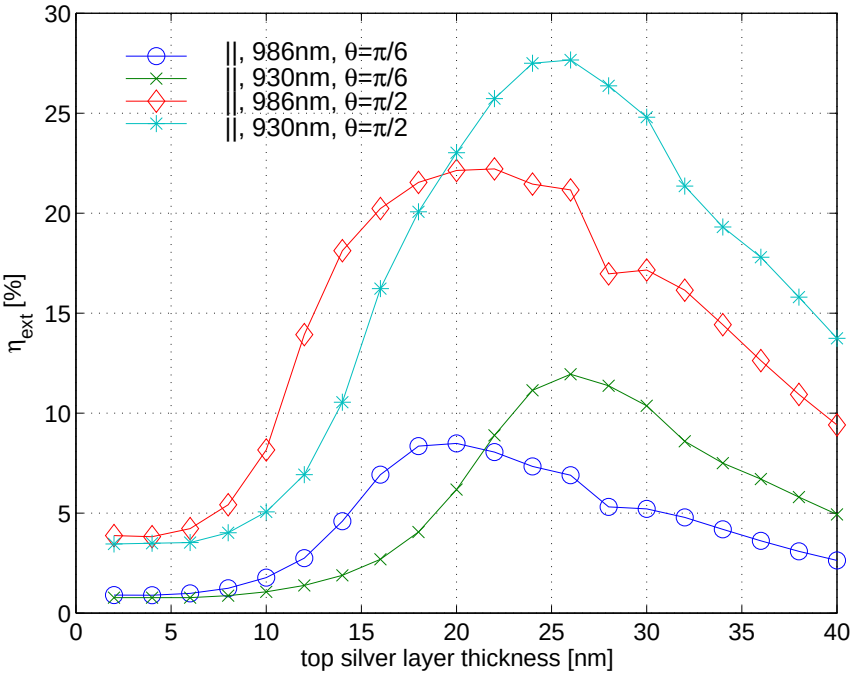

Figure 2.9: The calculated external efficiency for the semiconductor slab with metal cladding (metal clad microcavity), as a function of the top, semitransparent silver layer thickness. We calculated η_{ext} into the 30^o or 90^o collection angle. The emitter is a parallel dipole positioned in the middle of the $90nm$ thick semiconductor membrane, oscillating at the wavelength of $986nm$ or $930nm$.

of up to 4.3 times. The question is now how much of this radiation can be extracted out. The external efficiency for planar structures without metal patterning can be evaluated using the method described in References 73 and 75. We calculated the external efficiency of the same semiconductor waveguide with metal cladding, as a function of the top, semi-transparent silver layer thickness, and for the collection angles of 30^o or 90^o with respect to the normal to the surface. The assumed refractive index of silver was $n = 0.14 + 6.94i$, and the emitter was a parallel or a perpendicular dipole positioned in the middle of the membrane and oscillating at the wavelength of $986nm$ or $930nm$. The calculated external efficiencies corresponding to perpendicular dipoles are negligible, while the external efficiencies of parallel dipoles are shown in Figure 2.9. As a reference, for the unprocessed semiconductor wafer and dipoles positioned $45nm$ from the semiconductor/air interface, we calculate that η_{ext} is 2% into the 90^o collection angle, or 0.5% into the 30^o collection angle, both at wavelength of $986nm$ and $930nm$. η_{ext} for perpendicular dipoles is negligible.

Let us compare these results with the band diagram discussion in the previous section. In normalized units, $986nm$ corresponds to $\frac{\lambda_p}{\lambda} = 0.14$ and $930nm$ corresponds to $\frac{\lambda_p}{\lambda} = 0.15$. From the band diagram shown in Figure 2.4 it follows that dipoles oscillating at these wavelengths can couple to TE_0 and TM_0 modes in the gradual cutoff, or to the TM_{-1} mode. From the field profiles of these modes, we know that parallel dipoles couple mostly to TE_0 or TM_0, while perpendicular dipoles couple to the TM_{-1} mode. This TM_{-1} mode is completely below the light line in air. Therefore, all the radiation coupled to it remains trapped within the structure. For that reason, the calculated external efficiency of perpendicular dipoles is negligible. On the other hand, the cutoff of TE_0 and TM_0 modes lies above the light line in air. Therefore, TE_0 and TM_0 modes can be extracted outside the structure, in a range of k_x vectors for which these bands lie within the light cone. However, the fact that a mode is above the light line does not automatically mean that it leaks into air very strongly. The field intensity of TE_0 and TM_0 modes is strongly damped in their passage through the metal layer on top. For that reason, the achievable extraction efficiencies cannot exceed 13% into the 90^o collection angle, when the silver layer is $40nm$ thick (as shown in Figure 2.9).

Another interesting question arising from Figure 2.9 is why the decay rate enhancement and external efficiency peak at some metal thickness, for parallel dipoles. This can be also

explained with the help of the band diagram shown in Figure 2.4. Parallel dipoles couple mostly to TE_0 or TM_0 modes. F_d is maximum when the electric field at the position of the dipole is maximized, which happens around cutoff. As the thickness of the top silver layer increases, the penetration tails of the TE_0 or TM_0 wave into that layer decrease, meaning that their cutoff frequency increases. Therefore, we can expect that more silver on top should be added in order to achieve a cutoff at $930nm$, instead of $986nm$. For that reason, the F_d peak shifts to larger silver thickness when dipole oscillates at $930nm$ (instead of $986nm$), as shown in Figure 2.8. If we let the parallel dipole oscillate at $986nm$ and the top silver layer thickness is kept at $12nm$, and we keep adding more silver on top of the structure, the TE_0 mode cutoff shifts towards higher frequencies, the coupling of dipole to it starts to drop and F_d decreases as well. On the other hand, if we reduce the silver layer thickness to below $12nm$, the dipole will still couple to TE_0 and TM_0 modes, but above their cutoff, where the electric field intensity is not maximized in the middle of the slab. Therefore, F_d drops again. What about the perpendicular dipole? The decay rate enhancement reaches the value of 3 when the silver layer is $10nm$ thick and saturates there. This is due to the fact that the TM_{-1} mode does not have a cutoff and the field intensity of the ASP mode does not vary significantly throughout the membrane. There is a drop in F_d for a silver layer thinner than $10nm$. As we remove silver from top, we cannot excite the coupled SP state (ASP) anymore. Instead, we can excite only the SP mode of the bottom metal-semiconductor interface. The field intensity achievable in the middle of the slab will be approximately 2 times weaker than for the coupled state, and F_d will be two times smaller than its maximum value for the ASP state.

Two questions have to be answered in order to estimate η_{ext} in this structure: is the band that a dipole couples to above the light line, and what is the transmission of light through the semitransparent silver layer on top. From the band diagram shown in Figure 2.4, it follows that if a parallel dipole operates below or much above the cutoff for TE_0 and TM_0 modes, its radiation cannot be coupled to the outside world. Also, if the top silver layer is too thick, the radiation will be strongly damped by absorption in it. Therefore, η_{ext} has to decrease on both sides of the peak, as shown in Figure 2.9.

2.6 Periodic metallic structures

The external efficiencies calculated in the previous section are quite modest. Furthermore, the emission from the analyzed structures is not directional, as can be seen from Figure 2.9: less than 50% of the total emission outside the structure is within the 30^o collection angle. In order to improve both the extraction efficiency and the directionality of emission, we will now explore metallic photonic crystals. By periodically modulating a semitransparent silver layer, we will be able to modify the band diagram shown in Figure 2.4 and bring previously nonradiative bands above the light line. The band diagram will be folded back into its first Brillouin zone at the edges of which the bandgap for surface plasmon waves will appear.[71] This means that bands previously located below the light line can now be brought above it. However, a reduction in the amount of metal on top will influence a decrease in F_d. For complicated geometries obtained after the top metal layer patterning, it is possible to use the FDTD-based 3D analysis of the Purcell factor proposed in Reference 47. Unfortunately, this requires large amounts of computer memory. Instead, it can be roughly estimated that the decay rate enhancements and Purcell factors of patterned structures have values between those of the structures with and without metal on top (i.e., they can be approximated by spatial averaging of F_d for structures with and without metal on top). Therefore, we will trade off some of the decay rate enhancement for being able to extract light outside the structure with top mirror patterning.

2.6.1 Analyzing metallic photonic crystals in the old fashioned way

The old-fashioned way of explaining the effect of a grating (i.e., a 1D photonic crystal) is shown in Figure 2.10. Both momentum and energy conservation have to be satisfied on a grating. Energy conservation is converted to frequency conservation, i.e., the frequency of the emitted photon has to be equal to the frequency of the surface plasmon. On the other hand, momentum conservation requires that the parallel components of wavevectors of the

outcoupled photon and the surface plasmon differ by a reciprocal lattice vector:

$$k_{sp} + \Delta k = k_{out} sin(\theta) \tag{2.26}$$

$$\Delta k = n\frac{2\pi}{a}, n = 0, \pm 1, \pm 2, ... \tag{2.27}$$

where k_{sp} is the x component of the SP wavevector, k_{out} is the wavevector of the outcoupled photon (in the x-y plane), θ is the angle of photon emission (measured with respect to the y axis) and a is the grating period. It is assumed that the SP has no wavevector component in the z direction and, therefore (according to the momentum conservation), the outcoupled photon cannot have a wavevector component in the z direction.

The wavevectors of the SP (excited at the metal-semiconductor interface) and the outcoupled photon can be expressed as

$$k_{sp} = \frac{2\pi}{\lambda}\sqrt{\frac{\epsilon_1 \epsilon_2}{\epsilon_1 + \epsilon_2}} \tag{2.28}$$

$$k_{out} = \frac{2\pi}{\lambda}, \tag{2.29}$$

where λ is the wavelength measured in air and ϵ_1 and ϵ_2 are the dielectric constants of the semiconductor and metal, respectively. The absorption in metal is neglected, i.e., ϵ_2 is assumed to be real. ϵ_2 can be expressed from the Drude or Lorentz model (equations 2.11 and 2.12). Therefore, at some wavelength λ we can choose a grating periodicity a in such a way that the photon is coupled outside the structure, i.e., (ω, k_x) is selected to be at a point of the dispersion diagram above the light line in air (as shown in Figure 2.10). It has to be emphasized that this approach is approximate. It assumes that bands folded back with the help of a grating preserve their original shape. In reality, this is not true and, for that reason, the exact analysis presented in the next subsection is necessary. However, the approximate grating analysis gives us a good starting point in designing a metallic photonic crystal. Furthermore, the approach is easily extendable to structures periodic in 2D.

However, the periodicity of a grating is not the only issue that matters. The extraction efficiency is also determined by the n-th order Fourier coefficient of the grating, where $\Delta k = n\frac{2\pi}{a}$ (i.e., the coupling happens through the reciprocal lattice vector of the n-th order and the dispersion diagram is folded n times). This can be explained in terms of the

standard diffraction grating analysis.[76] In the far field (the region of Fraunhofer diffraction), the field magnitude is proportional to the Fourier transform of the aperture (the grating in this case). Since the grating of our interest is periodic, it can be expressed in terms of the Fourier series:

$$t(x) = \sum_{n=-\infty}^{n=+\infty} c_n e^{i\frac{2\pi}{a}nx}, \tag{2.30}$$

where $t(x)$ refers to the amplitude transmittance as a function of position. The Fourier

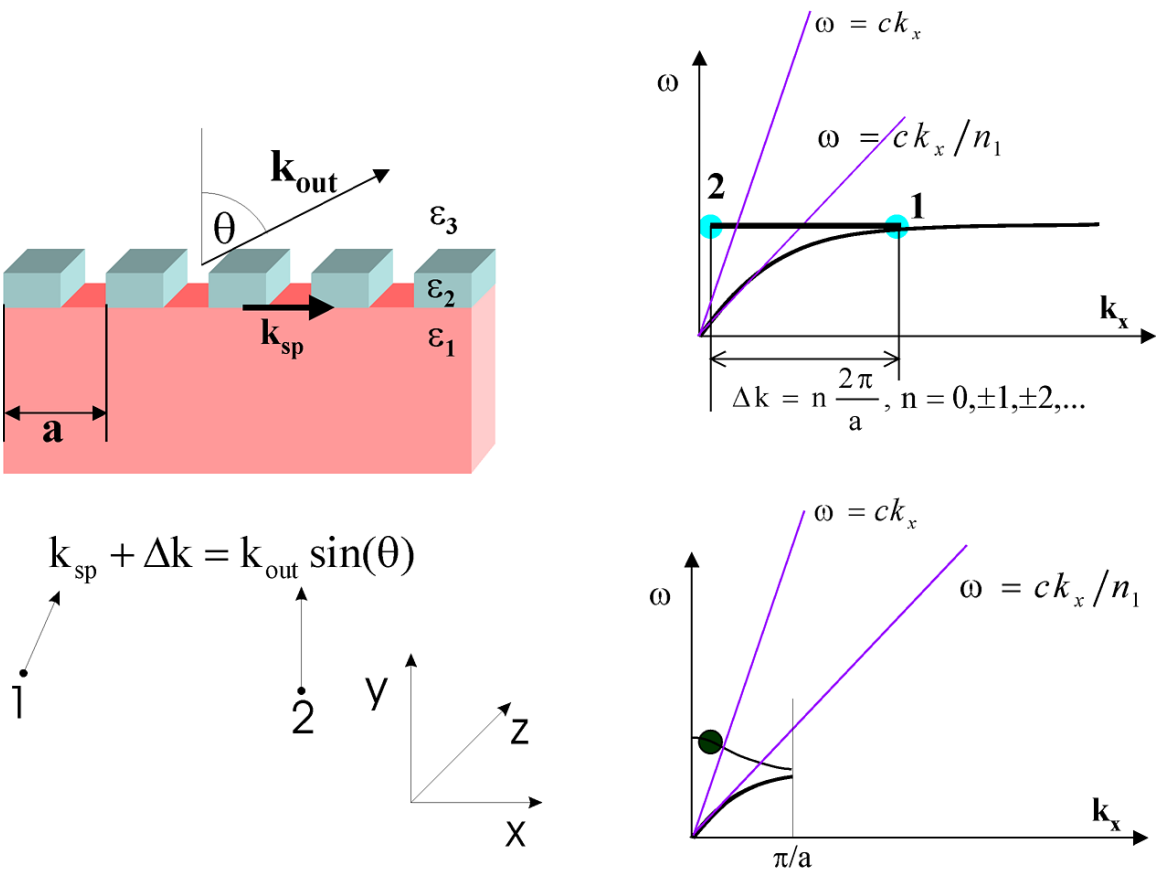

Figure 2.10: Outcoupling of the SP mode through the grating.

transform of this grating is

$$T(k) = \sum_{n=-\infty}^{n=+\infty} c_n \delta(k - \frac{2\pi n}{a}) \tag{2.31}$$

The magnitude of the far field is proportional to $T(k)$. Since the field intensity is proportional to square of the field magnitude, it follows that the intensity of the n-th diffracted component is proportional to $|c_n|^2$. Let us now find $|c_n|^2$ for our grating shown in Figure 2.10. By modulating the metallic surface periodically, we also modulate the amplitude transmittance as a function of position x. Let s denote the gap between two metallic stripes (the width of the region where the thickness of the metal film is decreased), and let t_1 and t_2 denote transmission through the metal film of the decreased thickness (region of width s), and the metal film of the original thickness (region of width $a-s$), respectively. Then we have

$$c_n = \frac{1}{a}\int_0^a t(x)e^{-i\frac{2\pi}{a}nx}dx \tag{2.32}$$

$$= \frac{1}{\pi n}(t_1 - t_2)e^{-i\frac{\pi}{a}ns}\sin\left(\frac{\pi ns}{a}\right), n \neq 0 \tag{2.33}$$

$$c_0 = \frac{1}{a}\int_0^a t(x)dx = \frac{s}{a}t_1 + \frac{a-s}{a}t_2 \tag{2.34}$$

The diffraction efficiency of the n-th order is defined as $\eta_n = |c_n|^2$. Therefore, we have:

$$\eta_0 = \left|\frac{s}{a}t_1 + \frac{a-s}{a}t_2\right|^2 \tag{2.35}$$

$$\eta_n = \frac{|t_1 - t_2|^2}{\pi^2 n^2}\left|\sin\left(\frac{\pi ns}{a}\right)\right|^2, n \neq 0 \tag{2.36}$$

Since the factor $\frac{|t_1-t_2|^2}{\pi^2}$ appears for all $n \neq 0$, we can normalize η_n with it:

$$\eta_n^{(1)} = \frac{1}{n^2}\left|\sin\left(\frac{\pi ns}{a}\right)\right|^2, n \neq 0 \tag{2.37}$$

We should keep in mind that the bigger the contrast in t_1 and t_2 (i.e., the bigger $|t_1 - t_2|^2$), the higher the diffraction efficiencies. For that reason, we will completely remove metal from the region of width s in our gratings.

Let us now try to design gratings that can couple out the radiation from our metal clad semiconductor waveguides, presented in the previous section. The emission from the QW is centered around $986nm$ or $930nm$ (for C-HH and C-LH emission peaks). In this wavelength region, the dielectric constant of silver (ϵ_2) is between -43 and -48.6. For $\epsilon_1 = 12.25$, we have that $k_{sp} = f\frac{2\pi}{\lambda}$, where $f = 4.047$ at $986nm$, and $f = 4.139$ at $930nm$. To achieve the

emission within the 30^o cone ($\theta \leq 30^o$), we have to satisfy the following relation:

$$f\frac{2\pi}{\lambda} + n\frac{2\pi}{a} = \frac{2\pi}{\lambda}\sin(\theta), \tag{2.38}$$

where $0 \leq \sin(\theta) \leq 1/2$. Therefore:

$$0 \leq f + n\frac{\lambda}{a} \leq \frac{1}{2} \tag{2.39}$$

Let us choose a few gratings that satisfy the previous condition. Their parameters are shown in Table 2.1.

a [nm]	n	θ (at 986nm)	θ (at 930nm)	s [nm]	$\eta_n^{(1)}$
250	-1	6^o	25^o	160	0.82
480	-2	3.5^o	15.3^o	160	0.19
650	-3	30^o	9^o	160	0.06
650	-3	30^o	9^o	100	0.11

Table 2.1: Parameters of gratings used for extracting the emission from the metal clad microcavity. a is the grating periodicity, s is the gap between silver stripes, θ is the angle of the outcoupled photon with respect to normal and $\eta_n^{(1)}$ is the normalized diffraction efficiency into the n-th order of a grating. The outcoupling happens through the n-th order of a grating.

From Table 2.1, we conclude that the grating with periodicity of $250nm$ will have the best performance, since it has the largest diffraction efficiency. The grating with periodicity of $650nm$ and a gap between stripes of $s = 160nm$ will have the worst performance, which can be somewhat improved by reducing the gap to $100nm$.

2.6.2 Modern approach to the analysis of metallic photonic crystals

Structures with parameters given in Table 2.1, previously treated using the old fashioned Fourier analysis of a grating and momentum conservation, will now be analyzed using 2D FDTD. The flexibility of the FDTD method allows us to take into account the finite semiconductor core thickness and the modification of the dispersion diagram due to coupling between the SP states of the top and bottom metallic surfaces. The schematic diagram of

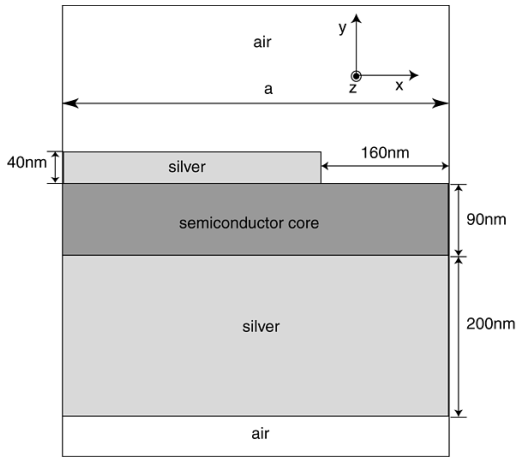

Figure 2.11: The structure with a grating defined in the top semitransparent layer analyzed using the FDTD method in order to study the effect of metal patterning. Mur's absorbing boundary conditions are applied to boundaries in the y direction and Bloch boundary conditions are applied to boundaries in the x direction. a denotes the grating periodicity.

the analyzed structures is shown in Figure 2.11 and the calculated band diagrams for TE and TM polarizations are shown in Figures 2.12, 2.13 and 2.14.

An indicator of how strongly the grating changes the band diagram of an unpatterned structure, and how efficiently this grating can extract the radiation, is the size of the bandgap that opens at the edge of the Brillouin zone. This can be correlated to our explanation of the grating efficiency η_n introduced in the previous subsection. η_n is proportional to the amplitude of the n-th order Fourier coefficient. On the other hand, from the 1st order perturbation analysis of the dispersion diagram, it follows that the n-th order bandgap is also proportional to the amplitude of the appropriate Fourier coefficient. Therefore, the size of the bandgap is directly proportional to the diffraction efficiency of a grating. Let us first consider band diagrams for the TM polarization. Clearly, in the frequency range of interest ($\frac{\lambda_p}{\lambda} \approxeq 0.14$), and with the frequency resolution of $2.3 \cdot 10^{-3} \frac{\lambda_p}{\lambda}$ used in our FDTD calculations, we were able to detect only a bandgap in the dispersion digram of the structure with a periodicity of $250nm$. This means that this structure will have much better performance than the other two analyzed structures in extracting TM polarized light. This result is not surprising and agrees with the grating efficiencies presented in Table 2.1.

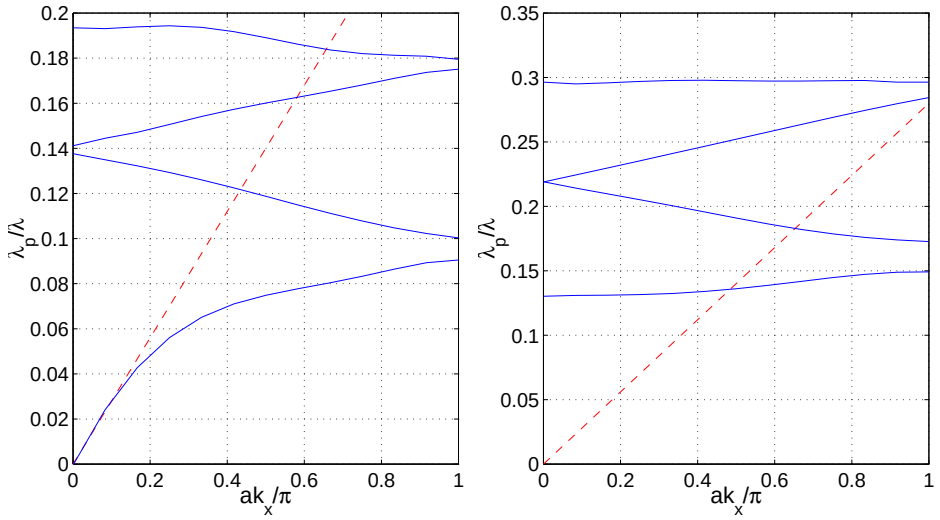

(a) (b)

Figure 2.12: Band diagrams of the patterned structure with a periodicity of $a = 250nm$: (a) TM-polarization; (b) TE-polarization. The dashed line corresponds to the light line in air.

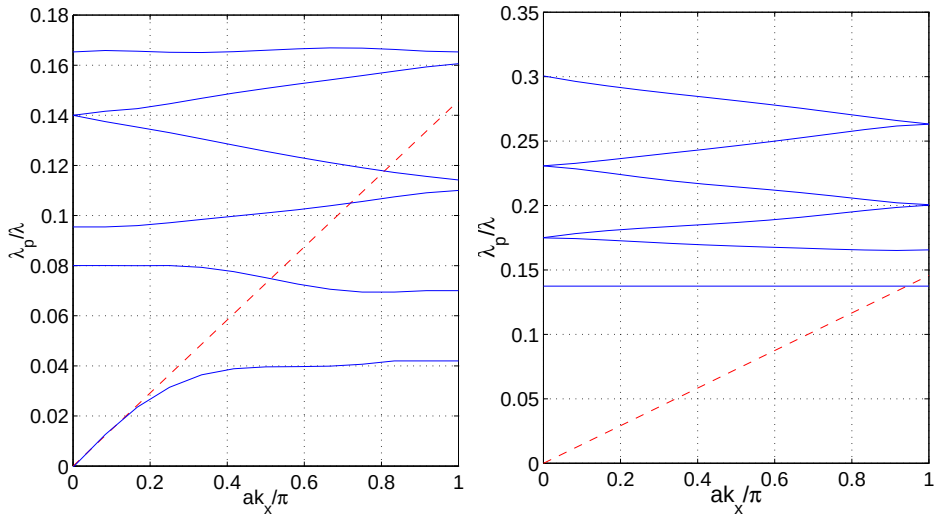

(a) (b)

Figure 2.13: Band diagrams of the patterned structure with a periodicity of $a = 480nm$: (a) TM-polarization; (b) TE-polarization. The dashed line corresponds to the light line in air.

Let us consider the TE polarization next. A band with a cutoff frequency of around 0.14 appears in TE band diagrams for all structures. As we will see from the electric field distribution, this branch corresponds to the combination of the TE_0 mode and the mode that resonates in the gap between silver stripes. For a smaller grating periodicity, gaps between silver stripes are closer to each other and behave as coupled cavities. Therefore, this mode can propagate in the x direction. On the other hand, for the larger grating periodicities (such as $480nm$), cavities are decoupled, this mode cannot propagate and the corresponding TE band is flat. For the upper TE bands, the bandgap does not appear at the edges of the Brillouin zone, meaning that grating has basically no effect there and the corresponding mode is simply the TE mode of the unpatterned structure.

First we filtered the TM polarized fields with $k_x = 0$ and $\frac{\lambda_p}{\lambda} \approxeq 0.14$ for the structure with

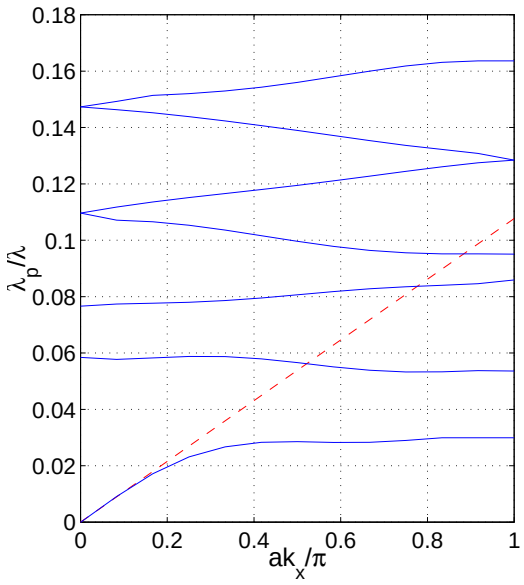

Figure 2.14: Band diagram of the structure with a grating periodicity of $650nm$ (TM-polarization only). The dashed line corresponds to the light line in air.

a periodicity of $250nm$, in order to confirm that this metal layer patterning produces the out-coupling of radiation. From the band diagram shown in Figure 2.12 we see that there are two modes in the filtered frequency range. The x and y components of electric field are shown in Figure 2.15. By comparison with the fields from Figure 2.6, we see that radiation now escapes from the microcavity, even though the gap between silver stripes is smaller

than a wavelength. Moreover, the x component of the electric field is not negligible in the middle of the membrane. This means that parallel dipoles positioned there and oriented in the x direction can also couple to this mode. On the other hand, the E_y field is still strong within the membrane, which means that perpendicular dipoles still strongly couple to this mode.

Then we filtered the TM polarized fields with $k_x = 0$ and $\frac{\lambda_p}{\lambda} \approxeq 0.15$, for the structure

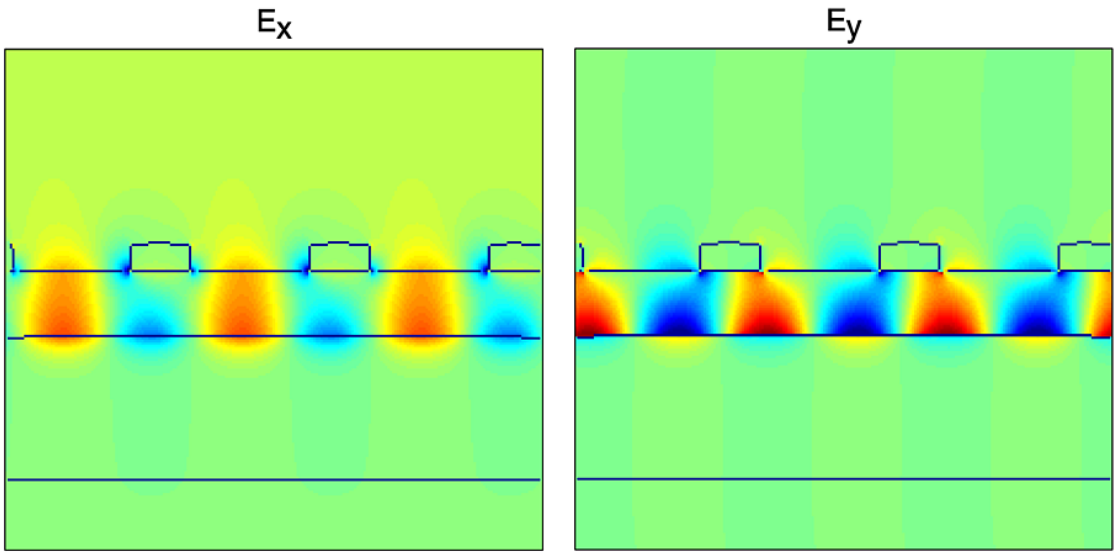

Figure 2.15: Electric field components for the structure with a periodicity of $250nm$. The filtered frequency range was centered at $\frac{\lambda_p}{\lambda} = 0.14$ and $k_x = 0$.

with a periodicity of $650nm$. The electric field components are shown in Figure 2.16. They look exactly like the TM_{-1} mode with $k_x = 6\pi/a$ of the unpatterned structure, except underneath the gaps between silver stripes. The electromagnetic field intensity outside the microcavity is small. This was expected from the band diagram for the TM polarization for this structure, shown in Figure 2.14, since we could not detect the opening of a bandgap in the filtered frequency range. This is also expected from the diffraction efficency of this grating, which is very small, as shown in Table 2.1.

We also filtered the TE polarized fields with $k_x = 0$ and $\frac{\lambda_p}{\lambda} \approxeq 0.14$ for the structures with periodicities of $250nm$ and $480nm$. The corresponding E_z field distributions are shown in Figure 2.17. The mode looks like a TE_0 mode that also resonates in the gap between silver stripes, and is radiated out of the cavity through the spacing between stripes. Since

the density of these spacings is larger for the structure with a periodicity of $250nm$, this mode will extract emission out of the cavity more efficiently. An example of the upper TE band is shown in Figure 2.18. We plot the E_z field component of a mode with $k_x = 0$ and $\omega = 0.23\omega_p$ for the structure with $a = 480nm$. The weak leakage into air for this mode is expected from the band diagram shown in Figure 2.13, since no bandgap appeared at this (ω, k_x) point. This mode looks almost exactly like a TE_0 mode of the unpatterned waveguide, with $k_x = \frac{4\pi}{a}$.

As we mentioned previously, the properties of a grating are also strongly dependent on

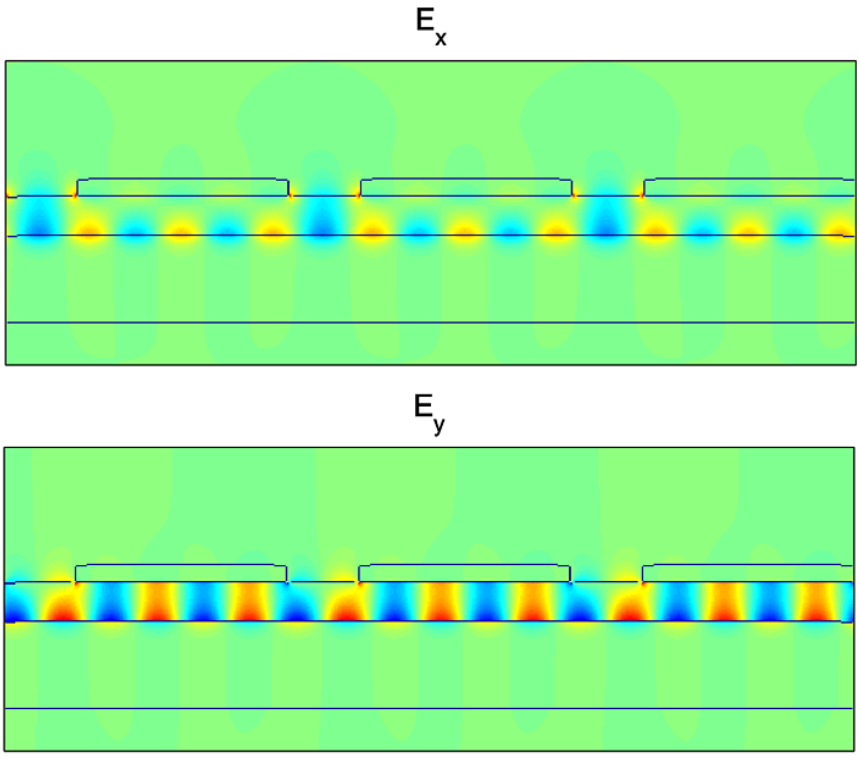

Figure 2.16: Electric field components for the structure with a periodicity of $650nm$. The filtered frequency range was centered at $\frac{\lambda_p}{\lambda} = 0.15$ and $k_x = 0$.

the spacer s between stripes. From the simple Fourier analysis, we predicted that the performance of a grating with $a = 650nm$ would be improved if the gap between stripes was reduced to $100nm$. To prove that this is true, we filtered the same TM mode as the one shown in Figure 2.16, but for a structure where $a = 650nm$ and $s = 100nm$. The result of this calculation is shown in Figure 2.19. Obviously, more light is extracted from this

structure than the one shown in Figure 2.16.

Therefore, patterning of the top metal layer has a strong effect on properties of both TE and TM band diagrams. By choosing a grating appropriately, such as in the case of the analyzed structure with a periodicity of $250nm$, both the emission of perpendicular and parallel dipoles can be extracted out of the microcavity.

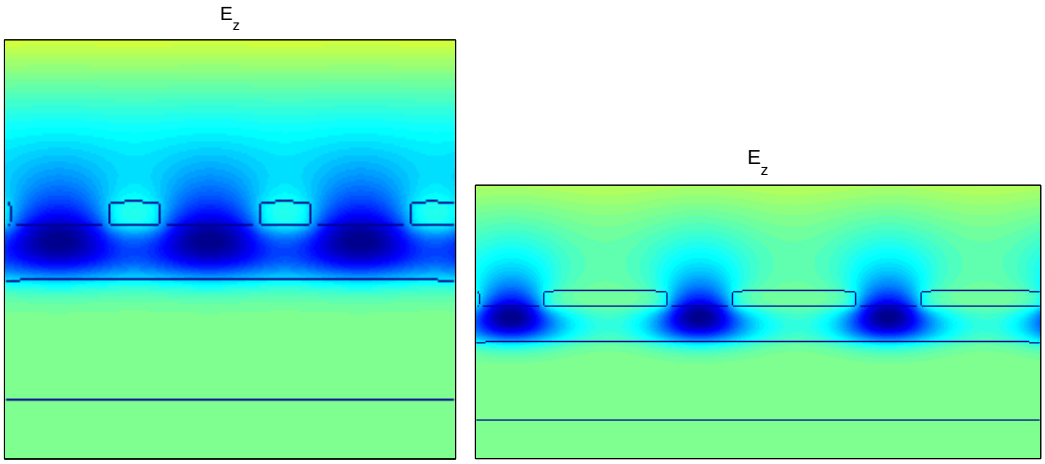

Figure 2.17: E_z of the TE mode with $k_x = 0$ for structures with periodicities of: (a) $250nm$ and (b) $480nm$. $\frac{\lambda_p}{\lambda}$ is equal to 0.13 and 0.137, respectively.

2.6.3 Extraction efficiencies of periodically modulated structures

For structures with a patterned top metal layer, the external efficiencies can be calculated using a 3D FDTD model, with oscillating dipole sources approximating atomic transitions. However, this computation requires large amounts of memory, as we noted previously. Instead, we can easily estimate, from our 2D FDTD simulations, the efficiency of light extraction by coupling to any given mode. The extraction efficiency η_x is the probability that a photon radiated into that mode escapes the cavity. The rate at which the electromagnetic field energy is lost from the cavity is then described by the radiation quality factor Q_r:

$$Q_r = \frac{\omega_0 W}{P_r}, \tag{2.40}$$

where W represents the electromagnetic field energy stored within the cavity, ω_0 is the radial frequency of a mode and P_r is the power radiated outside the cavity. On the other hand, the non-radiative quality factor Q_{nr} describes the rate at which the stored electromagnetic energy decreases due to loss mechanisms other than the radiation outside the cavity:

$$Q_{nr} = \frac{\omega_0 W}{P_{nr}}, \tag{2.41}$$

where P_{nr} represents the power lost through these mechanisms. The total quality factor

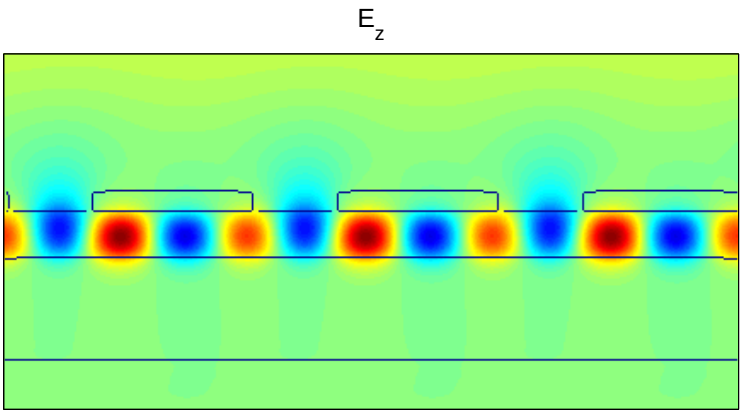

Figure 2.18: E_z of the TE mode with $k_x = 0$ for the structure with periodicity of $480nm$. $\frac{\lambda_p}{\lambda}$ is equal to 0.23.

Q is defined as

$$\frac{1}{Q} = \frac{1}{Q_r} + \frac{1}{Q_{nr}} \tag{2.42}$$

and the radiative and non-radiative photon lifetimes are defined as

$$\tau_{pr} = \frac{Q_r}{\omega_0} \tag{2.43}$$

$$\tau_{pnr} = \frac{Q_{nr}}{\omega_0} \tag{2.44}$$

$$\tag{2.45}$$

η_x can be expressed as

$$\eta_x = \frac{\frac{1}{\tau_{pr}}}{\frac{1}{\tau_{pr}} + \frac{1}{\tau_{pnr}}} = \frac{Q}{Q_r} \tag{2.46}$$

Clearly, η_x does not take into account the dependence on the position and orientation of dipole transitions.

To calculate η_x, we again use the 2D FDTD method. The only non-radiative loss mech-

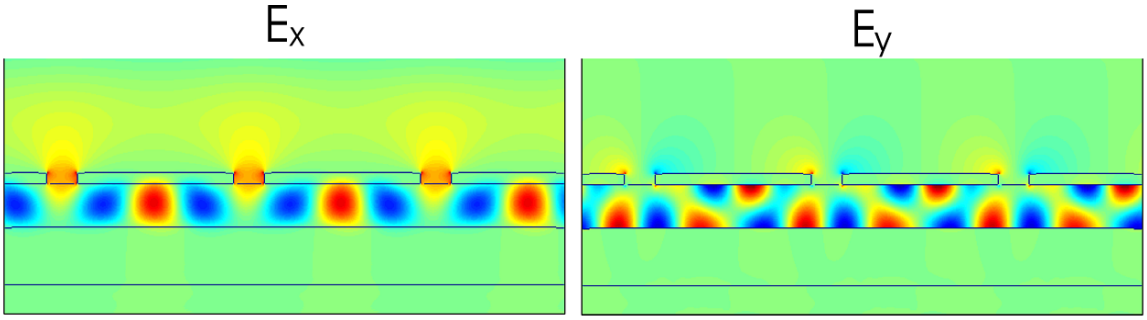

Figure 2.19: The effect of reducing a gap between stripes (to $100nm$) on performance of a grating with $a = 650nm$. For the shown TM mode, $k_x = 0$ and $\lambda_p/\lambda = 0.15$. From comparison with the result shown in Figure 2.16, it is clear that the extraction is improved, as predicted from the Fourier analysis. For the structure shown in this Figure, thickness of a semiconductor core is $150nm$. However, the position of the TM_{-1} (ASP) band (which is folded here) is not strongly dependent on the core thickness, as mentioned previously.

anism is assumed to be the absorption in the metal and the damping constant is set to $\hbar\Gamma = 0.05eV$. It is important to note that the calculated Q factors are approximate, since the combination of absorption losses with Bloch boundary conditions introduces calculation errors, as noted in Appendix I. For the folded TM_{-1} mode in the structure with periodicity of $250nm$, whose field distribution is shown in Figure 2.15, we estimate values for Q_r between 30 and 50, $Q \approxeq 6$ and η_x between 12% and 20%. For the TE mode shown in Figure 2.17, we calculate $Q_r = 15$, $Q = 5$ and $\eta_x = 33\%$. From the band diagram shown in Figure 2.12(a), we can see that the emission in the frequency range from 0.14 to 0.15 (in units of $\frac{\lambda_p}{\lambda}$) emits into a 30^o escape cone, if coupled to TM modes. However, coupling to TE modes does not improve the directionality and the emission goes into the 90^o cone. For the structure with periodicity of $480nm$ and the folded TM_{-1} mode at $k_x = 0$ and $\omega/\omega_p = 0.14$, we estimate that $Q \approxeq 8$ and $\eta_x \approxeq 2\%$. For the first TE band (whose field distribution is

shown in Figure 2.17(b)), we estimate $\eta_x = 20\%$. However, only dipoles located directly underneath the gap between silver stripes can couple to this mode, which implies that the external efficiency is at least three times smaller than the calculated η_x, i.e., around 7%. For the folded TM_{-1} mode in the structure with $a = 650nm$, we estimate that $Q \cong 11$ and $\eta_x \cong 0$. η_x corresponding to the first TE branch is predicted to be around 5% (when including the spatial averaging, i.e., coupling of only dipoles underneath the spacing between stripes to this mode).

The extraction efficiencies corresponding to TM modes, estimated from their Q factors, follow the trend in the calculated diffraction efficiencies presented in Table 2.1. From the calculated extraction efficiencies corresponding to TE modes in the structures with periodicities of 480 nm and $650nm$, we conclude that they will not perform any better than the unpatterned structures, with regards to the extraction of radiation from parallel dipoles (see Figure 2.9). For the extraction of radiation from perpendicular dipoles, the structure with periodicity of $650nm$ will perform almost the same as the unpatterned structure. On the other hand, the structure with periodicity of $480nm$ will show some improvement over the unpatterned structure, but will still perform much worse than the best design with $a = 250nm$.

We conclude that by adding a grating with periodicity of $250nm$ to the metal clad microcavity, an extraction efficiency over 30% can be achieved. The filtered modes have low quality factors and overlap with both C-HH and C-LH emission peaks. From the field patterns for the TM mode shown in Figure 2.15, we see that this mode can extract emission from both perpendicular dipoles and parallel dipoles oriented in the x direction. On the other hand, the filtered TE mode extracts the emission of parallel dipoles oriented in the z direction. Since the dipoles located in the middle of the membrane couple to these modes very efficiently, we expect that this structure will have a better external efficiency than the unpatterned structure. One should also note the low values of Q resulting from the significant metal absorption loss. A reduction in the absorption and a further increase in the extraction can be achieved by designing a device that operates at even longer wavelengths. As we will see later, the calculated Q values are in the same range as our experimental results, and limited by absorption loss.

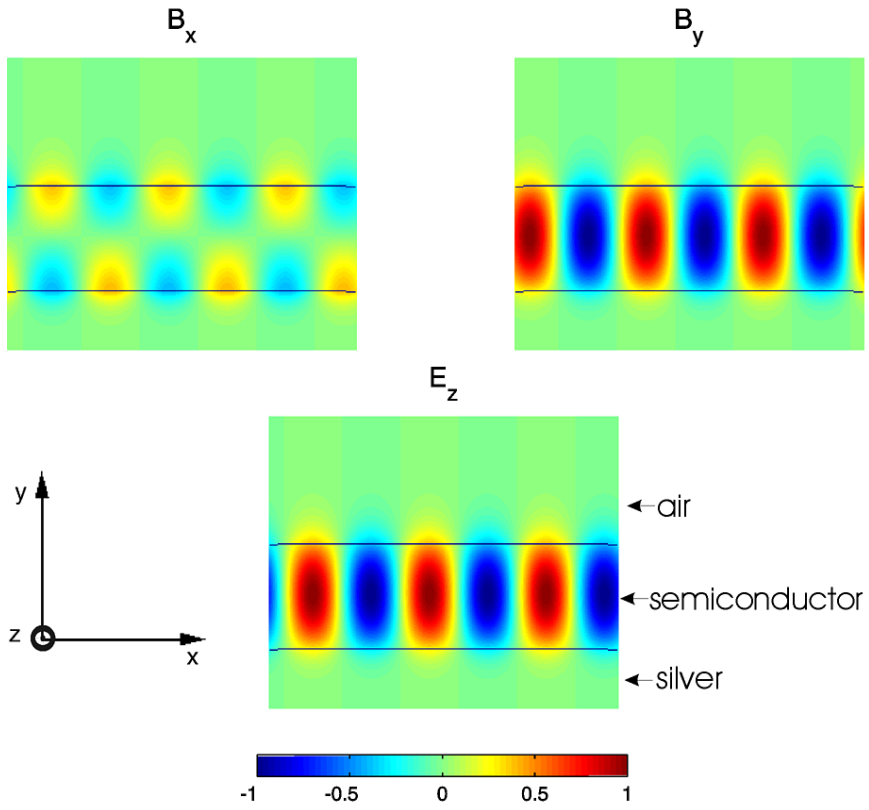

Figure 2.20: TE mode of the half-processed wafer, with $k_x = 0.0628$ and $\omega = 0.435\omega_p$. The semiconductor thickness is $90nm$ and the widths of figures correspond to $300nm$.

2.7 Thin semiconductor film on top of a metal layer

What would happen if, instead of a semiconductor slab between two coupled metallic surfaces, we had only a thin semiconductor membrane sitting on top of a thick metallic surface? From our earlier discussions, it is clear that in this structure we can expect lower values of the decay rate enhancement F_d (compared to the structure with two metallic cladding layers), that the radiation of perpendicular dipoles will strongly couple to the SP mode of the single metal surface and remain trapped there, and that the only mechanism of light extraction will be coupling to leaky waveguide modes. The band structure will be similar to that of a slab waveguide, with the addition of a SP mode of the metal-semiconductor interface. When describing our experimental results, we will refer to this structure as the half-processed wafer. Some of its modes are shown in Figures 2.20 and 2.21.

We have calculated the efficiency ($F_d\eta_{ext}$) of light emission from this structure, using again the method from References 73 and 75. $F_d\eta_{ext}$ (both into the 30^o or 90^o collection angles) as a function of the semiconductor slab thickness, and for parallel dipoles positioned in the middle of the slab, is shown in Figure 2.22. The efficiency corresponding to perpendicular dipoles is negligible.

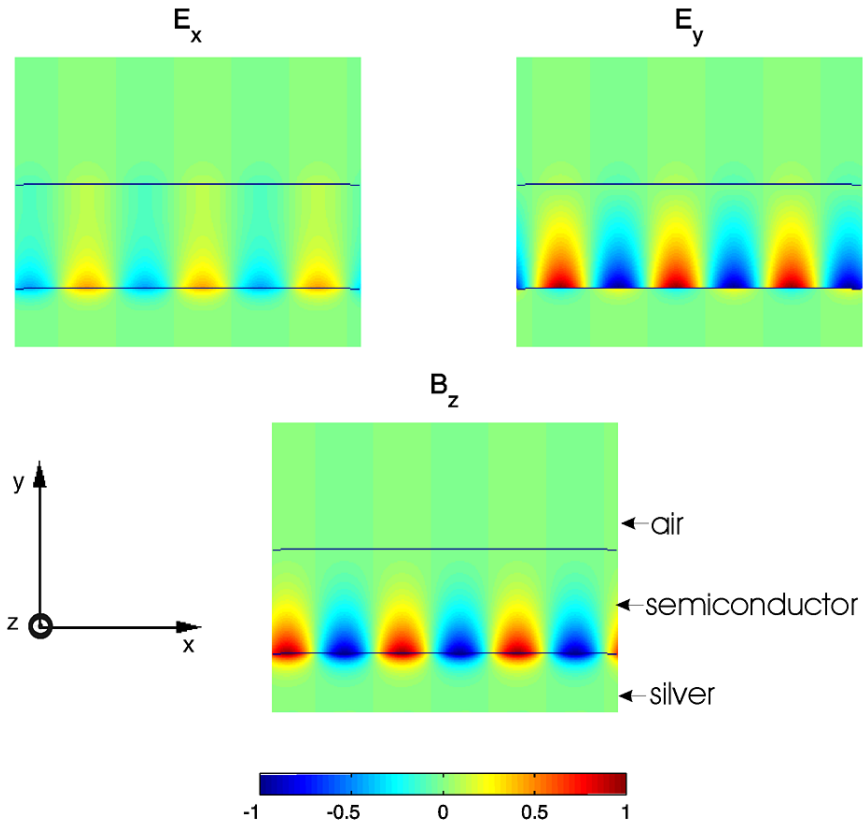

Figure 2.21: TM mode of the half-processed wafer, with $k_x = 0.0628$ and $\omega = 0.3418\omega_p$. The semiconductor thickness is $90nm$ and the widths of figures correspond to $300nm$.

Therefore, for a core thickness of $90nm$, we can expect an efficiency of 6% into the 90^o collection angle, or 1.3% into the 30^o collection angle. By tuning the core thickness, one can improve the efficiency of this structure, but not its directionality.

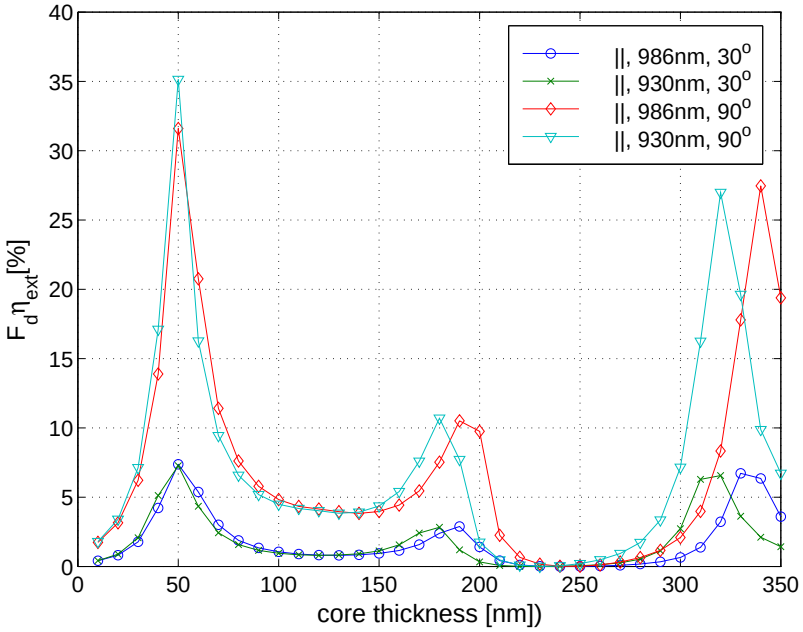

Figure 2.22: The efficiency of the half-processed structure, as a function of the semiconductor core thickness.

2.8 Fabrication

The design of the grown wafer is shown in Table 2.2. This wafer was designed for fabrication of electrically pumped devices and p and n doped layers were already included. Layers 2 to 8 form a membrane that will be lifted off and sandwiched between two metal layers. The total membrane thickness is $88nm$. The main emission peak from the InGaAs/GaAs QW is at $986nm$, corresponding to C-HH transitions. There is also a peak at $930nm$, corresponding to C-LH transitions.

The fabrication procedure is described in Figure 2.23. First we deposit a thick silver mirror ($d > 1.5\mu m$) on top of the grown wafer (step (a)). This metal layer is also used as a mechanical support during the membrane liftoff. Then we remove the membrane from its substrate by dissolving the sacrificial $AlAs$ layer in 8.2% hydrofluoric acid (HF) diluted in water (step (b)). HF attacks $AlAs$ very selectively over $Al_xGa_{1-x}As$ for $x < 0.4$.[55] The lifted-off membrane (layers 2-8) with a thick silver layer on top is then Van der Waals bonded[55] onto a silver coated silicon wafer and the silver on the lift-off film bonds to

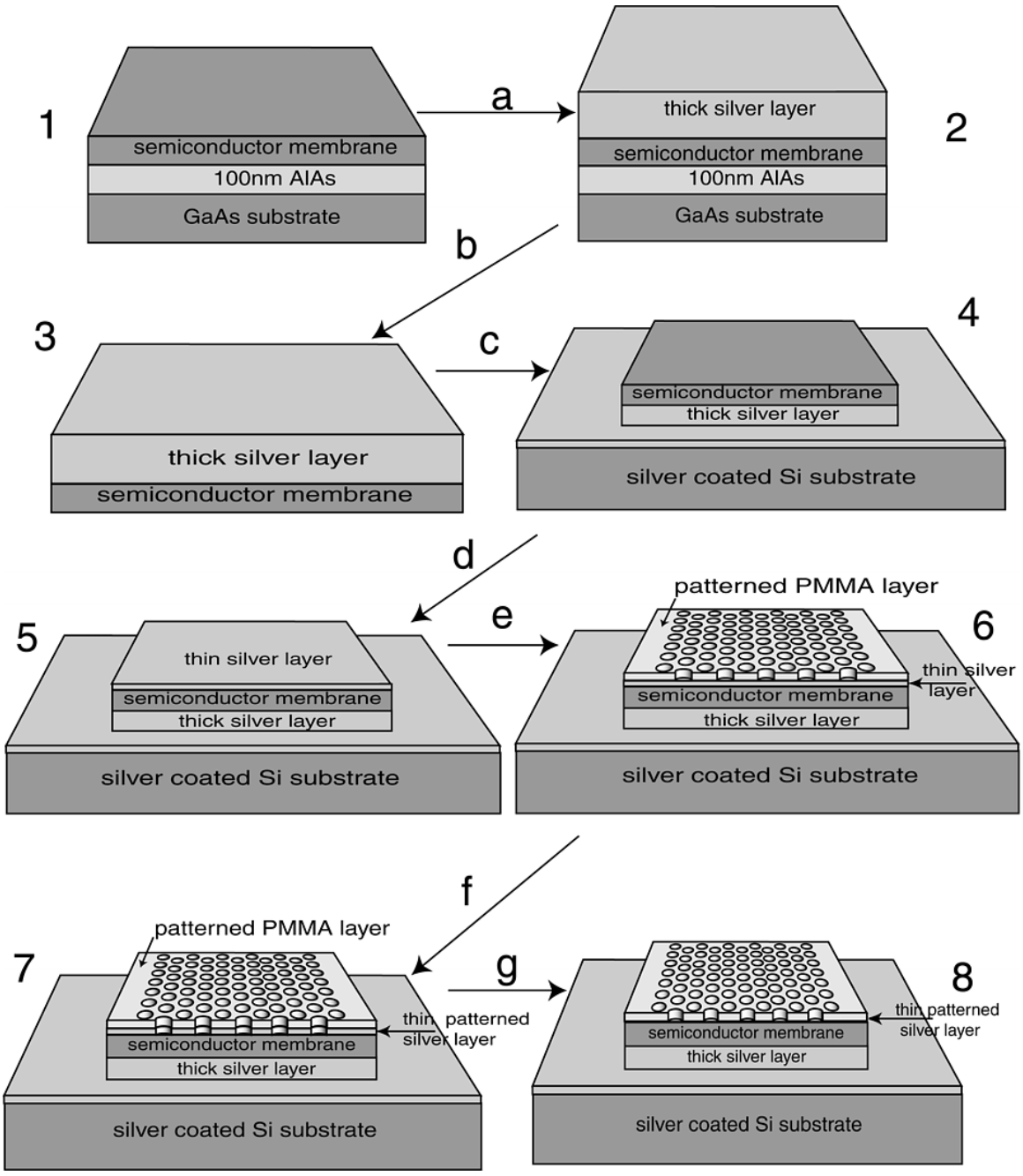

Figure 2.23: Fabrication procedure: a) thick silver layer deposition; b) epitaxial liftoff; c) Van der Waals bonding onto silver coated silicon substrate; d) thin silver layer deposition; e) PMMA deposition and patterning using e-beam lithography; f) pattern transfer to thin silver layer using Ar^+ ion milling; g) PMMA removal.

Table 2.2: Layers of the grown wafer.

	layer	thickness [nm]
8	p-GaAs cap	10
7	p-$Al_xGa_{1-x}As$, $x < 0.3$	20
6	undoped GaAs	10
5	undoped $In_{0.2}Ga_{0.8}As$ QW	8
4	undoped GaAs	10
3	n-$Al_xGa_{1-x}As$, $x < 0.3$	20
2	n-GaAs cap	10
1	undoped AlAs (sacrificial layer)	100
0	undoped GaAs substrate	-

the silver coated on the silicon support wafer (step (c)). Another $20nm$ to $40nm$ thick silver layer is then deposited on top of the n-GaAs cap (step (d)). $100nm$ thick PMMA (polymethylmethacrylate), with molecular weight of 950K, is then spun on top of the thin metal layer and subsequently baked on a hot plate at 150^oC for 20 minutes. A desired pattern is beamwritten on the PMMA by electron beam lithography in a Hitachi S-4500 electron microscope (step (e)). The resulting patterns are approximately $50\mu m \times 50\mu m$ in size, and the exposed PMMA is developed in a 3:7 solution of 2-ethoxyethanol:methanol for 30 seconds. Then, the pattern is transferred into the top semitransparent metal layer by using Ar^+ ion milling at a beam voltage of 1500V (step (f)). Finally, the remaining PMMA may be dissolved in acetone (step (g)). Corresponding SEM pictures showing the top views of fully processed wafers are given in Figure 2.24, where lighter areas correspond to regions where silver was removed.

The structure shown in Figure 2.23.1 is the unprocessed wafer and the one in Figure 2.23.4 is referred to as the half-processed wafer. Figure 2.23.5 represents the unpatterned metal clad microcavity and, finally, the structure shown in Figure 2.23.8 is the fully processed one.

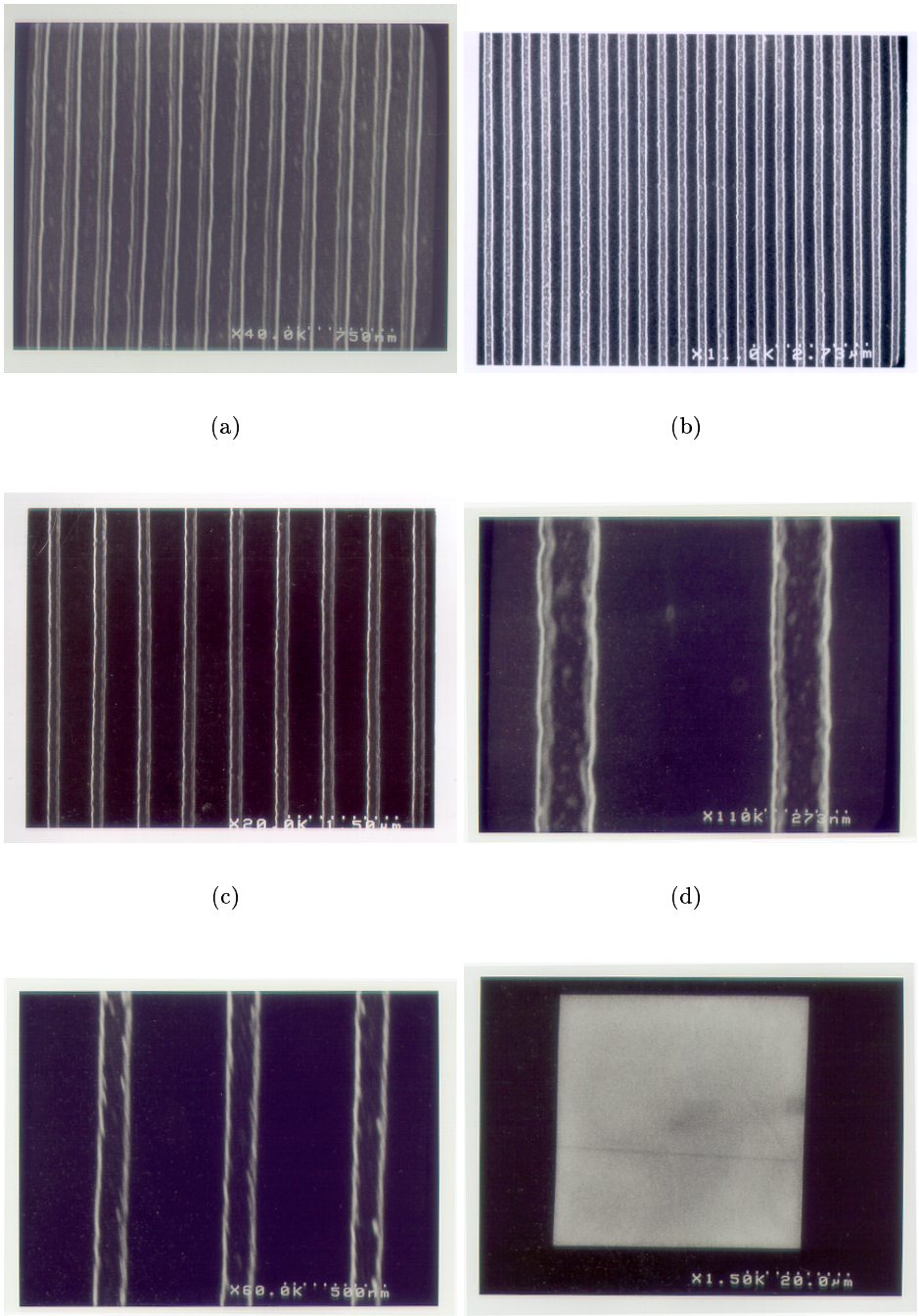

(a) (b)

(c) (d)

(e) (f)

Figure 2.24: Fabricated patterns in the top silver layer. Light areas correspond to regions where silver was removed during the Ar^+ ion milling process. Fabricated structures have various periodicities: (a) $250nm$; (b) $480nm$; (c) $650nm$; (d) 650nm (zoom in); (e) 650nm (zoom in); (f) whole array. For all structures, the gap between silver stripes is around $160nm$.

2.9 Experimental results

2.9.1 Measurement setup

The experimental setup used for the photoluminescence (PL) measurements is shown in Figure 2.25. Samples are mounted on an X-Y-Z stage and optically pumped at a 90^o incident angle. The pump source is a semiconductor laser diode emitting at $830nm$, pulsed with a period of $3\mu s$ and a pulse width of $2.5\mu s$. A non-polarizing cube beamsplitter is used to bring 50% of the pump beam to the detector and to measure the external pump power. The other 50% of the beam is focused to a spot on the sample by using a 100X objective lens (labeled as Lens1). The same objective lens is also used to collect the emitted light. The collection angle is 30^o with respect to normal. The collected emission is then focused in Lens2 and detected using a fiber coupled spectrum analyzer.

Table 2.3: The photoluminescence measured from the fabricated structures. a is the 1D grating periodicity, and s denotes the gap between silver stripes. $E_{up}(986nm)$ and $E_{hp}(986nm)$ denote photoluminescence (PL) enhancements at $986nm$ of the fully processed wafer with respect to the unprocessed and to the half-processed wafer, respectively. $E_{hp}(930nm)$ is the PL enhancement at $930nm$, with respect to the half-processed wafer. The last row corresponds to the structure with unpatterned top metal layer. The half-processed structure has $E_{up}(986nm) = 21$.

a [nm]	s [nm]	$E_{up}(986nm)$	$E_{hp}(986nm)$	$E_{hp}(930nm)$
250	160	46	2.24	5.5
480	160	5.6	0.27	1.8
650	160	6.4	0.3	1.2
0	0	5.5	0.26	1.5

2.9.2 Results of PL measurements

We measured the output from the unprocessed as-grown wafer, from the half-processed wafer, and from the fully processed structures, with patterned or unpatterned thin metal layers on top. Previously theoretically analyzed gratings were fabricated in the top metal layer, which was $25nm$ thick (within a $\pm 10\%$ range). A small reduction in the thickness of

top silver layer helps to improve the pump beam transmission, but does not influence the performance of the patterned structures significantly.

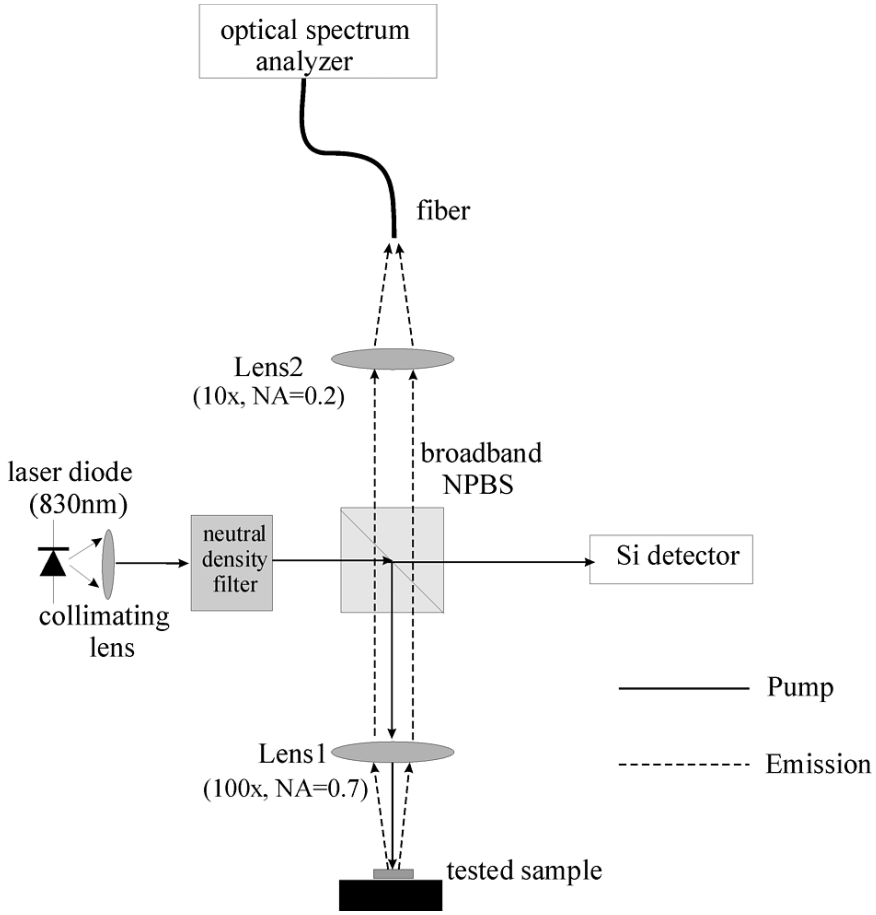

Figure 2.25: The experimental setup used for photoluminescence measurements.

Each grating is characterized with a periodicity (a) and a gap (s) between silver stripes. Between stripes, silver was completely removed by Ar^+ ion milling. During the thin silver layer deposition, part of the sample surface was masked, in order to produce half-processed regions. The measurement results are summarized in Table 2.3, where the peak external pump power was $2.2mW$. For all fully processed wafers, including the unpatterned metal clad microcavity, a FWHM is in the range of $60nm$ to $110nm$. Therefore, their quality factors are between 10 and 15. For the half-processed wafer, a FWHM is $32nm$. Because of a bulk emission tail at lower wavelengths, a luminescence peak at $930nm$ for unprocessed wafers cannot be clearly resolved. The spectra of unprocessed, half-processed and

fully processed wafers are shown in Figure 2.26. The PL peak of the unprocessed wafer at $986nm$ was normalized to 1. A $GaAs$ filter was applied in front of the detector to cut off wavelengths below $890nm$.

As expected from our theoretical discussions in the previous sections, structures with periodicities of $650nm$ and $480nm$ have emission properties very similar to those of the unpatterned structure. The structure with periodicity of $480nm$ shows some improvement at $930nm$, due to the better extraction of energy of perpendicular dipoles. On the other hand, the structure with periodicity of $250nm$ has the best performance, as predicted.

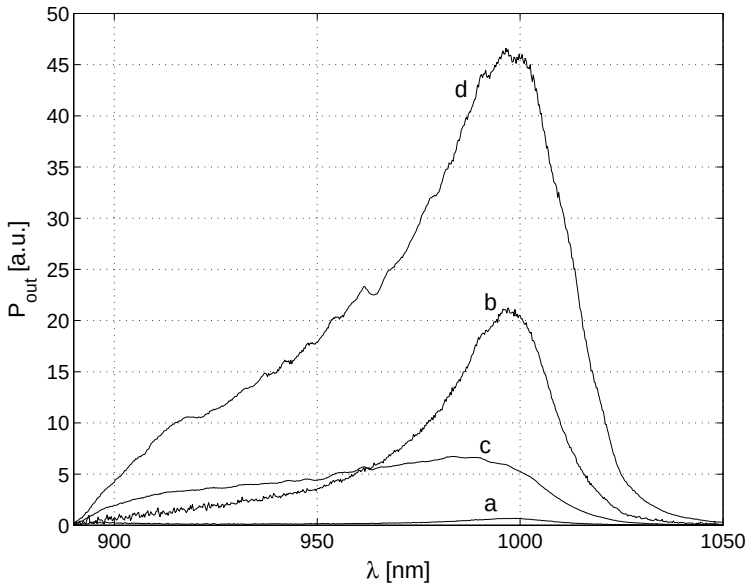

Figure 2.26: The measured photoluminescence spectra: (a) unprocessed wafer; (b) half-processed wafer; (c) pattern with $a = 480nm$ and $s = 160nm$ (the unpatterned structure and the pattern with $a = 650nm$ and $s = 160nm$ give very similar signals); (d) pattern with $a = 250nm$ and $s = 160nm$.

2.9.3 Theory vs. experiment

In order to explain measurement results and confirm that they match our theoretical predictions, we have to take into account several effects: (A) the increase in the pumping intensity resulting from the trapping of pump photons within a microcavity; (B) the decay rate enhancement and (C) the change in the external efficiency. The spontaneous emission

reabsorption is not very efficient because of the small optical confinement factor in the QW, and the photon recycling effect can be neglected.[59]

If P_{in} denotes the external pump power and P_{out} denotes the power emitted from the device, then (in the linear region of the LL curve)

$$\frac{P_{out}}{P_{in}} \approxeq \gamma, \tag{2.47}$$

where γ is defined as

$$\gamma = \beta \cdot (f_{||} F_{d,||} \eta_{ext,||} + f_{\perp} F_{d,\perp} \eta_{ext,\perp}) \tag{2.48}$$

For patterned structures, the first term should be separated into contributions of parallel dipoles in the x direction and in the z direction, since they have different η_{ext}. $f_{||}$ and $f_{\perp}$ are fractions of dipole transitions that are in the QW plane or perpendicular to it. Their values at the main peak of $986nm$ are $f_{||} = 1$ and $f_{\perp} = 0$ and at $930nm$ are $f_{||} = 1/3$ and $f_{\perp} = 2/3$. Furthermore, $1/2$ of parallel dipoles are oriented in the x direction and the other half in the z direction. β is the equivalent pumping intensity that can be expressed as

$$\beta = T_p \cdot N, \tag{2.49}$$

where T_p is the pump power transmission through the top surface, and N is the factor that measures the increase in pumping intensity resulting from the trapping of pump photons within a structure.

Let us label the half-processed wafer by a subscript hp, the unprocessed wafer using a subscript up and denote the photoluminescence (PL) enhancement by E. If the input pump powers are the same (i.e., P_{in} equal), PL enhancements can be expressed as

$$E_{hp} = \frac{\gamma}{\gamma_{hp}} \tag{2.50}$$

$$E_{up} = \frac{\gamma}{\gamma_{up}} \tag{2.51}$$

Pump power transmission through the top surface

In our experiments, structures are optically pumped from top using a semiconductor laser diode emitting at $830nm$. Therefore, it is important to determine what percentage of the vertically incident pump beam is transmitted into the structure. Let us denote by T_p the pump power transmission through the top surface. T_p can be evaluated from Fresnel equations for an unpatterned top layer. The calculated T_p, as a function of the silver layer thickness, is shown in Figure 2.27. The transmission through the air/semiconductor interface is equal to 70%.

Moreover, for both patterned and unpatterned structures, T_p can be determined from

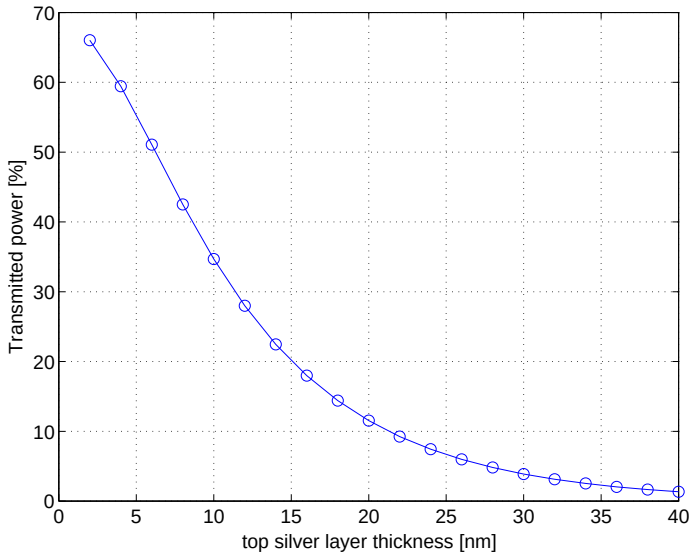

Figure 2.27: The percentage of the vertically incident pump beam intensity transmitted through the top, unpatterned silver layer, as function of its thickness.

diffraction efficiencies presented in Subsection 2.6.1. Let $t(x)$ denotes the amplitude transmittance of a structure as a function of position, and $T(k)$ the Fourier transform of $t(x)$. The magnitude of the transmitted beam will be proportional $|T(k)|$, and the power will be proportional to $n_1|T(k)|^2$, where n_1 represents the refractive index of semiconductor (equal to 3.5). Therefore, T_p will be proportional to diffraction efficiency η_n multiplied by n_1. Diffraction efficiencies are given by equation 2.36. Let t_1 and t_2 represent the amplitude transmittances (into the semiconductor) of the wave incoming from the air region, and

passing through the $0nm$ thick or $25nm$ thick metal layer, respectively. The calculated amplitude transmittance for the vertically incident beam, as a function of the metal layer thickness, is shown in Figure 2.28. It is easy to check that even when the angle of incidence varies between 0^o and 30^o, and the polarization switches between s and p in this range, the amplitude transmittance remains approximately the same. Therefore, we can approximate t_1 and t_2 with their values for the vertically incident beam, and $0nm$ or $25nm$ thick silver on top respectively, i.e., $t_1 = 0.4444$ and $t_2 = 0.0911 - 0.1037i$.

For unpatterned structures, the amplitude transmittance as a function of position is given

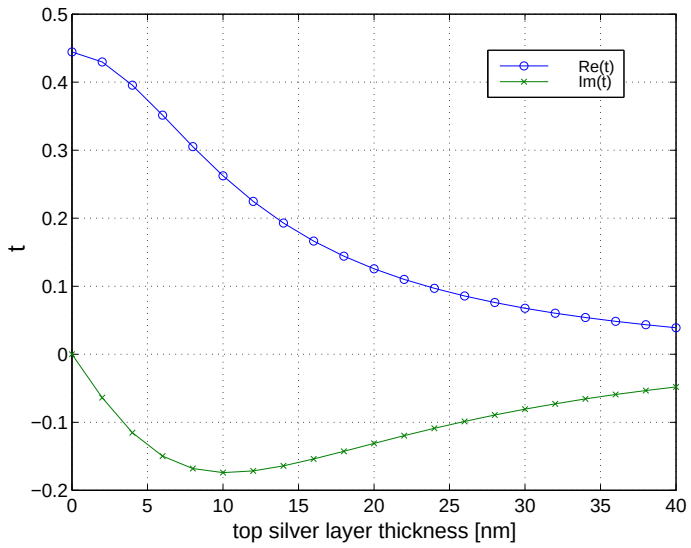

Figure 2.28: Amplitude transmittance of the vertically incident pump beam, as a function of the top metal layer thickness.

by $t(x) = t_2$, or for half-processed and unprocessed structures by $t(x) = t_1$. Therefore, the Fourier transform of the amplitude transmittance is $T(k) = t_i\delta(k)$, for $i = 1, 2$. The magnitude of the transmitted wave is proportional to $|T(k)|$ (i.e., $|t_i|$), and T_p is equal to $n_1|t_i|^2$, where $n_1 = 3.5$. In order to calculate the power transmission T_p for patterned structures, we have to find the diffraction order n at the pump frequency ($\lambda_p/\lambda = 0.17$). From band diagrams of these structures, it is clear that TM polarized light can possibly couple only to higher order TM bands. Since the diffraction efficiency is inversely proportional to diffraction order (n), and since the pump beam is predominantly s polarized and verticaly incident, it follows that we can neglect the coupling of the pump beam to TM modes. On

the other hand, from the band diagram shown in Figure 2.4, it is clear that the pump beam can couple to TE modes of structures, through the diffraction order $n = 0$. Calculated pump beam power transmissions T_p for all structures are shown in Table 2.4.

In order to prove that previously calculated T_p are correct, we have also analyzed the power transmission using the FDTD method. One unit cell of the structure was analyzed, Mur's ABC were applied to boundaries in the y direction and periodic BC (i.e., Bloch BC with $k_x = 0$) to boundaries in the x direction. A parallel dipole (oriented in the x or z direction) was located $400nm$ above the metal surface, in the air and above the middle of the gap between stripes. The frequency of dipole oscillations matched the pump frequency. We calculated the power of the dipole source, as well as the power transmitted into the semiconductor, by integrating the Poynting's vector along a chosen surface. Without metal on top, the calculated transmission was $T_p = 0.7$ for both x-oriented or z oriented dipole, as expected from Fresnel equations. However, in the presence of the metallic grating with periodicity of $250nm$, we calculated $T_p = 0.5$ for an x-oriented dipole and $T_p = 0.24$ for a z-oriented dipole. This means that the average transmission in the presence of a grating is $T_p = 0.375$, which is very close to the value $T_p = 0.357$ from Table 2.4.

Table 2.4: Theoretically estimated pump power transmissions (T_p) to analyzed structures.

structure type	T_p
unprocessed	0.7
half-processed	0.7
unpatterned	0.067
$a = 250nm$, $s = 160nm$	0.357
$a = 480nm$, $s = 160nm$	0.17
$a = 650nm$, $s = 160nm$	0.13

Trapping of pump photons within a structure

The trapping of pump photons within a structure effectively increases the pumping intensity, since the probability that a photon excites an electron transition is proportional to the number of times that it crosses the QW. We can define N as a factor that measures the increase in the pumping intensity resulting from this effect. The unprocessed wafer has

$N = 1$, since there is no mode within the structure that pump photons can couple to and photons not absorbed in the QW are lost when they reach the GaAs substrate. However, in the case of half-processed or fully processed wafers, the pump power transmitted through the top surface can couple to an s-polarized guided mode of the structure, as we discussed in the previous subsection. For fully processed wafers, this can be easily seen from the previously calculated TE band diagrams. For the half-processed wafer, we performed the 1D finite-difference analysis and showed that an s-polarized guided mode existed at the wavelength of $830nm$.

Let us denote by α (in units [1/cm]) the loss coefficient for the guided mode that pump

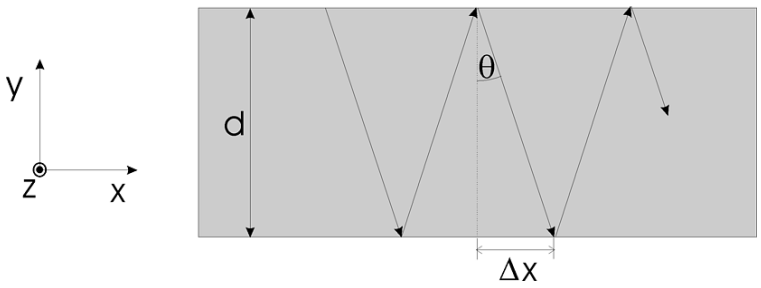

Figure 2.29: Pump power coupled to the mode of the structure.

photons couple to. The angle with respect to the y axis of this mode's total internal reflection (see Figure 2.29) is defined as

$$\theta = \arcsin\left(\frac{k_x}{k}\right), \tag{2.52}$$

where k_x is the wavevector component in the direction of propagation (x) and k is the amplitude of the wavevector. The intensity of the wave varies in the direction of propagation (x) as $e^{-2\alpha x}$. The distance between two consecutive reflections (denoted as Δx) is equal to $d\tan(\theta)$, where d is a membrane thickness. Along the distance Δx, the trapped beam crosses the QW once and a portion of it gets absorbed by the QW. Larger portion of the beam is lost due to nonradiative absorption losses both in a semiconductor and metal. Therefore, the trapped pump beam crosses the QW multiple times, but its intensity decreases in each pass. The total increase in the pumping intensity, with respect to the unprocessed wafer,

is proportional to the factor N defined as

$$N = 1 + e^{-2\alpha\Delta x} + e^{-4\alpha\Delta x} + e^{-6\alpha\Delta x} + ... \tag{2.53}$$

$$= \frac{1}{1 - e^{-2\alpha\Delta x}} \tag{2.54}$$

Terms in the previous series correspond to intensities of the pump beam in the 1st, 2nd... pass across the QW. We analyzed the half-processed wafer and the unpatterned metal clad microcavity using the 1D finite difference method (absorption losses in both metal and semiconductor were included, former being dominant). From the obtained values of α and k_x for the guided TE mode at $830nm$, we estimate N. For both the half-processed structure and the unpatterned metal clad structure, we calculate $N = 7$ (even when the top silver layer thickness varies between $20nm$ and $40nm$ in the unpatterned structure). Therefore, both the half-processed structure and the unpatterned metal clad microcavity have equal increases in the pumping intensity resulting from the pump beam trapping. We can also assume that patterned structures have their N factors between those of half-processed and unpatterned structures, i.e., $N = 7$. When the semiconductor core thickness in the half-processed structure increases to $150nm$ (due to the increase in thickness of GaAs layers), N decreases 3 times.

Based on the previous results, we can theoretically estimate the effective pumping intensities β for all analyzed structures. Results are shown in Table 2.5.

Table 2.5: Theoretically estimated effective pumping intensities ($\beta = T_p N$), and pumping intensities normalized with respect to the unprocessed wafer ($\frac{\beta}{\beta_{unp}}$).

structure type	β	β/β_{unp}
unprocessed	0.7	1
half-processed	4.9	7
unpatterned	0.47	0.67
$a = 250nm$, $s = 160nm$	2.5	3.57
$a = 480nm$, $s = 160nm$	1.2	1.7
$a = 650nm$, $s = 160nm$	0.9	1.29

Explanation of measurement results

Starting from the equation 2.48 and our theoretical estimates of β, η_{ext} (into the 30^o collection angle) and F_d, we calculated PL enhancements, both at $986nm$ and $930nm$. The theoretical results for the unprocessed, half-processed and unpatterned structures are collected in Table 2.6. We can conclude that there is a very good agreement between experiment and theory, i.e., Tables 2.3 and 2.6. Therefore, the half-processed structure has a 21-fold PL intensity enhancement at $986nm$ relative to the unprocessed wafer, as a result of seven times larger pumping intensity and a threefold increase in efficiency. The unpatterned metal clad microcavity has a 5.5-fold PL intensity increase at $986nm$ with respect to the unprocessed wafer, as a result of the eightfold improvement in efficiency and somewhat lower pumping intensity. At $930nm$, this structure has the output 1.5 times larger than the half-processed wafer, even though it is pumped weaker. This was also predicted theoretically in Table 2.6 and comes from the increase in the efficiency with respect to the half-processed wafer at $930nm$. The prominent peak at $930nm$ in this structure is partly due to almost threefold decay rate enhancement.

Table 2.6: Theoretically estimated PL enhancements of structures made from the 1st wafer. The unpatterned structure is a metal clad semiconductor slab ($90nm$ thick), with $25nm$ thick silver on top.

	$E_{up}(986nm)$	$E_{hp}(986nm)$	$E_{hp}(930nm)$
unprocessed	1	-	-
half-processed	19	1	1
unpatterned	6	0.3	2

Structures with periodicities of $480nm$ or $650nm$ have performances similar to the unpatterned structure, as we theoretically predicted. The structure with periodicity of $480nm$ has somewhat larger peak at $930nm$, due to the better extraction of radiation from perpendicular dipoles.

The structure with a periodicity of $250nm$ has a 46-fold photoluminescence intensity enhancement at $986nm$ relative to the unprocessed wafer. After taking into account the difference in pumping intensity, this PL enhancement is converted into the 13-fold efficiency

enhancement into the detection angle of 30^o, compared to the unprocessed wafer at $986nm$ (or 4.4-fold enhancement relative to the half-processed structure). This mostly comes from the large extraction efficiency of the folded TM and TE modes in this structure, as discussed previously. At $930nm$, this structure has a 5.5-fold PL enhancement with respect to the half-processed wafer. After taking into account the difference in pumping levels, this is converted into the 11-fold efficiency enhancement with respect to the half-processed wafer (or almost 30-fold efficiency enhancement relative to the unprocessed wafer). This is a result of much larger extraction efficiencies for parallel, and especially for perpendicular dipoles that dominate at $930nm$.

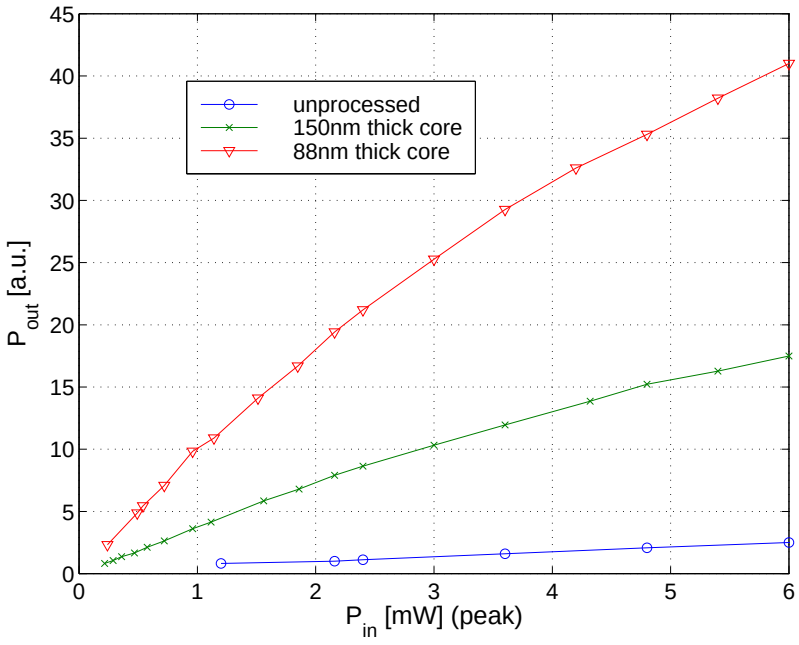

Figure 2.30: Measured LL curves corresponding to the unprocessed structure or the half-processed structures with $88nm$ or $150nm$ thick core.

Thin semiconductor films on top of a metal layer - experimental results

We have also measured the LL curves corresponding to the unprocessed wafer and the half-processed structures with a semiconductor core which is either $88nm$ or $150nm$ thick. The half-processed structure with a $150nm$ core was made from another wafer, in which

the thickness of GaAs layers was increased. The pump power was controlled using neutral density filters, as shown in Figure 2.25. The result is shown in Figure 2.30, where the vertical axis corresponds to the PL peak at $986nm$. These results also agree very well with our theoretical predictions. In the linear region, the slope of the LL curve of the structure with $88nm$ thick core is 20 times larger than that of the unprocessed wafer. The increase in the core thickness of the half-processed structure to $150nm$ results in the 2.5-fold decrease in the LL slope. From Figure 2.22, we do not expect that the efficiency of the structure would change significantly with this change in the core thickness. The difference in the LL slope comes from the difference in the pumping intensities of the two structures (i.e., the difference in N). As we discussed previously, N decreases around three times with this increase in the core thickness.

2.10 Conclusion

We have theoretically analyzed, fabricated and measured the metal clad microcavity with a sub-$\lambda/2$ semiconductor membrane and a patterned top metal layer. The emitting region is a single QW positioned in the middle of the membrane. At the same external pump power, we measured photoluminescence enhancements of up to 46 times with respect to the unprocessed wafer, and estimated that this enhancement was due to at least a 13-fold increase in the efficiency (relative to an unprocessed wafer and into the 30^o detection angle), and an increase in the effective pumping intensity resulting from the pump photons trapping within the microcavity. Up to 30-fold increase in the efficiency into the 30^o cone and relative to the unprocessed wafer was estimated at $930nm$. Interesting modifications in the photoluminescence spectra were also experimentally observed, resulting from the simultaneous change in the spontaneous emission rate and extraction efficiency.

Therefore, we have showed that periodic metallic structures (metallic photonic crystals) can be used to improve the light extraction and enhance the spontaneous emission rate in light emitting devices. The advantages of this design are a small surface recombination rate, and metallic layers that can be used both as contacts and for efficiency improvement. Certainly, in order to make good contacts, more attention has to be paid to the proper choice of metal. Devices presently operate in the $980nm$ wavelength range, where metal

absorption losses are significant. This reduces quality factors of fully processed structures to values between 10 and 15 and broadens their emission. This problem can be overcome by designing devices that operate at longer wavelengths. For example, a surface plasmon laser operating at $17\mu m$ has been demonstrated recently by researchers in Bell Labs.[77] We have tested only 1D metallic photonic crystals, because they were simple to analyze theoretically and explain obtained experimental results. However, even larger efficiency enhancements will be possible by employing metallic structures periodic in 2D, since they can extract light in broader range of wavevectors.

We conclude that structures based on metallic photonic crystals printed on a semiconductor wafer can be used as building blocks for highly efficient light emitting diodes. However, in order to make a practical device, more research and work has to be done, particularly in designing their electrical properties, reducing absorption losses and employing metallic structures periodic in 2D.

Chapter 3 Alternative fabrication methods

Feature sizes of structures presented in this thesis are below those achievable by photolithography. Therefore, high-resolution lithography is necessary for their fabrication. The e-beam writing techniques that we presently use suffer from limitations in speed and wafer throughput. For this reason, they also represent a huge obstacle to commercialization of photonic crystals. An alternative to serial e-beam writing that could provide us with the speed of photolithography and the resolution of e-beam writing is *electron beam projection lithography*. This lithographic method has been investigated for over 30 years,[78–80] but the old

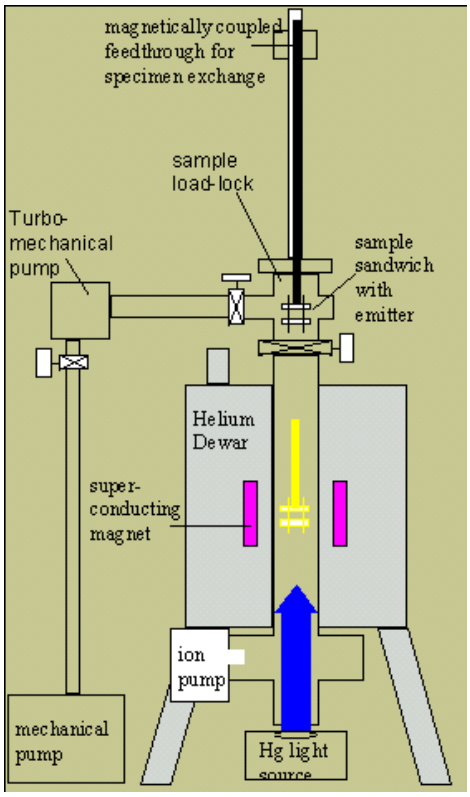

Figure 3.1: Electron beam projection lithography system.

prototypes suffered from a number of problems, such as sample heating, mask contamination, surface charging, magnetic field distortions and electron proximity effects. Several

years ago, we constructed a 1:1 electron beam projection system at Caltech, addressed some of the previously mentioned problems and demonstrated lithography with the feature sizes of 150nm. The cross section of our system is shown in Figure 3.1. The operation principle is very simple and is outlined in Figure 3.2. A shaped beam of electrons is photoemitted from a mask and projected onto an e-beam resist coated sample. The shape of the beam is determined by the pattern on the mask. The motion of electrons between the mask and the sample is controlled by static electric and magnetic fields, whose orientation is perpendicular to the mask and sample surfaces. The electric field is controlled by the voltage applied between the mask and the sample. Both mask and sample are placed into a bore of a superconducting magnet, which allows the tuning of magnetic field amplitude and uniformity. In the 1:1 projection system, electrons undergo an integer number of cyclotron orbits on their path from the mask to the sample. The sample surface is coated with e-beam resist and the shape of the beam is projected to an image on the sample surface.

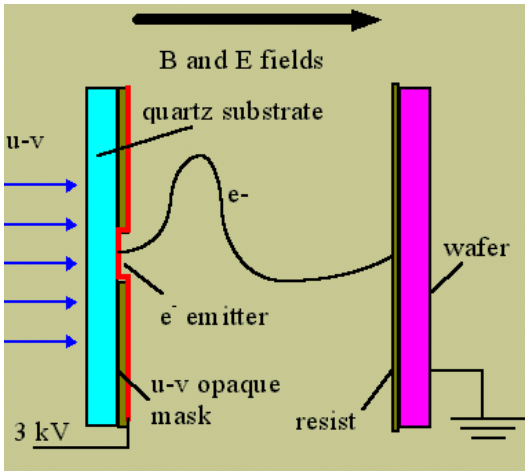

(a)

Figure 3.2: Operation principle of a 1:1 electron beam projection lithography system.

The mask making procedure is very simple. In the first step, a quartz plate is coated with Cr/Au layers nontransparent for the UV radiation. Au layer alone can block the UV radiation, but it has a very poor adhesion to quartz. For that reason, it is necessary to

deposit a thin Cr layer in between the quartz plate and the Au layer. The masks used in our experiments have Cr and Au layers that are approximately 20nm and 80nm thick, respectively. Conventional e-beam writing is used to define the desired pattern on the mask, which is subsequently transferred through Cr/Au using Ar^+ ion milling. Finally, mask is coated with a thin (30nm to 50nm) Au or AuPd layer which is used as a source of electrons. Electrons can be emitted only from areas where the Cr/Au was removed during the ion milling process. The mask is re-usable for projections. If the energy of a UV photon is matched exactly to the work function of Au (5eV), the photoemitted electrons have initial energies equal to zero and their motion is completely controllable by the applied electric and magnetic fields. This is, however, possible only if the used UV source has a very narrow

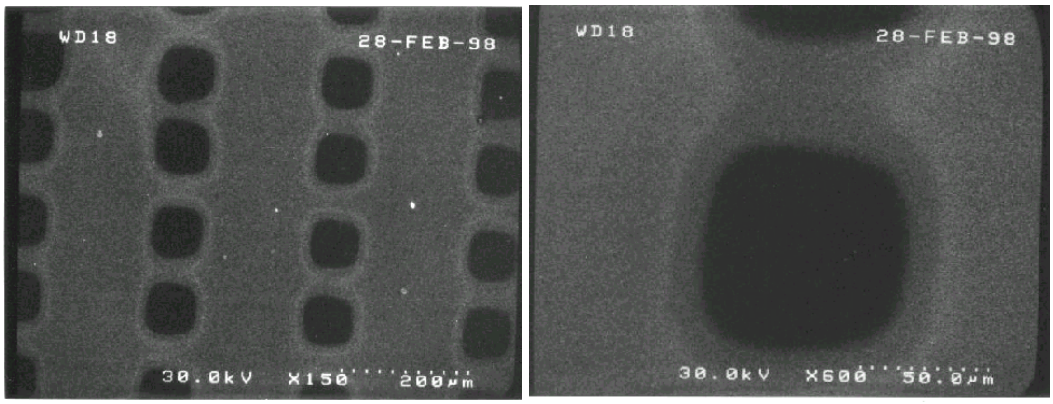

(a) (b)

Figure 3.3: Results of projection without magnetic field. The pattern defined on the mask is a 2D array of squares.

linewidth (such as in the case of using a laser). However, when a UV lamp is used, the photoemitted electrons have a range of initial energies (denoted as W_0) and can be emitted with a variety of initial angles with respect to the mask surface (denoted as α). The spread in W_0 and α is what makes the focusing difficult. Perfect focusing is achieved if all electrons emitted from a spot on the mask are projected into the same size spot on the sample. This is possible if all electrons make an integer number of cyclotron orbits on their route between the mask and the sample. Let us denote the distance between the mask and sample surfaces by d, the applied voltage and magnetic field by V and B, and the charge and mass of an

electron by e and m. In our system at Caltech, $d = 1.57mm$. For a particular electron, the focusing condition can be expressed as

$$N\frac{2\pi m}{eB} = d\sqrt{\frac{2m}{eV}}\left(1 - cos\alpha \cdot \sqrt{\frac{W_0}{eV}}\right), \tag{3.1}$$

where N is the integer number of cyclotron orbits that the electron makes on its journey from the mask to the sample. Knowing W_0 and α, we can choose V and B in order to obtain an integer N.

(a) (b)

Figure 3.4: Projection results with $B = 1.85T$, $V = 3kV$: (a) mask; (b) sample.

However, we cannot choose unique V and B to achieve focusing for many electrons with different W_0 and α. For a particular choice of electric and magnetic field, some electrons cannot accomplish an integer number of cyclotron orbits, which means that a point on the mask is projected onto a disk on the sample. The goal of the focusing is to choose V and B in such a way to minimize the diameter of that projected disk (denoted as D). When calculating the focusing condition, we assume that the initial energies of electrons in our system (W_0) vary between 0 and 0.4eV, and that the initial angles of electron emission (α) are in the range between 0^o and 90^o. In reality, the projected disk will have a smaller diameter than the one we calculate, since not all initial energies and angles of electrons are equally likely.

If magnetic field is not used in the projection, the resulting image on the sample is blurred,

as shown in Figure 3.3, since electric field alone is not enough to achieve focusing. By tuning B and V, we can also tune the quality of focusing. For example, the projection results at $B = 1.85T$, $V = 3kV$ are shown in Figure 3.4. Electrons make $N = 5$ cyclotron orbits in this case and the diameter of the projected disk on the sample is $D = 413nm$. Focusing can be somewhat improved for $B = 2.4T$ and $V = 3.56$kV. For this set of parameters, we calculate $N = 6$ and $D = 348nm$, and the projection result is shown in Figure 3.5(a). The best projection results are obtained for $B = 3.32T$ and $V = 3kV$ and are shown in Figures 3.5(b) and 3.6. Photoemitted electrons make $N = 9$ cyclotron orbits in this case, and the

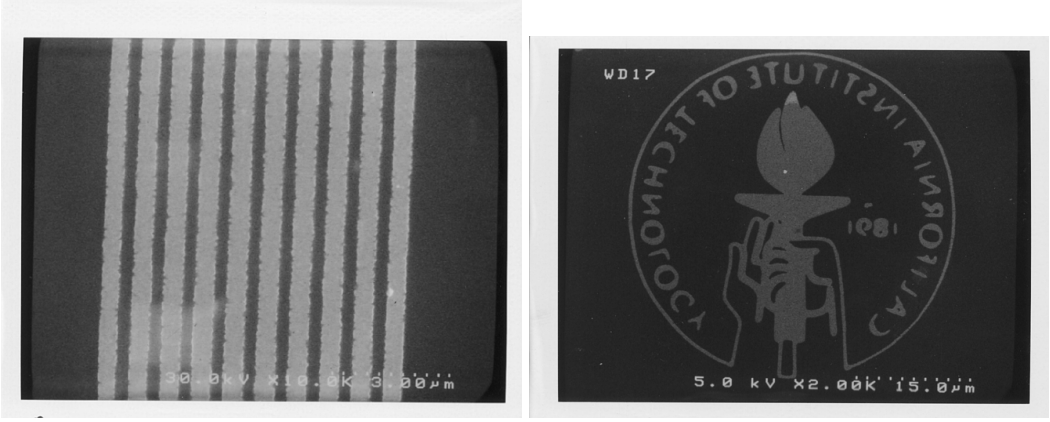

(a) (b)

Figure 3.5: Projected patterns: (a) $B = 2.4T$ and $V = 3.56kV$ (sample after ion milling); (b) $B = 3.32T$ and $V = 3kV$ (before ion milling).

diameter of the projected disk is $D = 250nm$. Samples used in all presented projections are Si wafers coated with 30nm of Au and 60nm of PMMA (molecular weight 950K) on top. Samples are coated with Au on both sides, in order to connect the top sample surface to the ground potential. The projected area is a circle with the diameter of 2.5cm. The projection time is calculated according to the formula $t = \frac{QA}{I}$, where A is the projected area, I is the photoemission current and Q is the optimum exposure dose for the corresponding PMMA thickness and the beam energy.[81] Our projections lasted between 10 and 20 minutes, due to the poor electron emission efficiency (i.e., small I). After the projection, the sample is taken outside the e-beam projection system and PMMA is developed first in IPA, and

then in a 3:7 solution of 2-ethoxyethanol:methanol. The developed PMMA can be used as a mask for the Ar^+ ion milling and the transfer of the projected pattern through the Au layer.

In our electron beam projection system at Caltech, we have managed to address some of the problems of the previous prototypes. The difference of our approach with respect to the old ones lies in the use of high magnetic fields and low voltages, as well as in the mask and sample preparation. High magnetic fields reduce the radius of the cyclotron orbit and, subsequently, reduce the projected spot diameter D. The use of a superconductive magnet helps to achieve the uniformity of magnetic field, and the low acceleration voltage helps in reduction of proximity effects. Moreover, our masks did not show significant signs of contaminations, even after several tens of exposures. Our biggest problems were, however, poor electron emission efficiency, and the use of a broad linewidth source for electron excitation (UV lamp), which resulted in a resolution limited to about 200nm. During the long projection times, it becomes very difficult to control all the parameters of the system (such as the photoemission current, mechanical vibrations affecting the B field uniformity, etc.), and the reproducibility of results becomes a problem. Therefore, the first two steps in the future work are the exploration of other photoemissive materials, possibly with higher efficiency, and the use of narrow linewidth sources for electron excitation.

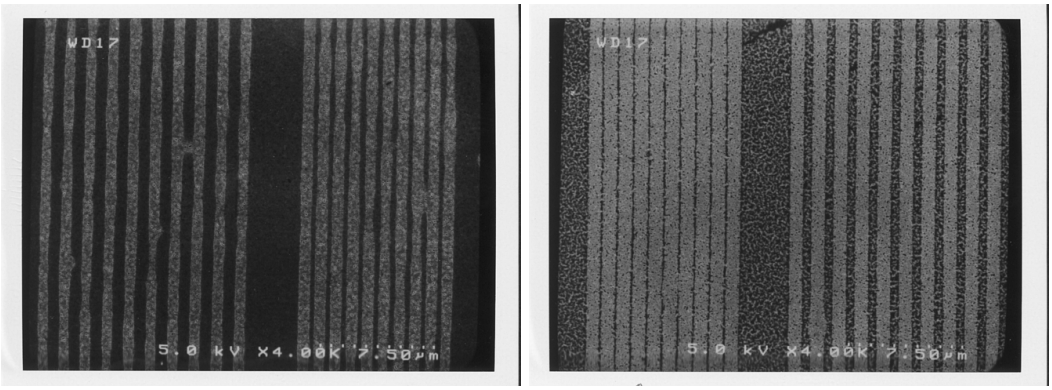

(a) (b)

Figure 3.6: Projected patterns with $B = 3.32T$ and $V = 3kV$: (a) Before ion milling; (b) After ion milling.

Appendix A Analysis of photonic crystal structures using the FDTD method

The finite-difference time-domain (FDTD) method will not be described in great detail here, since there are many excellent references that do that, such as the book by Taflove.[82] Briefly, the FDTD method is a very powerful technique of computational electromagnetics, based on the discretization of Maxwell's equations in space and time. It was proposed by Yee and 1966,[83] and it has been very popular ever since. Its advantage lies in the simplicity and the possibility of analyzing any desired geometry, and the disadvantage is in the large amounts of memory and long computation times required for the analysis. This appendix gives only a brief description of the methods used in this thesis and points out to references of interest.

A.1 FDTD calculation of band diagrams

We use 3D FDTD to calculate band diagrams of planar PC structures, and 2D FDTD for band diagrams of metal clad waveguides with 1D grating on top. The use of FDTD in dispersion diagram calculation of 3D photonic crystals was proposed in Reference 84. In References 85 and 28, the 3D FDTD was used for calculation of dispersion diagrams of planar PC structures. To the best of our knowledge, we presented the first analysis of band diagrams of the metallic photonic crystals at optical frequencies, based on the FDTD.[67]
Here we describe briefly the procedure used in the calculation of TE-like band diagrams of planar PC structures, such as the one shown in Figure 1.1. (The similar procedure is applied to all other types of PC structures.) The appropriate Bloch boundary conditions are applied to the boundaries of the unit PC cell in x and y directions. The structure is not periodic in the z direction and the full description of the slab and surrounding air has to be made. To select TE-like modes, even mirror BC are applied to the lower boundary in the z direction,

which coincides with the middle of the slab. Mur's absorbing boundary conditions (ABC)[53] are applied to the upper boundary in the z direction, which is positioned at least λ from the surface of the membrane. The initial field containing appropriate field components (e.g., B_z for TE-like modes) is applied, and subsequently evolved over a long interval of time (of the order of 300 periods corresponding to the mid-gap frequency). During the time evolution, we store the field at several points of low symmetry in the microcavity. After applying a Fast Fourier Transform (FFT) to the resulting time series, we observe the resonant peaks in the spectrum corresponding to the modes of the structure, at the in-plane wavevector determined by Bloch boundary conditions. This procedure is repeated for many different wavevector values at the boundary of the 1st Brillouin zone, and the resulting band diagram looks like those shown in Figure 1.2.

A.2 FDTD filtering of the mode of interest

Starting with an initial field distribution $\vec{E}(\vec{r}, t = 0)$ and $\vec{H}(\vec{r}, t = 0)$, we use the FDTD analysis to time evolve the electric and magnetic field in the computational domain. During the time evolution, we store the field at a point of low symmetry in the microcavity. After applying a Fast Fourier Transform (FFT) to the resulting time series, we observe the resonant peaks in the spectrum corresponding to the modes of the structure. Then we filter the electromagnetic field for the mode of interest. The filtering is done by convolving the electromagnetic field in time with a bandpass filter centered at the resonant frequency of the fundamental mode and with an appropriate bandwidth.[86]

A.3 FDTD analysis of metallic photonic crystals

The FDTD (finite-difference time-domain) method is used to theoretically analyze electromagnetic fields within metal clad microcavities. In order to accurately model metals at optical frequencies, it is necessary to make some changes[87,88] to the standard Yee's FDTD scheme.[83] Electromagnetic fields in metals are described by adding a current term ($\vec{J}$) to

Maxwell curl equations (e.g., in the Drude model):

$$\vec{\nabla} \times \vec{H} = \epsilon_0 \frac{\partial \vec{E}}{\partial t} + \vec{J} \tag{A.1}$$

$$\vec{\nabla} \times \vec{E} = -\mu_0 \frac{\partial \vec{H}}{\partial t} \tag{A.2}$$

$$\frac{\partial \vec{J}}{\partial t} + \Gamma \vec{J} = \epsilon_0 \omega_p^2 \vec{E}, \tag{A.3}$$

where ω_p is the plasma frequency of a metal and Γ is the corresponding damping rate. In part of our FDTD calculations, we neglect metal absorption losses by applying $\Gamma = 0$. Non-metallic regions are described with standard Maxwell curl equations:

$$\vec{\nabla} \times \vec{H} = \epsilon(\vec{r}) \frac{\partial \vec{E}}{\partial t} \tag{A.4}$$

$$\vec{\nabla} \times \vec{E} = -\mu_0 \frac{\partial \vec{H}}{\partial t} \tag{A.5}$$

The FDTD method consists, basically, of discretization of previous equations in space and time.[82] Depending on the problem, different boundary conditions (BC) are applied to boundaries of the computational domain, such as the Mur's absorbing boundary conditions[53] or Bloch BC. The spatial discretization step is critical in this case, keeping in mind that the penetration depth of electromagnetic field into metals can be of the order of only tens of nanometers. This implies that large amounts of memory are required for computation unless variable cell sizes are used. All calculations of metallic photonic crystals in this thesis are obtained using either Drude or Lorentz model of silver with the following parameters: $\epsilon_\infty = 1$, $\lambda_p = 140nm$ (i.e., $\hbar\omega_p = 8.8eV$), $\hbar\Gamma = 0.05eV$ (or $\Gamma = 0$ for the lossless metal) and $\chi_0 = 10$ for the Lorentz model. The discretization step used in FDTD analysis of metals was between $1nm$ and $3nm$. The increase in the discretization step (to $3nm$) causes a small shift in positions of some bands.

For the analysis of dispersion diagrams, we assume that structures are infinite in the third dimension (i.e., z direction), and periodic in the x direction (which is also the direction of wave propagation), with periodicity equal to a. Unpatterned (smooth) structures are periodic in the x direction with arbitrary periodicity a. Therefore, we can choose a and analyze only one unit cell, as in the case or truly periodic structures. Mur's ABC are applied to boundaries of the unit cell in the y direction, while Bloch BC are applied to boundaries in

the x direction. Bloch boundary conditions in the x direction can be expressed as

$$u(x+a) = u(x)e^{ik_x a}, \tag{A.6}$$

where a represents the corresponding periodicity and $u(x)$ represents some field component at position x. However, in the presence of absorption losses, fields decay in the direction of propagation (i.e., k_x has both real and imaginary parts) and the correct way of expressing boundary conditions would be

$$u(x+a) = u(x)e^{(ik_x' a - k_x" a)}, \tag{A.7}$$

where k_x" represents the damping in the x direction. Even when significant losses are present (i.e., k_x" is not negligible), for small periodicities a, the equation (A.6) still holds. On the other hand, for large a, the amplitude of the wave decays significantly between the unit cell boundaries in the x direction, and the wave does not satisfy the originally Bloch boundary conditions anymore. Fortunately, in the wavelength range of our interest ($1\mu m$), the imaginary part of silver dielectric constant is still much smaller than its real part, and positions of bands can be determined approximately by neglecting absorption in metal, i.e., assuming that $\Gamma = 0$ and $k_x" = 0$. The additional problem that occurs after the inclusion of absorption losses is that Q factors of bands are small, and it is difficult to recover them from spectra obtained in FDTD analyses.

Bibliography

[1] H.A. Haus and C.V. Shank. Antisymmetric taper of distributed feedback lasers. *IEEE Journal of Quantum Electronics*, 12:532, 1976.

[2] E. Yablonovitch. Inhibited Spontaneous Emission in Solid-State Physics and Electronics. *Physical Review Letters*, 58(20):2059–2062, May 1987.

[3] S. John. Strong localization of photons in certain disordered dielectric superlattices. *Physical Review Letters*, 58:2486–2488, 1987.

[4] John D. Joannopoulos, Robert D. Meade, and Joshua N. Winn. *Photonic Crystals*. Princeton University Press, Princeton, New Jersey, 1995.

[5] P. Villeneuve and M. Piché. Photonic Bandgaps in Periodic Dielectric Structures. *Progress in Quantum Electronics*, 18:153–200, 1994.

[6] C.C. Cheng, V. Arbet-Engels, A. Scherer, and E. Yablonovitch. Nanofabricated three-dimensional photonic crystals operating at optical wavelengths. *Physica Scripta*, T68:17–20, 1996.

[7] M. Lončar, D. Nedeljković, T. Doll, J. Vučković, A. Scherer, and T. P. Pearsall. Waveguiding at 1500nm using photonic crystal structures in silicon on insulator wafers. *Applied Physics Letters*, 77:1937–1939, September 2000.

[8] J. Vučković, M. Lončar, H. Mabuchi, and A. Scherer. Design of photonic crystal microcavities for cavity QED. *To appear in Physical Review E*, January 2002.

[9] O. Painter, R.K. Lee, A. Scherer, A. Yariv, J.D. O'Brien, P.D. Dapkus, and I. Kim. Two-Dimensional Photonic Bandgap Defect Mode Laser. *Science*, 284:1819–1821, June 1999.

[10] T. Yoshie, A. Scherer, H. Chen, D. Huffaker, and D. Deppe. Optical characterization of two-dimensional photonic crystal cavities with indium arsenide quantum dot emitters. *Applied Physics Letters*, 79(1):114–116, July 2001.

[11] P.R. Villeneuve, S. Fan, S.G. Johnson, and J.D. Joannopoulos. Three-dimensional photon confinement in photonic crystals of low-dimensional periodicity. *IEE Proceedings Optoelectronics*, 145:384–390, December 1998.

[12] D. Labilloy, H. Benisty, C. Weisbuch, C.J.M. Smith, T.F. Krauss, R. Houdre, and U. Oesterle. Finely resolved transmission spectra and band structure of two-dimensional photonic crystals using emission from InAs quantum dots. *Physical Review B*, 59:1649–1652, January 1999.

[13] S. Noda, A. Chutinan, and M. Imada. Trapping and emission of photons by a single defect in a photonic bandgap structure. *Nature*, 407(6804):608–610, October 2000.

[14] M. Boroditsky, R. Vrijen, T.F. Krauss, R. Coccioli, R. Bhat, and E. Yablonovitch. Spontaneous emission extraction and Purcell enhancement from thin-film 2-D photonic crystals. *Journal of Lightwave Technology*, 17(11):2096–2112, November 1999.

[15] J.K. Hwang, H.Y. Ryu, D.S. Song, I.Y. Han, H.W. Song, H.K. Park, Y.H. Lee, and D.H. Jang. Room-temperature triangular-lattice two-dimensional photonic bandgap lasers operating at 1.54μm. *Applied Physics Letters*, 76(21):2982–2984, May 2000.

[16] T. Baba, N. Fukaya, and A. Motegi. Clear correspondence between theoretical and experimental light propagation characteristics in photonic crystal waveguides. *Electronics Letters*, 37(12):761–762, June 2001.

[17] C.J.M. Smith, T.F. Krauss, H. Benisty, M. Rattier, C. Weisbuch, U. Oesterle, and R. Houdre. Clear correspondence between theoretical and experimental light propagation characteristics in photonic crystal waveguides. *Journal of the Optical Society of America B*, 17(12):2043–2051, December 2000.

[18] C. Monat, C. Seassal, X. Letartre, P. Viktorovitch, P. Regreny, M. Gendry, P. Rojo-Romeo, G. Hollinger, E. Jalaguier, S. Pocas, and B. Aspar. InP 2D photonic crystal microlasers on silicon wafer: room temperature operation at 1.55μm. *Electronics Letters*, 37(12):764–766, June 2001.

[19] N. Kawai, K. Inoue, N. Carlsson, N. Ikeda, Y. Sugimoto, K. Asakawa, and T. Takemori. Confined bandgap in an air-bridge type of two-dimensional AlGaAs photonic crystal. *Physical Review Letters*, 86(11):2289–2292, March 2001.

[20] J. Vučković, M. Lončar, and A. Scherer. Design of photonic crystal optical microcavities. *Proceedings of the SPIE meeting Photonics West 2001, San Jose*, January 2001.

[21] S.G. Johnson, S. Fan, A. Mekis, and J.D. Joannopoulos. Multipole-cancellation mechanism for high-Q cavities in the absence of a complete photonic bandgap. *Applied Physics Letters*, 78(22):3388–3390, May 2001.

[22] E. Miyai and K. Sakoda. Quality factor for localized defect modes in a photonic crystal slab upon a low-index dielectric substrate. *Optics Letters*, 26(10):740–742, May 2001.

[23] J. Vučković, M. Lončar, H. Mabuchi, and A. Scherer. Photonic crystal microcavities for strong coupling between an atom and the cavity field. *Proceedings of the LEOS 2000, Rio Grande, Puerto Rico*, November 2000.

[24] J. Vučković, M. Lončar, H. Mabuchi, and A. Scherer. Optimization of Q-factor in microcavities based on free-standing membranes. *To appear in IEEE Journal of Quantum Electronics*, 2002.

[25] J. Vučković, M. Lončar, H. Mabuchi, and A. Scherer. Quality factors of localized defect modes in planar photonic crystal structures. *Euresco conference: Electromagnetic crystal structures, St Andrews, United Kingdom*, June 2001.

[26] M. Lončar, T. Doll, J. Vučković, and A. Scherer. Design and fabrication of silicon photonic crystal optical waveguides. *Journal of Lightwave Technology*, 18(10):1402–1411, October 2000.

[27] E. Yablonovitch, T.J. Gmitter, R.D. Meade, A.M. Rappe, K.D. Brommer, and J.D. Joannopoulos. Donor and acceptor modes in photonic band-structure. *Physical Review Letters*, 67(24):3380–3383, December 1991.

[28] O. Painter, J. Vučković, and A. Scherer. Defect Modes of a Two-Dimensional Photonic Crystal in an Optically Thin Dielectric Slab. *Journal of the Optical Society of America B*, 16(2):275–285, February 1999.

[29] S. Ramo, J.R. Whinnery, and T. Van Duzer. *Fields and waves in communication electronics.* John Wiley and Sons, Inc., New York, 1994.

[30] H. J. Kimble. *in Cavity Quantum Electrodynamics, edited by P. Berman.* Academic Press, San Diego, 1994.

[31] Y. Yamamoto, T. Tassone, and H. Cao. *Semiconductor Cavity Quantum Electrodynamics.* Springer, Berlin, 2000.

[32] H. Mabuchi, M. Armen, B. Lev, M. Lončar, J. Vučković, H.J. Kimble, J. Preskill, M. Roukes, A. Scherer, and S.J. Van Enk. Quantum networks based on cavity QED. *Proceedings of the first international conference on experimental implementations of quantum computation*, 2001.

[33] E.M. Purcell. Spontaneous Emission Probabilities at Radio Frequencies. *Physical Review*, 69:681–681, 1946.

[34] Y. Yamamoto, S. Machida, K. Igeta, and Y. Horikoshi. *In Coherence and quantum optics, edited by E.H. Eberly et al.* Plenum Press, New York, 1989.

[35] J. Gerard, B. Sermage, B. Gayral, B. Legrand, E. Costard, and V. Tierry-Mieg. Enhanced spontaneous emission by quantum boxes in a monolitic optical microcavity. *Physical Review Letters*, 81(5):1110–1113, 1998.

[36] B. Gayral, J.-M. Gérard, B. Sermage A. Lemaître, and C. Dupuis. Time resolved probing of the Purcell effect for InAs quantum boxes in GaAs microdisks. *Applied Physics Letters*, 78(19):2828–2830, 2001.

[37] G.S. Solomon, M. Pelton, and Y. Yamamoto. Single-mode spontaneous emission from a single quantum dot in a three-dimensional microcavity. *Physical Review Letters*, 86(17):3903–3906, 2001.

[38] G. Björk and Y. Yamamoto. Analysis of semiconductor microcavity lasers using rate equations. *IEEE Journal of Quantum Electronics*, 27(11):2386–2396, November 1991.

[39] H. Yokoyama. Physics and device applications of optical microcavities. *Science*, 256:66–70, April 1992.

[40] Y. Suematsu and K. Furuya. Theoretical Spontaneous Emission Factor of Injection Lasers. *The Transactions of the IECE of Japan*, E60(9):467–472, September 1977.

[41] T. Baba, T. Hamano, F. Koyama, and K. Iga. Spontaneous Emission Factor of a Microcavity DBR Surface-Emitting Laser. *IEEE Journal of Quantum Electronics*, 27(6):1347–1358, June 1991.

[42] T. Baba, T. Hamano, F. Koyama, and K. Iga. Spontaneous Emission Factor of a Microcavity DBR Surface-Emitting Laser (II) - Effects of Electron Quantum Confinements. *IEEE Journal of Quantum Electronics*, 28(5):1310–1319, May 1992.

[43] M.K. Chin, D. Y. Chu, and S.T. Ho. Estimation of the Spontaneous Emission Factor for Microdisk Lasers via the Approximation of Whispering Gallery Modes. *Journal of Applied Physics*, 75(7):3302–3307, April 1994.

[44] D. Y. Chu and S.T. Ho. Spontaneous Emission from Excitons in Cylindrical Dielectric Waveguides and the Spontaneous-Emission Factor of Microcavity Ring Lasers. *Journal of the Optical Society of America B*, 10(2):381–390, February 1993.

[45] J. Vučković, O. Painter, Y. Xu, A. Yariv, and A. Scherer. Finite-difference time-domain calculation of spontaneous emission coupling factor in optical microcavities. *IEEE Journal of Quantum Electronics*, 35(8):1168–1175, August 1999.

[46] J. Vučković, O. Painter, Y. Xu, A. Yariv, and A. Scherer. Finite-difference time-domain calculation of spontaneous emission coupling factor in optical microcavities. *Proceedings of the SPIE meeting Photonics West*, 3937:2–1, January 2000.

[47] Y. Xu, J. Vučković, R. Lee, O. Painter, A. Scherer, and A. Yariv. Finite-difference time-domain calculation of spontaneous emission lifetime in a microcavity. *Journal of the OSA B*, 16(3):465–474, March 1999.

[48] Anthony E. Siegman. *Lasers.* University Science Books, Sausalito, California, 1986.

[49] E. A. Hinds. Perturbative Cavity Quantum Electrodynamics. *Cavity QED, edited by Paul R. Berman, Academic Press*, pages 1–55, 1994.

[50] Roy J. Glauber and M. Lewenstein. Quantum optics of dielectric media. *Physical Review A*, 43(1):467–491, 1991.

[51] Y. Xu, J. Vučković, R. K. Lee, O. J. Painter, A. Scherer, and A. Yariv. Finite-difference time-domain calculation of spontaneous emission lifetime in a microcavity. *Journal of the optical society of America B*, 16(3):465–474, 1999.

[52] A. Yariv. *Optical Electronics in Modern Communications*. Oxford University Press, New York, New York, 1997.

[53] G. Mur. Absorbing Boundary Conditions for the Finite-Difference Approximation of the Time-Domain Electromagnetic-Field Equations. *IEEE Transactions on Electromagnetic Compatibility*, EMC-23(4):377–382, November 1981.

[54] O. Painter, R. Lee, A. Yariv, A. Scherer, and J. O'Brien. Photonic bandgap membrane microresonator. *Integrated Photonics Research*, 4:221–223, 1998.

[55] E. Yablonovitch, D.M. Hwang, T.J. Gmitter, L.T. Florez, and J.P Harbison. Van der Waals Bonding of GaAs Epitaxial Liftoff Films onto Arbitrary Substrates. *Applied Physics Letters*, 56(24):2419–2421, June 1990.

[56] T. Yoshie, J. Vučković, A. Scherer, and D. Deppe. High quality two-dimensional photonic crystal slab cavities. *To appear in Applied Physics Letters*, December 2001.

[57] I. Schnitzer, E. Yablonovitch, C. Caneau, T.J. Gmitter, and A. Scherer. 30% External Quantum Efficiency from Surface Textured, Thin Film Light-Emitting Diodes. *Applied Physics Letters*, 63(16):2174–2176, October 1993.

[58] E.F. Schubert, N.E.J. Hunt, M. Micovic, R.J. Malik, D.L. Sivco, A.Y. Cho, and G.J. Zydzik. Highly Efficient Light-Emitting Diodes with Microcavities. *Science*, 265:943–945, August 1994.

[59] T. Baba, R. Watanabe, K. Asano, F. Koyama, and K. Iga. Theoretical and Experimental Estimations of Photon Recycling Effect in Light Emitting Devices with a Metal Mirror. *Japanese Journal of Applied Physics*, 35:97–100, January 1996.

[60] R. Windisch, P. Heremans, A. Knobloch, P. Kiesel, G.H. Dohler, B. Dutta, and G. Borghs. Light-Emitting Diodes with 31% External Quantum Efficiency by Outcoupling of Lateral Waveguide Modes. *Applied Physics Letters*, 74(16):2256–2258, April 1999.

[61] A. Kock, E. Gornik, M. Hauser, and W. Beinstingl. Strongly Directional Emission from AlGaAs/GaAs Light-Emitting Diodes. *Applied Physics Letters*, 57(22):2327–2329, 1990.

[62] I. Gontijo, M. Boroditsky, E. Yablonovitch, S. Keller, U.K. Mishra, and S.P. DenBaars. Coupling of InGaN quantum-well photoluminescence to silver surface plasmons. *Physical Review B*, 60(16):11564–11567, October 1999.

[63] M. Boroditsky, R. Vrijen, T.F. Krauss, R. Coccioli, R. Bhat, and E. Yablonovitch. Spontaneous Emission Extraction and Purcell Enhancement from Thin-film 2-d Photonic Crystals. *Journal of Lightwave Technology*, 17(11):2096–2112, November 1999.

[64] S.C. Kitson, W.L. Barnes, and J.R. Sambles. Full photonic bandgap for surface modes in the visible. *Physical Review Letters*, 77(13):2670–2673, September 1996.

[65] T.W. Ebbesen, H.J. Lezec, H.F. Ghaemi, T. Thio, and P.A. Wolff. Extraordinary optical transmission through sub-wavelength hole arrays. *Nature*, 391:667–669, February 1998.

[66] Jelena Vučković, Marko Lončar, Oskar Painter, and Axel Scherer. Surface Plasmon Enhanced LED. *Proceedings of the CLEO/QELS 2000, San Francisco*, pages 123–124, May 2000.

[67] Jelena Vučković, Marko Lončar, and Axel Scherer. Surface Plasmon Enhanced LED. *IEEE Journal of Quantum Electronics*, 36(10):1131–1144, October 2000.

[68] U. Kreibig and M. Vollmer. *Optical properties of metal clusters.* Springer-Verlag, Berlin, Heidelberg, 1995.

[69] N.W. Ashkroft and N.D. Mermin. *Solid state physics.* Saunders College Publishing, 1976.

[70] H. Raether. *Surface Plasmons.* Springer, Berlin, Germany, 1988.

[71] W.L. Barnes. Electromagnetic Crystals for Surface Plasmon Polaritons and the Extraction of Light from Emissive Devices. *Journal of Lightwave Technology*, 17(11):2170–2182, November 1999.

[72] D.G. Deppe, J.C. Campbell, R. Kuchibhotla, T.J. Rogers, and B.G. Streetman. Optically-coupled mirror-quantum well in InGaAs-GaAs light emitting diode. *Electronics Letters*, 26:1665–1666, 1990.

[73] J.A.E. Wasey and W.L. Barnes. Efficiency of spontaneous emission from planar microcavities. *Journal of Modern Optics*, 47(4):725–741, 2000.

[74] L.A. Coldren and S. W. Corzine. *Diode Lasers and Photonic Integrated Circuits.* John Wiley and Sons, New York, New York, 1995.

[75] M.S. Tomaš and Z. Lenac. Damping of a dipole in planar microcavities. *Optics Communications*, 100(1-4):259–267, 1993.

[76] J. W. Goodman. *Introduction to Fourier optics.* The McGraw Hill Companies, 1996.

[77] A. Tredicucci, C. Gmachl, F. Capasso, and A.L. Hutchinson. Single-mode surface-plasmon laser. *Applied Physics Letters*, 76(16):2164–2166, 2000.

[78] T.W. O'Keeffe. Fabrication of integrated circuits using the electron image projection system (ELIPS). *IEEE Transactions on Electron Devices*, ED-17(6):465–469, June 1970.

[79] T.W. O'Keeffe, J. Vine, and R.M. Handy. Electron imaging system for abrication of integrated circuits. *Solid-State Electronics*, 12:841–848, June 1969.

[80] F.F. Saville, P.M. Platzman, G. Brandes, R. Ruel, and R. Willett. Feasibility study of photocathode electron projection lithography. *J. Vac. Sci. Technology B*, B13(6):2184–2188, November 1995.

[81] P.A. Peterson, Z.J. Radzimski, S.A. Schwalm, and P.E. Russel. Low voltage electron-beam lithography. *J. Vac. Sci. Technology B*, 10(6):3088–3093, November 1992.

[82] A. Taflove. *Computational Electrodynamics - The Finite-Difference Time-Domain Method*. Artech House, Norwood, Masachussetts, 1995.

[83] K.S. Yee. Numerical Solution to Initial Boundary Value Problems Involving Maxwell's Equations in Isotropic Media. *IEEE Transactions on Antennas and Propagation*, AP-14(3):302–307, May 1966.

[84] D.F. Sievenpiper, E. Yablonovitch, J.N. Winn, S. Fan, P.R. Villeneuve, and J.D. Joannopoulos. 3D metallo-dielectric photonic crystals with strong capacitive coupling between metallic islands. *Physical Review Letters*, 80(13):2829–2832, March 1998.

[85] R. Coccioli, M. Boroditsky, K.W. Kim, Y. Rahmat-Samii, and E. Yablonovitch. Smallest possible electromagnetic mode volume in a dielectric cavity. *IEE Proceedings - Optoelectronics*, 145(6):391–397, December 1998.

[86] D.H. Choi and W.J.R. Hoefer. The Finite-Difference-Time-Domain Method and its Application to Eigenvalue Problems. *IEEE Transactions on Microwave Theory and Techniques*, 34(12):1464–1469, December 1986.

[87] S.A. Cummer. An Analysis of New and Existing FDTD Methods for Isotropic Cold Plasma and a Method for Improving Their Accuracy. *IEEE Transactions on Antennas and Propagation*, 45(3):392–400, March 1997.

[88] J.B. Judkins and R.W. Ziolkowski. Finite-difference time-domain modeling of nonperfectly conducting metallic thin-film gratings. *Journal of the Optical Society of America B*, 12(9):1974–1983, 1995.